THE UNIVERSITY OF CHICAGO

MODEL-BASED IMAGE RECONSTRUCTION FOR MULTIPLE VIEW MICROSCOPY

A DISSERTATION SUBMITTED TO
THE FACULTY OF THE DIVISION OF THE BIOLOGICAL SCIENCES
AND THE PRITZKER SCHOOL OF MEDICINE
IN CANDIDACY FOR THE DEGREE OF
DOCTOR OF PHILOSOPHY

COMMITTEE ON MEDICAL PHYSICS

BY
COREY SMITH

CHICAGO, ILLINOIS
JUNE 2020

To My Mom

"You Live Only As Long As the Last Person Who Remembers You."

– Akecheta, "Kiksuya." Westworld.

TABLE OF CONTENTS

LIST OF FIGURES

LIST OF TABLES

ACKNOWLEDGMENTS

I am extremely grateful for the support, mentorship, and guidance from my thesis advisor Patrick La Riviere, none of this would have been possible without him. When I joined the lab, I was fortunate to begin working on his new project. Without previous experience in the lab, I had the freedom and flexibility to explore new ideas and techniques that could be useful for our research. Along with this new project came a new collaboration with the Shroff lab at the NIH. Both Hari Shroff and Yicong Wu were instrumental for me as I entered the new world of microscopy and biology. Without any background in the field, they were able to explain topics in a way that I could understand.

My research, and culminating thesis would not have been possible without the help and support from the many people in the La Riviere lab. Dimple Modgil and Phil Vargas were constant sources of help and guidance during my entire time in the lab. Both of them were always willing to help me with any issues that arose. Talon Chandler was instrumental in helping me learn new best practice techniques and is the sole reason for why I now use Emacs. Dave Rigie, Bryan Quigley, Scott Trinkle, and Ben Preusser were always willing to answer questions. The lab would have been very lonely without their company, conversation, and friendship.

I also want to thank the other members of my thesis committee: Samuel Armato, Chien-Min Kao, and Emil Sidky. As a group, they were able to provide valuable guidance and feedback on my writing and presentations that helped me better explain my work to people who are experts outside the focus of my research.

I also wish to thank the different sources of funding that I received for the duration of my time in graduate school. Their funding made it so I never had to worry about if I was going to get paid. These funding sources include: National Institute of General Medical

Sciences of the National Institutes of Health under Award Number R25GM109439 (Project Title: University of Chicago Initiative for Maximizing Student Development (IMSD)), NIBIB under grant number T32 EB002103, BSD Diversity Research and Small Grants Program, and the Chicago Biomedical Consortium with support from the Searle Funds at the Chicago Community Trust.

Last, but certainly not least, I am forever grateful for my family: Cliff, Helen, Holly, Christian, Carissa, Brooke, Nathan, and Bear. They have always supported me and the goals that I set for my self. Whether that was moving half way around the country to go to college or deciding that I wanted to spend five more years in school. And finally, I have to mention my new cat Simon. He has been a great distraction when I need a break from writing in the last few months. Even if he sits on my laptop keyboard to prevent me from working.

ABSTRACT

Three-dimensional fluorescence imaging is an essential tool in biology, used for everything from long-term imaging in developmental biology to short-term, high-resolution imaging of single cells and molecules. In recent years, there has been an influx of new imaging techniques that push the limits on both resolution and the ability to perform extended time-course imaging. Many new techniques, like structured illumination microscopy (SIM), require multiple images of the sample or increased excitation intensity to create a high-resolution image. This increased exposure can lead to an increase of sample degradation through photobleaching and phototoxicity.

In this work, we focus on reducing these damaging effects by developing and implementing new imaging models for light-sheet microscopes that improve collection efficiency by allowing for additional views of the sample to be acquired in such a way that there is no increase in sample exposure or imaging time. As part of a collaboration with researchers at the National Institutes of Health, we worked with two new microscope designs. In the three-view diSPIM, we were able to improve quality for thin samples and show that for every noise level, adding the third objective increased image resolution. In our work on reflective imaging, our implementation allowed for imaging with a reflective coverslip, which improved both collection efficiency and imaging speed. In addition to adding more views of the sample, we worked on creating a more accurate imaging model of the diSPIM system to determine if image quality improved for data that has previously been acquired. In simulations, we found that a more precise model improved image quality, but using real data, we did not see such significant improvements. This suggests that there might be other factors that have a more significant contribution to the artifacts seen in the final reconstructions.

We also work on determining the theoretical resolution limits for structured illumination microscopes. This resolution limit allows us to choose the necessary parameters for acquisition that produce an image quality that is adequate for analysis.

Finally, we look at different reconstruction methods for SIM and use both simulations

and real data to determine if these reconstruction methods approach or converge to the theoretical resolution limit. In addition to testing the theoretical vs. realized resolutions limits, we used these reconstruction methods to test the viability of using fewer acquired images during reconstruction. Previous reconstruction methods are unable to account for redundancies in the data that occur when isotropic resolution is needed. With the methods that we implemented, we found that using just four images during reconstruction, we could get comparable image quality to reconstructions that used all nine images. This reduction in data would allow for faster imaging and less exposure to the sample. Both of which are necessary for imaging fast actions in live cells.

CHAPTER 1

INTRODUCTION

Microscopes, since their invention around 1590, have been an essential tool in biology. While its not clear who has the sole claim of inventorship, it is clear that its invention opened up an entirely new world to scientists. It was now possible to see living things in everything that surrounds us. The major limitation of these early microscopes was in the lens making and light sources.

It wasn't until the late 1800s, when the carbon arc lamp replaced kerosene lamps as the light source, that scientists could get consistent, high intensity light for sample illumination. In 1983, August Köhler published a new method for sample illumination that provided much more uniform illumination of the sample, and for the first time removed the illumination source from the imaging plane [24]. Around the same time, Ernst Abbe was developing new theory around the limitations for optical imaging [1]. Together, these new advancements helped to solidify the foundations of modern microscopy.

1.1 Introduction to Fluorescence Microscopy

Today, microscopy continues to be an invaluable tool for biologists, and is used in fields such as molecular, cell, and developmental biology. The focus of recent advancements in the field have mostly been in fluorescence microscopy. The first fluorescence microscope was developed in 1911 [19] to image bacteria. Imaging was done using UV light to excite intrinsic flurochromes in the cells. In 1994, researchers discovered ways to express and fluoresce green fluorescent protein (GFP) outside of the jellyfish *Aequorea victoria* [4]. The development of GFP was a huge breakthrough in the field of microscopy and was awarded the Nobel Prize in Chemistry 2008, with over 20,000 publications in the biological sciences citing GFP between 1992 and 2008 [10]. Today, fluorescence microscopy is a useful tool due to the ability to label specific molecules in cells and study both their location and function in a cell.

Advancements in the last 10–15 years have expanded the imaging capability of microscopes down to the internal structures of bacteria with nanometer resolutions [11]. Along with improved the spatiotemporal resolution for imaging of single molecules, advancements in optics and detectors have improved *in toto* imaging for developing embryos.

The concept of selective plane illumination microscopy (SPIM) was first used in 1902 to study gold particles by shining sunlight through a slit [34]. It wasn't until Huisken *et al.* [22] used SPIM in 2004 to image live embryos at nearly isotropic resolution the idea of using a selective excitation plane in fluorescence microscopy took off. In this approach, a sheet of light is used to excite a 2D plane perpendicular to the detection objective at its focal plane. This geometry has two main advantages over previous methods such as widefield microscopy. The first advantage is that due to only a single in-focus plane of the sample being excited, the overall exposure to the sample is reduced, which makes the method less damaging to cells during developmental imaging. The second major advantage is that the thickness of the light-sheet determines the axial resolution. In a widefield microscope, there is no axial sectioning ability, which reduces SNR as none of the out-of-focus light is rejected.

1.2 Introduction to Image Reconstruction

Many modern microscopes acquire multiple images of the sample in order to achieve the necessary image quality needed for analysis. To extract the information contained in the multiple sets of data, images need to be combined algorithmically to produce a single image or image stack. This algorithmic process is referred to as image reconstruction.

Besides combining the different acquisitions, image reconstruction can also remove artifacts such as noise and blurring that are introduced by the imaging process. Blurring in the images is the result of diffraction-limited optics. All imaging systems are band limited which means that frequencies above a certain threshold are not captured during imaging. This rejection of high-frequency components shows up in the image as blurring.

Noise contamination comes from a couple of different sources. One source of noise is

the result of the quantum nature of light. Counting the number of photons on the detector sensor is a stochastic process. When the photon count is low, this process follows a Poisson distribution. The other source of noise is introduced when reading and digitizing the photon counts in each sensor well.

1.2.1 Forward Models

For the image reconstruction to be able to reduce artifacts introduced during imaging, an accurate model of the imaging system is needed. An imaging model is a mathematical model that describes how objects in data space transform into measurement space during imaging. For a continuous to continuous model, this mapping between data space D, and measurement space M, is from one possibly infinite Hilbert space to another.

$$\mathcal{H} : \mathbb{D} \mapsto \mathbb{M} \tag{1.1}$$

Data space consists of all square-integrable functions in $\mathbb{R}^3$, and measurement space is the space of all square-integrable functions in $\mathbb{R}^2$.

$$\mathbb{D} = L_2(\mathbb{R}^3) \tag{1.2}$$

$$\mathbb{M} = L_2(\mathbb{R}^3) \tag{1.3}$$

Because of the digitization by the detector during measurement, measurement space is not a continuous space but a discrete space. This means that a more representative imaging model would be a continuous to discrete imaging model. However, for the following work, we only consider the continuous to continuous mapping in (1.3) or the discrete to discrete mapping in (1.4).

$$\mathcal{H}^{m\times n} : \mathbb{R}^{n\times 1} \mapsto \mathbb{R}^{m\times 1} \tag{1.4}$$

If we assume the mapping between data space and measurement space is linear, we can write (1.4) as

$$\boldsymbol{g} = \mathbf{H}\boldsymbol{f} + \boldsymbol{n} + \boldsymbol{b}. \tag{1.5}$$

Here, $\boldsymbol{f}$ is the fluorophore distribution being imaged, $\boldsymbol{n}$ is a random noise vector, $\boldsymbol{b}$ is a background vector that can be constant or spatially varying, $\mathbf{H}$ is the linear system matrix containing the physics of the imaging system, and $\boldsymbol{g}$ is the acquired set of data. This is a very generalized equation and is applicable to any linear imaging system.

When a system is both linear and shift-invariant, meaning that the blurring of the microscope doesn't change when the object is shifted, the forward model can be written as a convolution.

$$\mathbf{H}\boldsymbol{f} = f(\boldsymbol{r}) * h(\boldsymbol{r}) = \int \mathrm{d}\boldsymbol{r} f(\boldsymbol{r'}) h(\boldsymbol{r} - \boldsymbol{r'}). \tag{1.6}$$

Here, * denotes the convolution between f and h. $h(\boldsymbol{r})$ is called the system point spread function (PSF) for the system $\mathbf{H}$. The advantage of writing the forward model as a convolution is two-fold. Using a point-spread function rather than a system matrix significantly reduces the memory needed to describe the system and allows reconstructions to be done in an acceptable amount of time. A PSF will be on the order of N^3 pixels, while the system matrix would be on the order N^6 pixels. For a small volume of $200 \times 200 \times 200$ floats, the memory needed for the PSF is only around 32 Mb, where as the memory needed for the system matrix is 256 Tb.

1.2.2 Inverse Problems

Deriving reconstruction methods start with formulating an optimization or inverse problem that the reconstructed high-resolution image needs to satisfy.

$$\hat{\boldsymbol{f}} = \arg\min_{\boldsymbol{f}} \Phi(\boldsymbol{f}, \boldsymbol{g}), \tag{1.7}$$

where $\hat{\boldsymbol{f}}$ is the solution to the optimization problem and $\Phi(\boldsymbol{f}, \boldsymbol{g})$ is the cost function being minimized. The cost function can be split into three terms,

$$\Phi(\boldsymbol{f}, \boldsymbol{g}) = G(\mathbf{H}\boldsymbol{f}, \boldsymbol{g}) + \epsilon\, R(\boldsymbol{f}) + P(\boldsymbol{f}). \tag{1.8}$$

The first term $G(\mathbf{H}\boldsymbol{f}, \boldsymbol{g})$ is the data fidelity and measures how well the forward model applied to a reconstructed image agrees with the acquired data, the second term $R(\boldsymbol{f})$ is a regularization term that can be used to enforce prior knowledge such as smoothness, on the reconstructed image, the final term $P(\boldsymbol{f})$ enforces any additional constraints on the reconstructed image, such as constraining all of the image pixels to be non-negative. A constant parameter ϵ is added to control the balance between regularization and data agreement.

1.2.3 Cost Functions

If the noise model is assumed to follow a Poisson distribution, then the image reconstruction can be formulated as an optimization problem that maximizes the likelihood function. The likelihood function is a probability distribution for the underling fluorophore distribution given the acquired data. For a Poisson distribution, the likelihood function for $\boldsymbol{f}$ is the product of Poisson likelihood functions for each pixel i assuming that the pixels are independent.

$$\boldsymbol{L} = p(\boldsymbol{f}|\boldsymbol{g}) = \prod_i \frac{e^{-[(\mathbf{H}\boldsymbol{f})_i + \boldsymbol{b}_i]}[(\mathbf{H}\boldsymbol{f})_i + \boldsymbol{b}_i]^{\boldsymbol{g}_i}}{\boldsymbol{g}_i!}. \tag{1.9}$$

Finding the image that maximizes the likelihood function is equivalent to finding the image that minimizes the negative log-likelihood function,

$$G(\mathbf{H}\boldsymbol{f}, \boldsymbol{g}) = -\sum_i \left\{ \boldsymbol{g}_i \log \frac{\boldsymbol{g}_i}{(\mathbf{H}\boldsymbol{f})_i + \boldsymbol{b}_i} + [(\mathbf{H}\boldsymbol{f})_i + \boldsymbol{b}_i] - \boldsymbol{g}_i \right\}, \tag{1.10}$$

also known as the Csiszar I-divergence and is the data fidelity term used to set up the inverse problem [7].

Richardson and Lucy independently proposed iterative solutions to the optimization problem which includes only the data fidelity term in (1.10). This proposed solution is commonly referred to as RL deconvolution [29, 25].

$$\boldsymbol{f}^{t+1} = \frac{\boldsymbol{f}^t}{\mathbf{S}} \left[\mathbf{H}^{\mathrm{T}} \frac{\boldsymbol{g}}{\mathbf{H}\boldsymbol{f}^t} \right], \tag{1.11}$$

where t is the iteration number, $\mathbf{S}$ is the sensitivity matrix of the imaging system computed by applying the transpose of $\mathbf{H}$ to a vector of ones, and division is point-wise. RL deconvolution has no explicit positivity or smoothness constraints placed on the reconstructed images. However, positivity is enforced as long as the initial estimate and acquired data is non-negative.

CHAPTER 2

MULTIVIEW LIGHT-SHEET MICROSCOPY.

2.1 Introduction

The use of selective plane illumination microscopy was a significant advance for developmental biology as it provided a more gentle method for imaging live cells over long periods of time [22]. However, when only a single view of the sample is acquired, the acquired image stack suffers from anisotropic resolution. The anisotropic resolution in SPIM is a result of using a single objective lens for detection. Any finite aperture used for detection will have poorer axial resolution when compared to the lateral resolution. Typically, the axial resolution is two to three times worse than the lateral resolution.

In addition to the inherent limitations when using a single detection objective, SPIM also has limitations that are result of the Gaussian laser beam used to create the excitation light-sheet. What this means is that as the waist of the light-sheet is made smaller, the beam starts to diverge faster away from the focal plane causing the effective FOV to shrink. In order to achieve nearly isotropic resolution, the sample needs to be rotated while 4-8 views of the sample are acquired [22].

Recent advancements have sought to create more isotropic resolution by adding additional detection objectives to acquire multiple view of the sample without the need for sample rotation. In [6], researchers developed IsoView microscopy. In this system the sample is positioned at the center of four orthogonal objective lenses. Both excitation and detection can be performed by all four of the lenses. This allows for multiple imaging configurations for simultaneous detection. While techniques such as IsoView do provide isotropic resolution, they do so at a considerable financial cost. Instead of a single objective lens and detector, this microscope configuration requires four objective lenses and detectors. For labs with financial constraints this could be a considerable barrier. Work done by Wu *et al.* provide an alternative solution with a much smaller financial barrier.

2.2 diSPIM with Spatially Varying PSF and TV Regularization

In [41], Wu *et al.* developed the dual-view inverted selective plane illumination microscopy (diSPIM) system, which modifies the SPIM system to include a second perpendicular objective that is capable of both excitation and detection. This modified configuration allows for the two lenses to rapidly switch between illuminating the sample and detecting emitted fluorescence. This allows for acquisition of two perpendicular stacks of images, one with the excess blurring in the z direction and the other with the excess blurring in the x direction, as shown in Figure 2.1. These two stacks of differently blurred images serve as the inputs to a joint deconvolution algorithm such as Richardson-Lucy introduced in Eqn. 1.11.

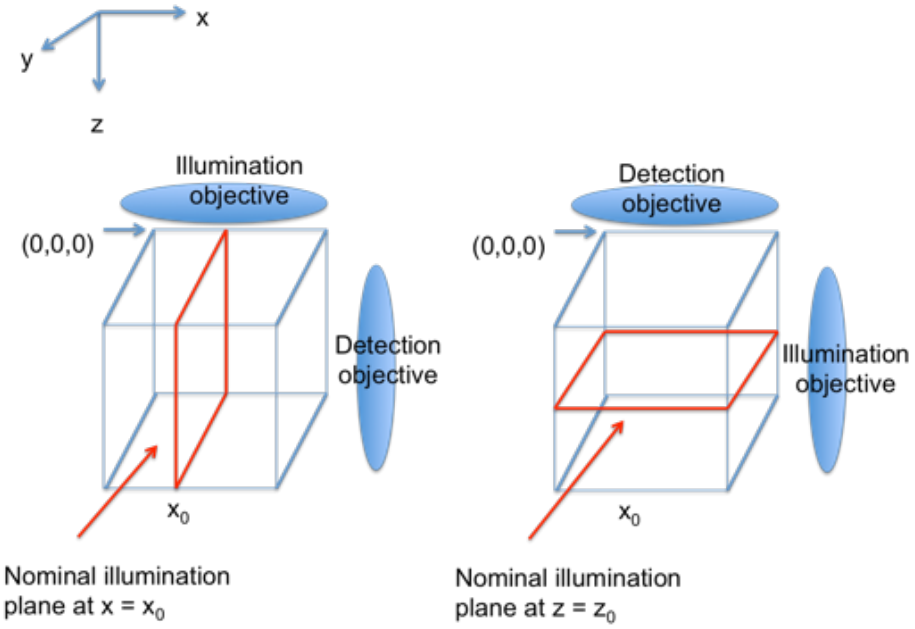

Figure 2.1: The diSPIM acquisition geometry. (Left) the upper objective is used to create a sheet beam that is imaged by the objective on the right. A 3D stack of images can be obtained by scanning the illuminated slice in x. (Right) The role of the objectives can be rapidly switched to obtain a 3D stack of images in the z direction. Each stack suffers excess blurring in the slice direction but they can be used as input to a joint deconvolution algorithm.

In reality, there are additional physical effects that can degrade the quality of diSPIM images and limit the size of objects that can be imaged. First, the illumination sheet is not expected to have a strictly uniform profile through the object but will have more of an

hourglass shape, as shown in Figure 2.2. Our work aims to use a more accurate blurring model in the deconvolution that takes into account this non-uniform illumination sheet.

2.2.1 Beam Modeling

To incorporate the more physical beam into the deconvolution algorithm we derived a new imaging model that accounts for the beam waist widening away from the center of the field of view. Figure 2.2 shows how the beam width changes through the FOV.

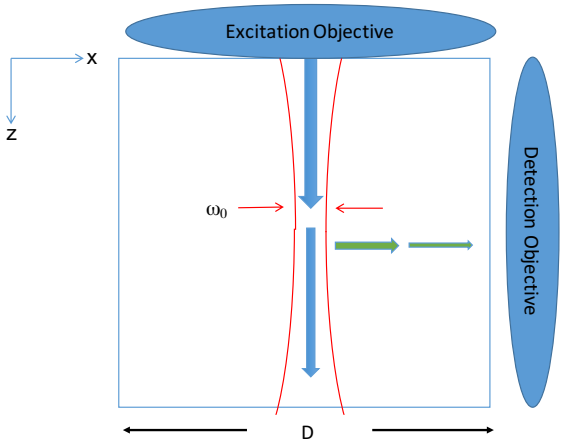

Figure 2.2: Illustration of the beam widening as the laser propagates through the FOV. As the excitation light travels through the FOV, it is attenuated while being focused to the focal place of the objective. After the focal plane, the beam begins to widen. The emission light that is a result of exciting the fluorophore is attenuated as it travels from the sample to the detection objective.

With illumination centered at x_0, the fluorescence emission is given by,

$$E_{x_0}(x, y, z) = f(x, y, z)\ G[x - x_0, \sigma_B(z)]\ e^{-\mu_I z}. \tag{2.1}$$

In this equation, G is the intensity the Gaussian excitation beam, f is the fluorophore distribution in the sample we want to estimate, $\sigma_B(z)$ is the depth-dependant standard deviation of the Gaussian beam, and μ_I is the attenuation coefficient of the excitation beam

as it travels through the sample. A model for the Gaussian beam [27] can be written as

$$G[x, \sigma_B(z)] = \left(\frac{\sigma_{B_0}}{\sigma_B(z)}\right) \exp\left[-2\frac{x^2}{\sigma_B(z)^2}\right], \tag{2.2}$$

$$\sigma_B(z) = \sigma_{B_0}\sqrt{1 + \left(\frac{z}{z_R}\right)^2}, \tag{2.3}$$

$$z_R = \frac{\pi(\sigma_{B_0})^2}{\lambda_{ex}}, \tag{2.4}$$

where σ_{B_0} is the radius of the beam at the focal spot, z_R is the Rayleigh length of the beam, and λ_{ex} is the wavelength of the excitation beam. The Rayleigh length measures the distance from the focal plane where the beam waist is $\sqrt{2}$ larger than σ_{B_0}. The intensity recorded at the detector, D_A, is the emitted fluorescence (2.1), multiplied by an attenuation factor $e^{-\mu_{F^*}(D-x)}$, and acted on by the system point spread function. The attenuation factor is the product of the attenuation coefficient for the emitted light as it leaves the sample, and the distance $D-x$ that the light travels through in the sample before it reaches the detector.

$$g^{\mathrm{A}}(x_0, y_0, z_0) = \iiint \mathrm{d}x\,\mathrm{d}y\,\mathrm{d}z\,[E_{x_0}(x, y, z)\; e^{-\mu_{F^*}(x-D)}]h(x_0 - x, y_0 - y, z_0 - z) \tag{2.5}$$

If the point spread function h is narrow compared to the slowly varying attenuation, we can pull the two attenuation factors outside of the integrals. If we also assume that the widening of the excitation beam is slow compared to the PSF, we replace $z- > z_0$ in the depth dependent beam waist formula.

$$g^{\mathrm{A}}(x_0, y_0, z_0) = A(x_0, z_0) \iiint \mathrm{d}x\,\mathrm{d}y\,\mathrm{d}z\,\Big[f(x, y, z) * G[x - x_0, \sigma_B(z)]h(x_0 - x, y_0 - y, z_0 - z)\Big] \tag{2.6}$$

$$A(x_0, z_0) = e^{-\mu_{I^*} z_0} e^{-\mu_{F^*}(D-x_0)} \tag{2.7}$$

The last assumption that we want to make is that h_{A} can be approximated by a separable

PSF. This assumption significantly reduces the computation time needed to compute the forward model as it will allow us to use a series of convolutions. Later on in Section 2.4 we will see what happens when we can't make this assumption. Rewriting (2.6) using a 3D Gaussian function as the PSF gives us

$$g^{\mathrm{A}}(x_0, y_0, z_0) = \int \mathrm{d}z \; \eth(z_0 - z, \sigma_l) \left[\iint \mathrm{d}y \, \mathrm{d}x \; f(x, y, z) G(x_0 - x, y, \sigma_b(z_0))) \eth(x_0 - x, \sigma_a) \eth(y_0 - y, \sigma_l) \right], \tag{2.8}$$

where $\eth(x, \sigma)$ is a zero-mean Gaussian function with a standard deviation (SD) σ, σ_l is the lateral SD, and σ_a is the axial SD In this form, we see that for a fixed z, the integrals over x and y can be computed as a series of 2D convolutions. The last integral is then a series of 1D convolutions with the resulting slices. The pseudo-code for this is shown in Algorithm 1.

Algorithm 1: Calculating the Forward Model, $\boldsymbol{g} = \mathrm{H}\boldsymbol{f}$

input : object f

output: acquired data g

for $i \leftarrow 0$ **to** z_{max} **do**
  $\mathrm{temp}(x, y, i) = f(x, y, i) * *(G[x, \sigma_B(i)] \eth(x, \sigma_A) \eth(y, \sigma_L))$
for $i \leftarrow 0$ **to** x_{max} **do**
  for $j \leftarrow 0$ **to** y_{max} **do**
    $\mathrm{g}(i, j, z) = \mathrm{temp}(i, j, z) * \eth(z, \sigma_L)$
$g(x, y, z) \leftarrow e^{-\mu_I z} \; e^{-\mu_F (x - x_{\max})} \, g(x, y, z)$
return $g(x, y, z)$

2.2.2 Multi-View Deconvolution

Reformulating the RL algorithm from a single view to a multi-view deconvolution allows for two different approaches. Wu *et al.* use an ordered subset expectation maximization

(OSEM) method in which the update of the object is done for view 1, and then the update is done using view 2. The use of OSEM is done to speed up the convergence properties of the algorithm. We wanted to investigate another algorithm in which the update is done for both views at the same time. This "one step" algorithm computed using the following formula:

$$\boldsymbol{f}^{t+1} = \boldsymbol{f}^{t} \sum_{k=1}^{J} \left(\mathbf{H}_k^T \frac{\boldsymbol{g}_k}{\mathbf{H}_k \boldsymbol{f}_k^t + \boldsymbol{b}_k} \right), \tag{2.9}$$

where k $\in \{1, \ldots, J\}$, J is the number of views, T denotes the matrix transpose, $\mathbf{H}_k$ is the imaging matrix for view k, $\boldsymbol{g}_k$ is the detected image for view k, and $\boldsymbol{b}_k$ is the background for view k.

2.2.3 Edge Preserving Regularization

One of the problems with using the MLEM approach for image deconvolution is that the algorithm tends to amplify noise after a large number of iterations. This noise amplification necessitates terminating the algorithm before convergence. In an effort to get rid of the noise amplification we added a regularization term to the functional that we are trying to minimize in Eqn. (1.10). Many of the objects imaged with the diSPIM system are piecewise constant and so we want a regularization term that will smooth the amplified noise while at the same time preserving the edges of the objects. With this requirement we decided to use total variation (TV) regularization.

TV regularization adds an additional term to the optimization equation that penalizes the ℓ_1-norm of the image gradient. The result of adding this term is an image with less variation to try and minimize the image gradient. With this added term the functional we are trying to minimize becomes,

$$\Phi(\boldsymbol{f}, \boldsymbol{g}) = G(\mathbf{H}\boldsymbol{f}, \boldsymbol{g}) + \lambda_{TV}\, R(\boldsymbol{f}) \tag{2.10}$$

$$\text{where,} \qquad R(\boldsymbol{f}) = |\nabla \boldsymbol{f}|. \tag{2.11}$$

Here λ_{TV} is an adjustable parameter that we can adjust to achieve different levels of smoothing in the image. Using the results described in Dey *et al.* [9], the regularized RL update algorithm for a single view is given by,

$$\boldsymbol{f}^{t+1} = \frac{\boldsymbol{f}^t}{1 - \lambda_{TV}\ \mathrm{div}\left(\dfrac{\nabla \boldsymbol{f}^t}{|\nabla \boldsymbol{f}^t|}\right)} \left(\mathbf{H}^T \frac{\mathbf{g}}{\mathbf{H}\boldsymbol{f}^t + \boldsymbol{b}}\right). \tag{2.12}$$

Applying this to our multi-view system results in an update equation with the following form for TV regularization.

$$\boldsymbol{f}^{t+1} = \frac{\boldsymbol{f}^t}{1 - \lambda_{TV}\ \mathrm{div}\left(\dfrac{\nabla \boldsymbol{f}^t}{|\nabla \boldsymbol{f}^t|}\right)} \sum_{k=1}^{J} \left(\mathbf{H}_k^T \frac{\boldsymbol{g}_k}{\mathbf{H}_k \boldsymbol{f}_k^t + \boldsymbol{b}_k}\right) \tag{2.13}$$

2.2.4 Results

To compare the effectiveness of the two deconvolution methods, we use both qualitative and quantitative metrics. The quantitative measurements used intensity plots across a line to directly compare the ability of the reconstruction methods to recover the original image. These intensity plots are generated using the software package Fiji [31]. The final measure of effectiveness that we used was qualitative; does this produce an image that looks better than the image produced by another method. For the qualitative measure using synthetic data, we just looked at the image in one plane. For the real data, we looked at orthogonal views, as well as the maximum intensity projections in those views.

Results on Synthetic Data

Using Matlab, we created a 240 x 360 x 240 - pixel image with an array of spheres centered at the y=120 plane. A pixel size of 0.1625 μm was used to match the real data. Using the forward model described by (2.8), we simulated the blurring effect that the diSPIM system would cause. The forward model also included Poisson noise where the noisy pixel

was selected from a Poisson random process with the noise-free pixel being the mean of the distribution.

The numerical parameters used in the forward model are: $z_R = 9\ \mu m$, $\sigma_0 = 0.60\ \mu m$, and $\sigma_L = 0.20\ \mu m$. These values were either given in or derived from Wu et al. A regularization parameter of 0.001 was used to allow the algorithm to run for a large number of iterations without the amplification of noise. This parameter was deemed optimal after visually inspecting reconstructions that used a different value for regularization. Figure 2.3 shows the test image and the result of the forward model for both of the views. The first estimate is the result of taking the average of both views. Using this image as $\boldsymbol{f}^0$, we used both the "one step" and OSEM algorithms to reconstruct the simulated data. The resulting image after 1, 10, 20, and 500 iterations is shown in Figure 2.3.

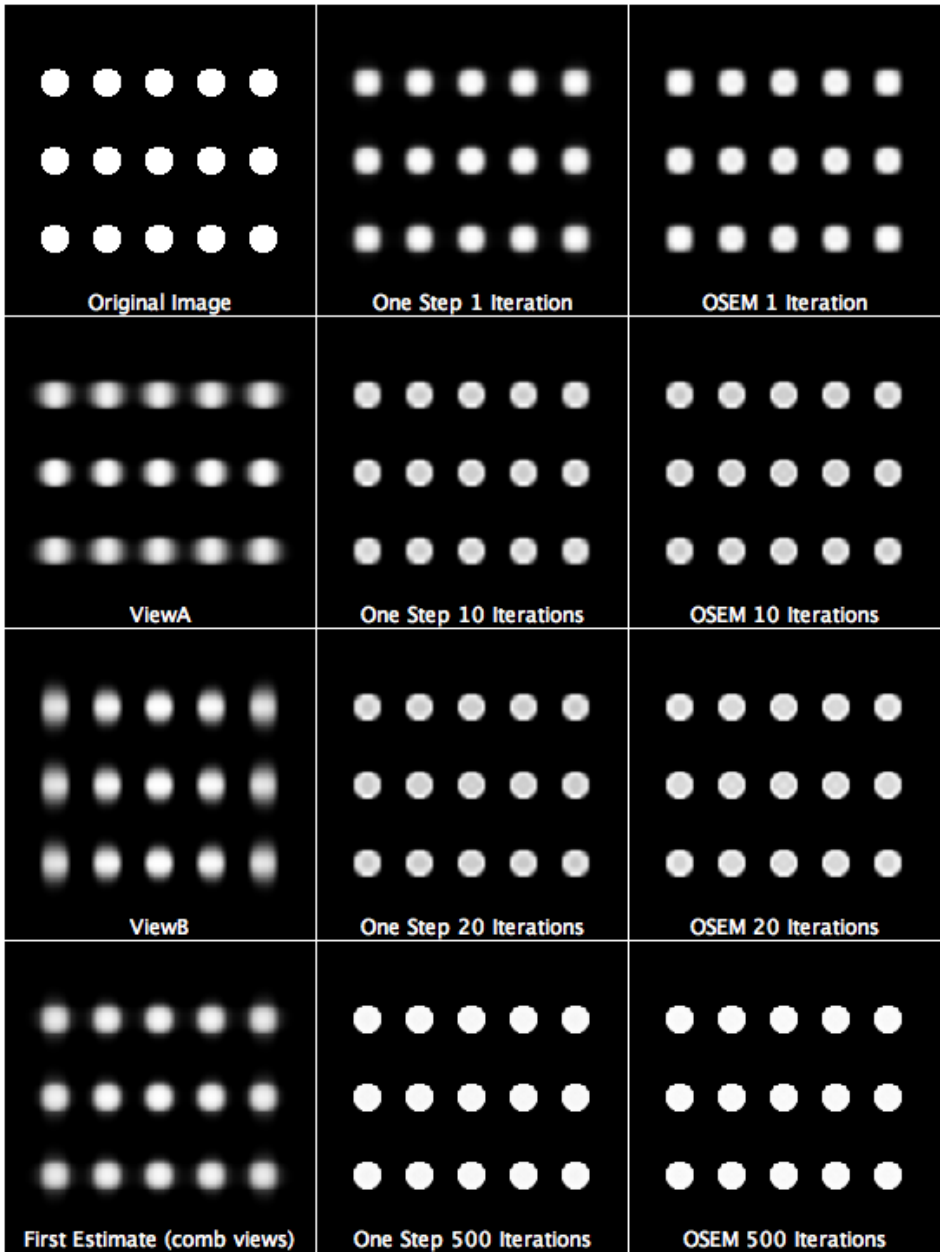

Figure 2.3: Comparing the two iterative algorithms used to deconvolve the simulated images, we see that the image quality between the two methods is very similar even with different stopping points.

Visually it seems that both algorithms recover the original image after a large number of iterations. For a more quantitative analysis, we plotted intensity profiles across a horizontal line centered at the midpoint of the image. These profiles, shown in Figure 2.4, confirm that the intensity of the reconstructed image approaches that of the original image for both of

the reconstruction methods.

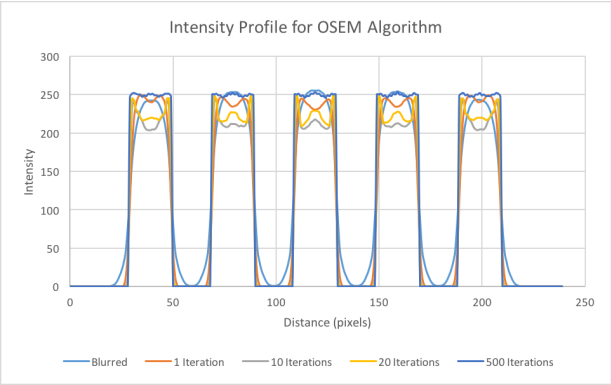

(a) Intensity profile using the OSEM algorithm.

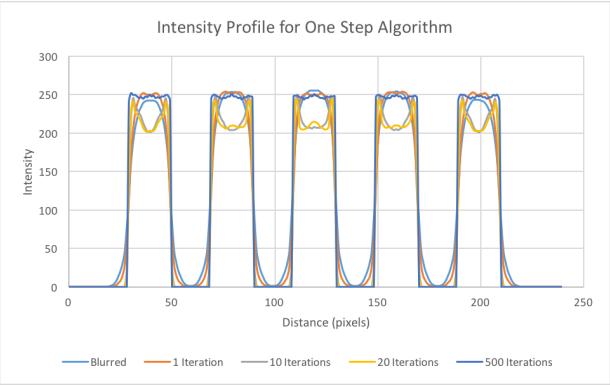

(b) Intensity profile using the "one step" algorithm.

Figure 2.4: Intensity profiles generated from the reconstructed data by the two different deconvolution algorithms.

Results on Real Data

To test the old PSF that does not account for beam widening with the new PSF that takes beam widening into account we applied both algorithms with both PSF models to real data acquired by the diSPIM imaging system. The data is of *C. elegans* cells labeled using green fluorescent protein (GFP) histone markers. The images have an isotropic voxel size of 0.1625 x 0.1625 x 0.1625 μm^3. Figure 2.5 shows the results of the deconvolution for both the old and new PSF using both the "one step" and OSEM algorithms. Without the regularization we can clearly see the amplification of noise as the number of iterations becomes large.

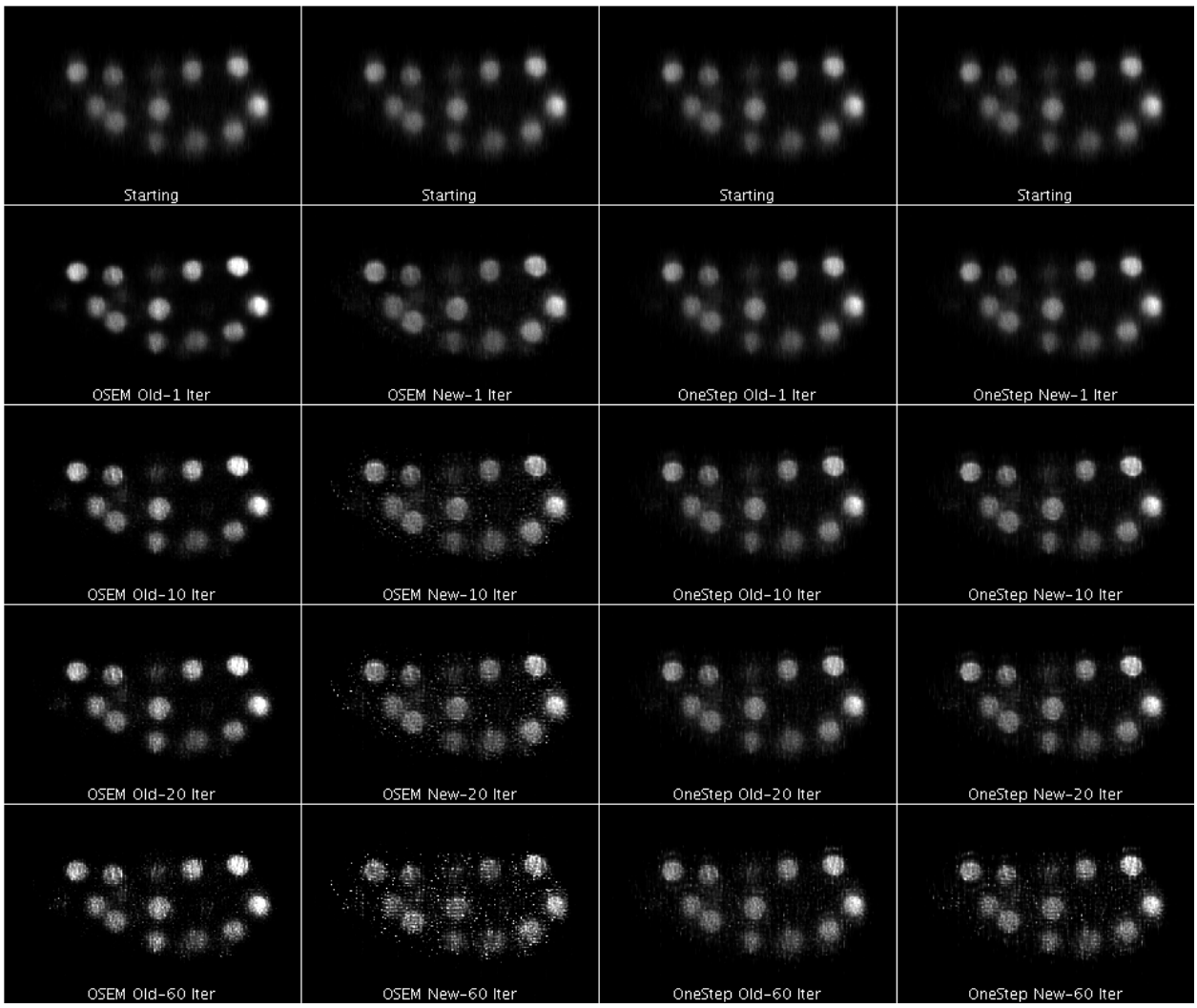

Figure 2.5: YZ views of the *C. elegans* data set after deconvolution for the two methods, for both the new and the old PSF.

Looking at the intensity profiles in Figure 2.6, we can see that after 10 and 60 iterations the one step method with the new PSF seems to produces a more uniform intensity profile than the other methods.

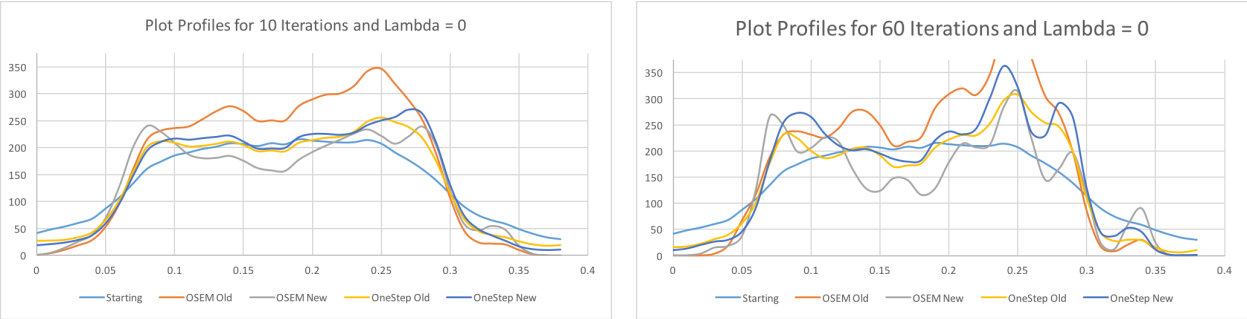

(a) **(b)**

Figure 2.6: Plot profiles for both 10 and 60 iterations with no regularization.

To reduce the amplification of noise, we added in the TV regularization to try and smooth out the images while still preserving the edges. The first lambda that we tried was 0.001 which is what we found to be the optimal parameter with the test image. Figure 2.7 shows the results of the deconvolution using each of the four algorithms with regularization. We can see that there is not much of a change in the images for this regularization parameter. There is less noise contamination in the OSEM algorithm with the new PSF for 60 iterations, but the changes are minimal for 1, 10, and 20 iterations, and is confirmed by the intensity profiles in Figure 2.8.

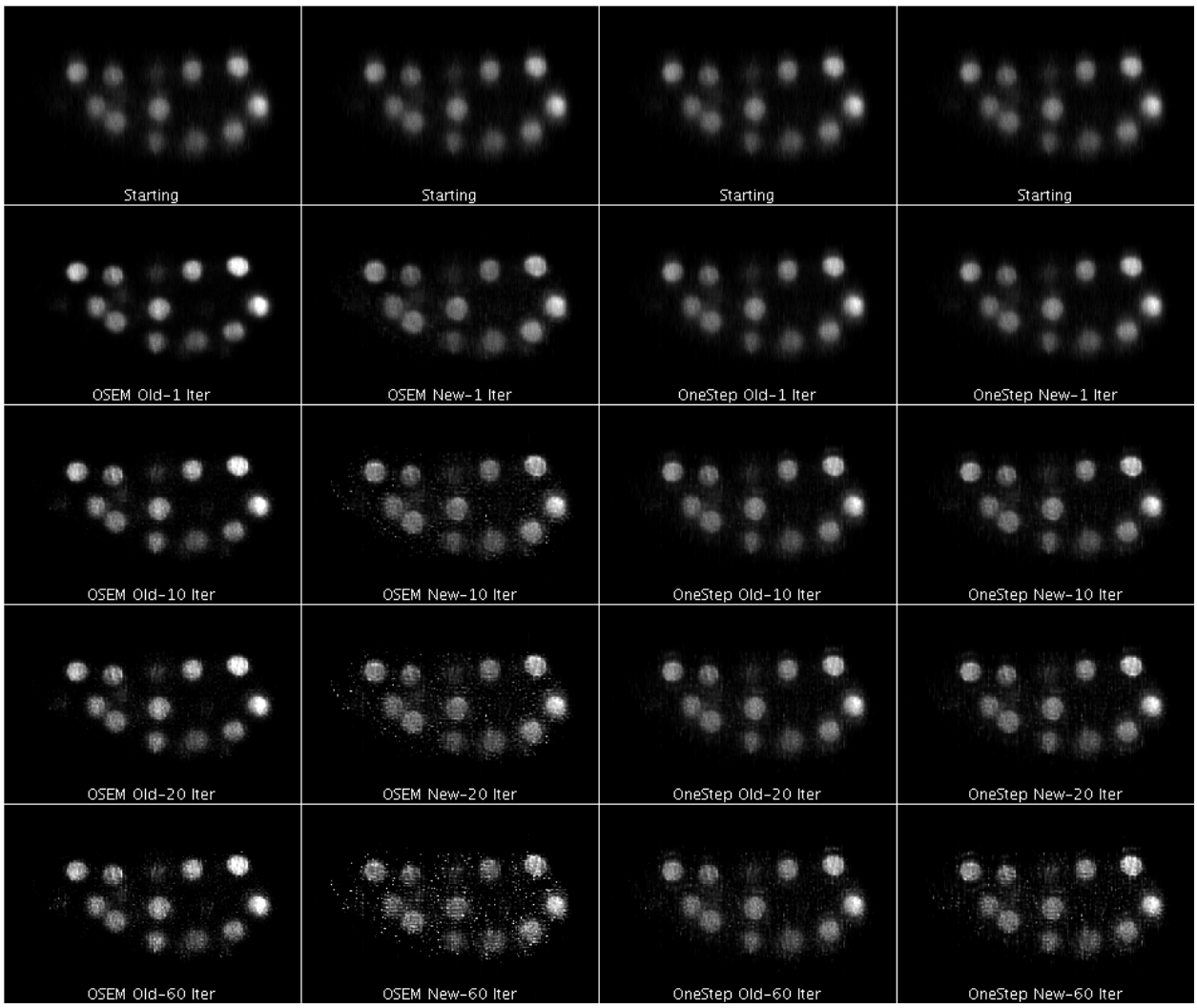

Figure 2.7: YZ views of the *C. elegans* data after deconvolution for the two methods, for both the new and the old PSF, with a regularization parameter of 0.001.

For 10 iterations, we can see that there is a slight smoothing of the peaks and valleys but the general shape of the intensity profiles is the same as if there was no regularization. There is a bit more smoothing when we get to 60 iterations. This is consistent with what we saw in Figure 2.7.

(a) **(b)**

Figure 2.8: Plot profiles for both 10 and 60 iterations with a regularization parameter of 0.001.

To try and improve the image quality even more we increased the regularization parameter to 0.005 to try and create more uniform intensity profiles. The reason for needing more regularization is a result of more noise contamination in the real data as compared to the simulations. In Figure 2.9 we can see that the images don't have as much of a checkerboard pattern as they did without regularization.

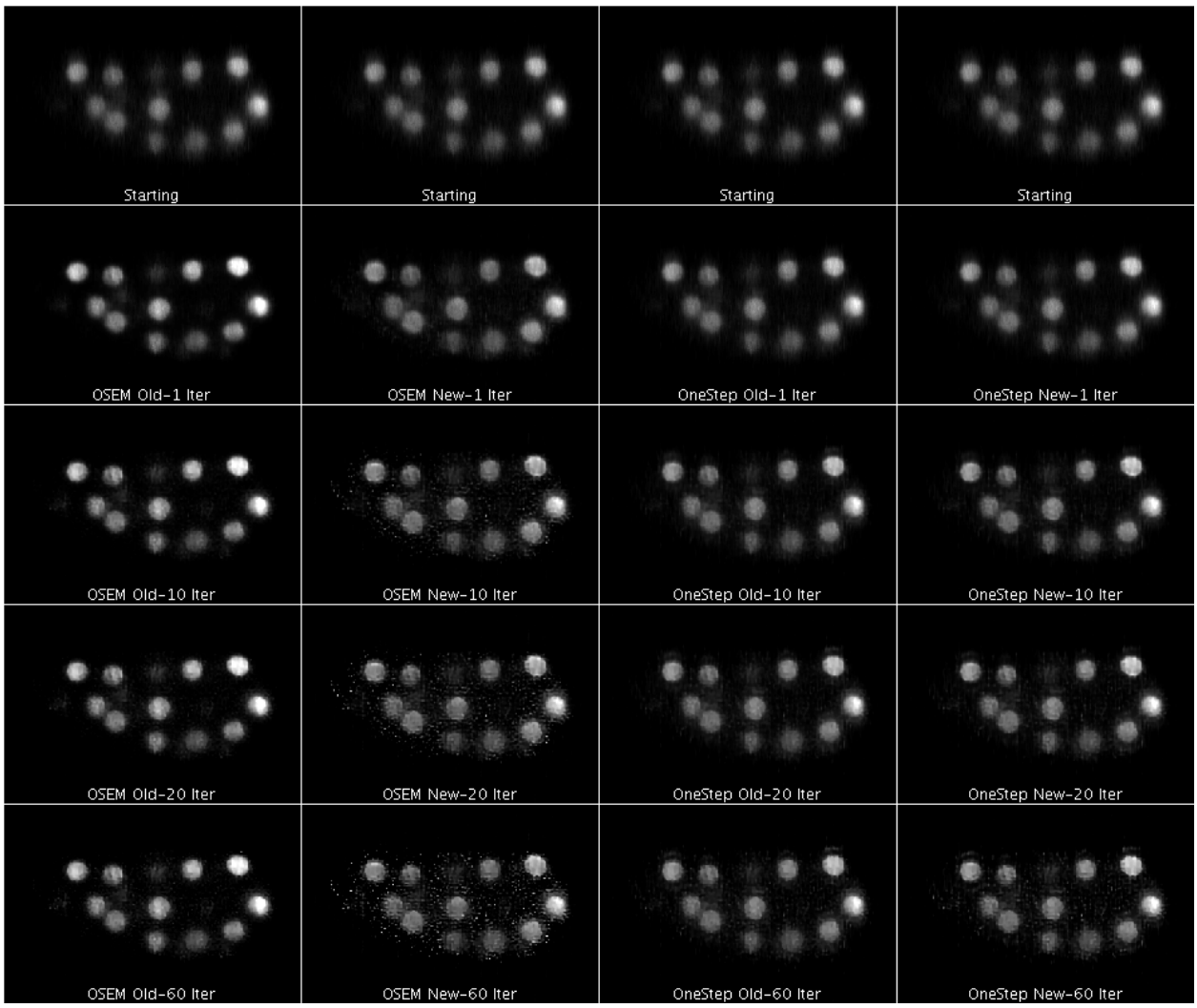

Figure 2.9: YZ views of the *C. elegans* data after deconvolution for the two methods, for both the new and the old PSF, with a regularization parameter of 0.005.

From the intensity profiles in Figure 2.10, we can see that a regularization of 0.005 creates a more uniform image. With this level of regularization, the one step algorithm with new PSF was able to achieve the most uniform profile.

Going from 10 to 60 iterations does not greatly effect the intensity profiles as it did with a smaller regularization parameter or none at all.

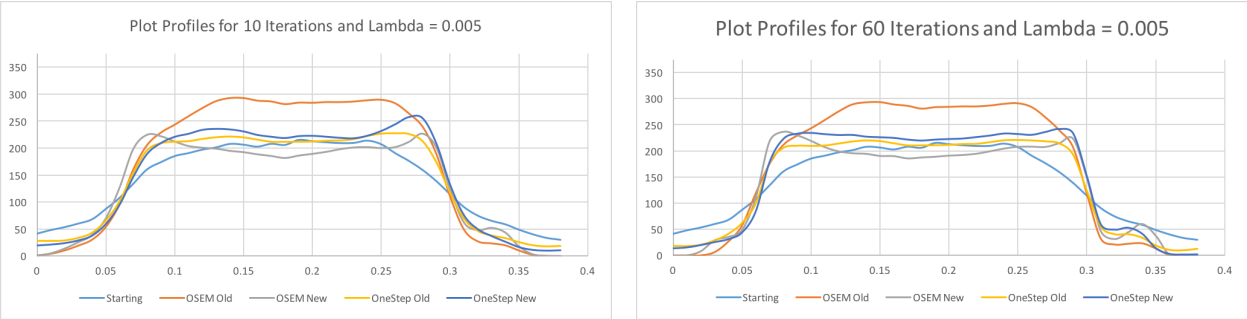

(a) **(b)**

Figure 2.10: Plot profiles for both 10 and 60 iterations with a regularization parameter of 0.001.

2.2.5 Conclusion

The results of the deconvolutions that include the effects of beam widening suggest that this correction does not have a big impact in improving the image quality. With marginal improvements, it is also important to consider that incorporating beam widening into the model will reduce the speed of the reconstruction process. The reduction in speed when using the model is more significant than the reduction that results from using regularization. Without a fully shift-invariant forward model, we needed to use a series of 1D and 2D convolutions rather than a single 3D convolution. If real-time imaging is the goal, then including beam widening might not be worth it.

One possible explanation for not seeing larger improvements in image quality is that the real data was acquired with parameters meant to try and keep the beam uniform across the sample. The scenarios under which including the beam widening will be most beneficial are when the beam has a large divergence across the sample. It is also possible that using a separable point spread function reduces the gain that we would see when incorporating for the beam thickness.

2.3 Improving diSPIM Collection Efficiency

Using only two views reduces the sample exposure compared to IsoView. However, as little as 20% of the light emitted from the sample reaches the detector in the diSPIM geometry. Emitted light not reaching the detector increases the sample exposure that contributes to phototoxicity without improving image quality. Our work aims to improve the collection efficiency of light-sheet microscopes through system design and improved image modeling.

In the case of diSPIM, steric constraints and commercial availability restrict the largest NA of symmetric perpendicular objectives to be 0.8 NA. In [40], we worked to overcome this limitation by adding a third high-NA detection objective below the sample and coverslip show in Figure 2.11.

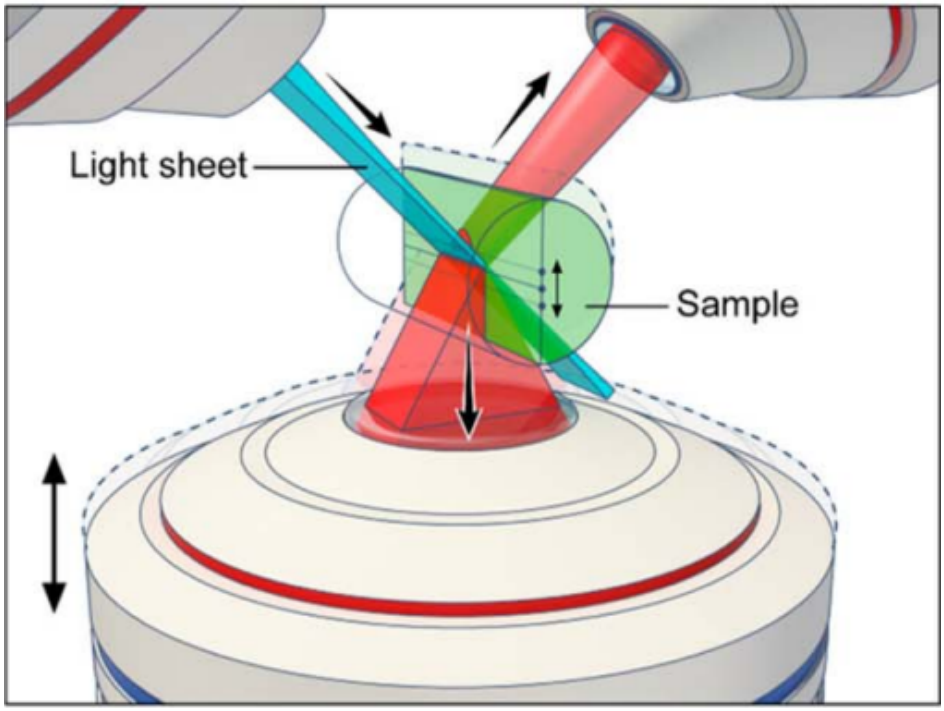

Figure 2.11: Microscope configuration for our modified diSPIM. Placing a high NA objective below the coverslip improves both the system resolution and collection efficiency. Reprinted from Yicong Wu et al. (2016). Used with permission.

The new objective is able to provide higher resolution information to the reconstruction due to its higher NA And because the third objective is only capturing light that would

otherwise be discarded, the collection efficiency is improved without increasing exposure to the sample. Compared with the diSPIM system, this system was able to double the volumetric resolution for thin samples.

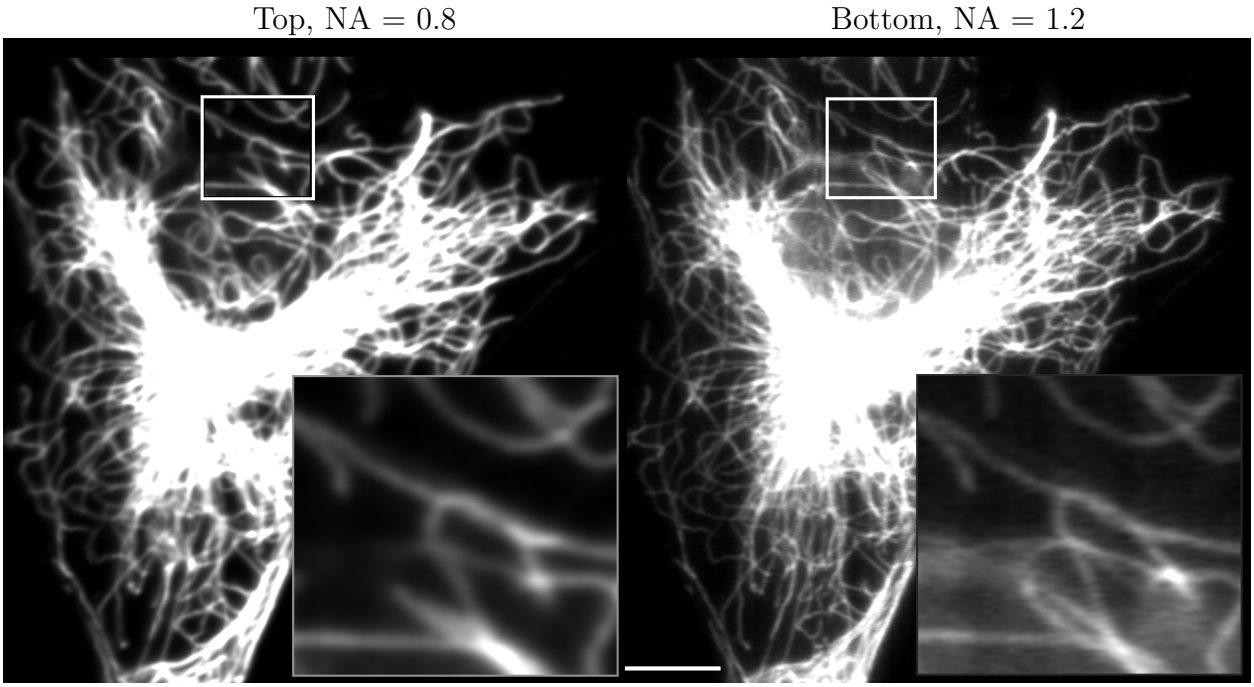

Figure 2.12: Raw data acquired on the modified diSPIM system. The image on the left is a slice acquired by a top objective and the image on the right is a slice acquired by the bottom objective. In the zoomed in images we can see that the bottom view has both better resolution and more noise. Scale bar is 10 μm. Reprinted from Yicong Wu et al. (2016). Used with permission.

2.3.1 Modeling for the New View

The biggest hurdle and where we contributed the most, was in modeling the the third objective. Due to its location, the bottom view detects more scatter than the top views do. An additional challenge is that the bottom view, unlike the top views, is not aligned perpendicular to the light-sheet. In fact, the light sheets are tilted at 45 degrees relative to the bottom objective. This means the 2D slice being excited is not entirely in the focal plane of the bottom objective. To overcome this problem, a rolling shutter on the camera's detector needs to be synchronized with the motion of the third objective as it is translated

downward. This shutter acts as a slit that blocks out light not being emitted from the focal plane. The combination of the objective motion and the rolling shutter allows this camera to capture an in-focus view of the tilted light sheet. We found that without taking into account this shutter during modeling, there was no improvement when adding the data from the bottom view. It was only once we corrected for the shutter that we saw an improvement in resolution.

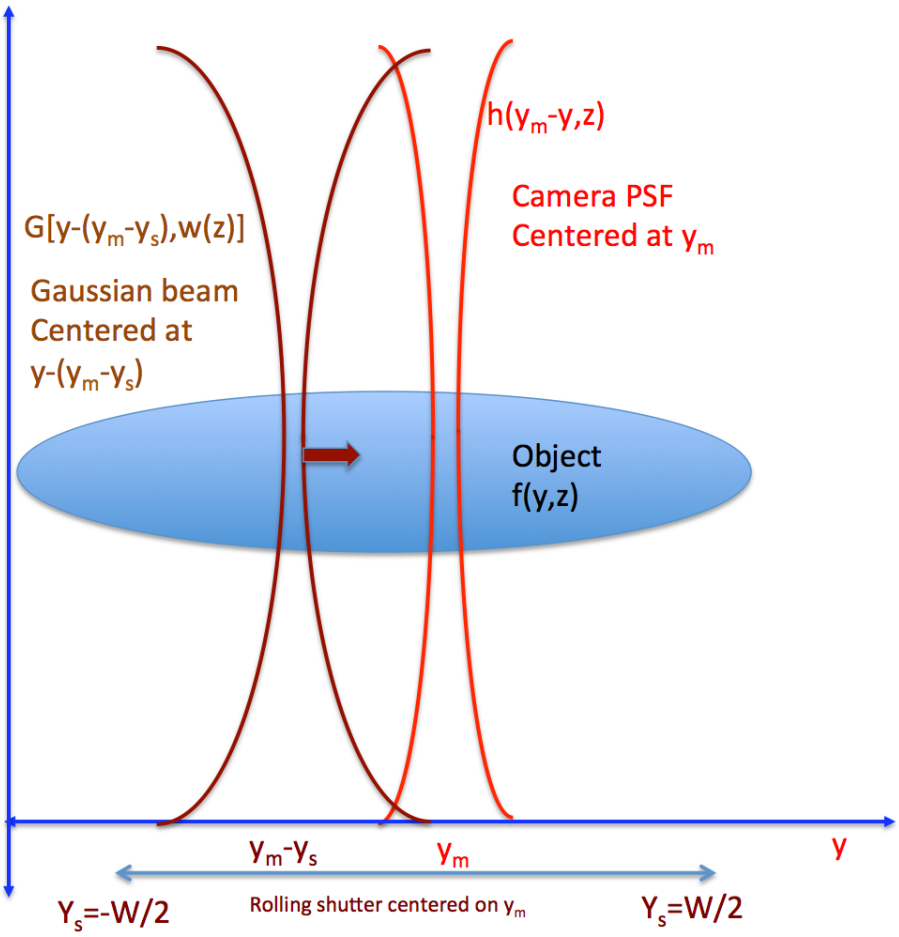

Figure 2.13: The rolling shutter on the camera with the high NA objective is synced with the shifting light-sheet to minimize out of focus light captured by the camera.

When modeling the shutter, we only need to model the forward model in two-dimensions since the light-sheet is scanned and thus constant in one of the dimensions. Figure 2.13 shows the y - z plane, with the Gaussian beam that is swept in y to create the light sheet

shown in brown and the response function of the pixel at y_m (m for measured) shown in red. The Gaussian beam is shown to be centered at $(y_m - y_s)$, where s stands for shift. The fluorophore distribution is denoted $f(y, z)$. The rolling shutter can be thought of as a slit with width W that constrains the measurement to only be responsive to shifts of the Gaussian beam between $-W/2$ and $W/2$. The measurement at y_m will be given by

$$m(y_m) = \int_{-W/2}^{W/2} \mathrm{d}y_s \int_{-\infty}^{\infty} \mathrm{d}y \, \left[h\left(y_m - y, z\right) G\left[y - \left(y_m - y_s\right), w\left(z\right)\right] f(y, z)\right] \tag{2.14}$$

$$= \int_{-\infty}^{\infty} \mathrm{d}y \, f(y, z) h\left(y_m - y, z\right) \int_{-W/2}^{W/2} \mathrm{d}y_s G\left[\left(y - y_m\right) + y_s, w\left(z\right)\right]. \tag{2.15}$$

Replacing the Gaussian beam in (2.15) with (2.2), we get an integral of the form

$$\int_{-W/2}^{W/2} \mathrm{d}y_s G\left[\left(y - y_m\right) + y_s, w\left(z\right)\right] = \left(\frac{w_0}{w(z)}\right)^2 \int_{-W/2}^{W/2} \mathrm{d}y_s \exp\left[-2\left(\left(y - y_m\right) + y_s\right)^2 / w^2(z)\right]. \tag{2.16}$$

Using a change of variables to set $a = y - y_m$ and $b = w(z)/\sqrt{2}$, we get an integral that has a known closed form solution.

$$\int_{-W/2}^{W/2} \mathrm{d}y_s \exp\left[\left(a + y_s\right)^2 / b^2\right] = \frac{1}{2}\sqrt{\pi} b \left[\mathrm{erf}\left(\frac{a + (W/2)}{b}\right) - \mathrm{erf}\left(\frac{a - (W/2)}{b}\right)\right] \tag{2.17}$$

where

$$\mathrm{erf}(x) = \frac{2}{\sqrt{\pi}} \int_0^x \mathrm{d}t \, e^{-t^2}. \tag{2.18}$$

Plugging (2.17) back into (2.16) yields

$$\int_{-W/2}^{W/2} \mathrm{d}y_s G\left[(y-y_m)+y_s, w\left(z\right)\right] = \tag{2.19}$$

$$\left(\frac{w_0}{w(z)}\right)^2 \frac{1}{2}\sqrt{\pi}\frac{w(z)}{\sqrt{2}}\left[\mathrm{erf}\left(\frac{(y-y_m)+(W/2)}{\frac{w(z)}{\sqrt{2}}}\right) - \mathrm{erf}\left(\frac{(y-y_m)-(W/2)}{\frac{w(z)}{\sqrt{2}}}\right)\right]. \tag{2.20}$$

This final expression only depends on the difference between $y_m - y$ and z, just as the PSF in (2.15) does.

If we let

$$s(y,z) = \left(\frac{w_0}{w(z)}\right)^2 \frac{1}{2}\sqrt{\pi}\frac{w(z)}{\sqrt{2}}\left[\mathrm{erf}\left(\frac{y+(W/2)}{\frac{w(z)}{\sqrt{2}}}\right) - \mathrm{erf}\left(\frac{y-(W/2)}{\frac{w(z)}{\sqrt{2}}}\right)\right], \tag{2.21}$$

then the measurement with the rolling shutter has the form,

$$m(y_m) = \int_{-\infty}^{\infty} \mathrm{d}y\, f(y,z) h\left(y_m - y, z\right)\, s\left(y_m - y, z\right). \tag{2.22}$$

So rather than having to explicitly account for the Gaussian beam excitation and the rolling shutter on the detector, we can modify the generic PSF $h(y,z)$ by multiplying it by a correction factor that accounts for both factors.

This gives an effective PSF of that we use in our forward model for the bottom view in Figure 2.11

$$h_{\mathrm{eff}}(x,y,z) = h(x,y,z)\, s(y,z). \tag{2.23}$$

This also allows us to write the forward model for the three-view system as a convolution between the fluorophore distribution and the effective PSF for each view,

$$g_k(\boldsymbol{r}) = \int \mathrm{d}\boldsymbol{r'}\, f(\boldsymbol{r'})\, h_k(\boldsymbol{r}-\boldsymbol{r'}) \tag{2.24}$$

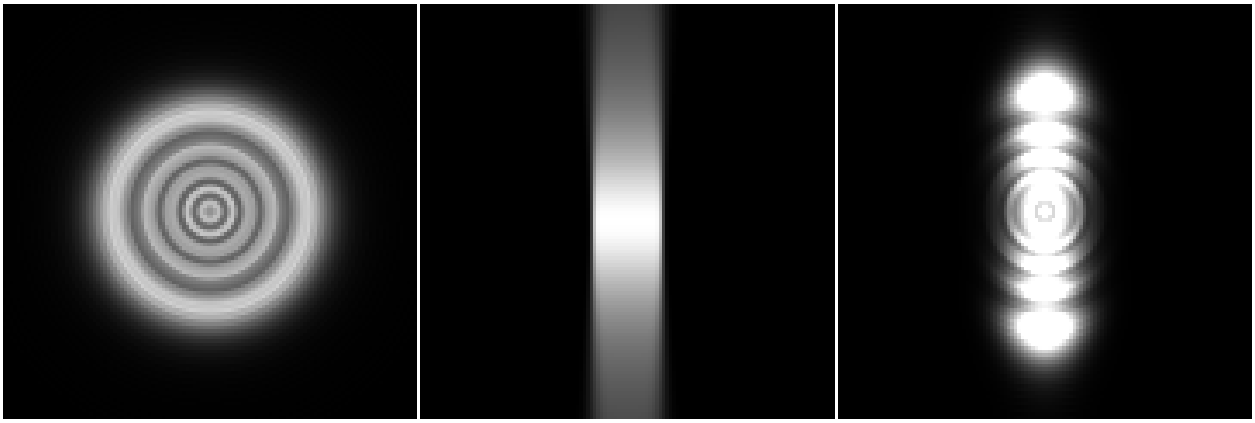

Figure 2.14: Modifying the PSF based on a correction factor from using a rolling shutter during image acquisition. The image on the left is a slice away from the focal plane through the PSF without any corrections for the shutter. The image is saturated for better visualization. The image in the center is the correction factor of the rolling shutter that is derived in (2.21). Finally, the image on the right is the corrected PSF that we use for reconstruction.

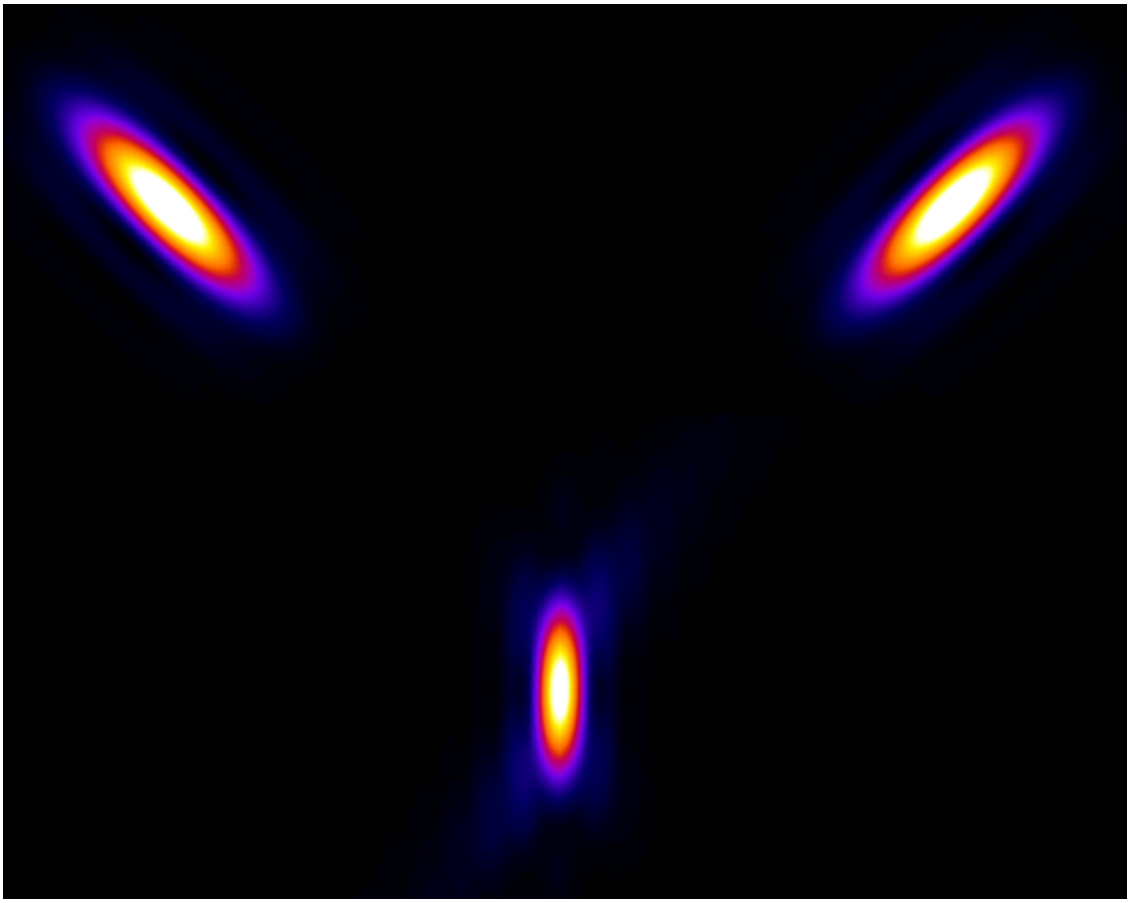

Figure 2.15: In the three-view diSPIM system, the two-top detection PSFs can be modeled as the product of the light sheet and a widefield PSF for a 0.8 NA objective. The bottom detection is modeled as the product of the light sheet with a convolution between a 1 μm slit and a widefield PSF for a 1.2 NA objective. The effects of the slit on the bottom objective can be seen in the 'wings' of the final PSF.

2.3.2 Estimation Theory for Noise and Resolution Trade-offs

A challenge with this microscope is that due to the location of the third objective, a rolling shutter on the detector is needed to reject out of focus light. This reduces the photon flux on the detector causing an increase in noise compared to the other two views. Given that this view contains both better resolution but also more noise than the top two views, we want to be able to estimate the SNR for both the two- and three-view diSPIM geometries.

In the section we use a Gaussian noise model rather than the Poisson noise model used

in previous sections. Using a Gaussian model as the data fidelity term offers us a closed-form solution to the inverse problem. The reason we make the change is that unlike the previous sections where we are trying to accurately model the system, here we are looking at comparing the information preserved by different imaging configurations, rather than explicitly trying to predict the output. Using a more accurate noise model that contains both Poisson and Gaussian noise would likely change the scale of the estimates derived here, but should preserve the comparisons between different system configurations.

We begin by assuming that the noise vector $\boldsymbol{n}$ in (1.5) is a zero-mean Gaussian random vector with covariance matrix $\mathbf{K}$. If the noise is uncorrelated from pixel to pixel, $\mathbf{K}$ will be a diagonal matrix with the variance σ_i^2 along the diagonal. For regularized least squares, the cost function in (1.7) being minimized is

$$\Phi(\boldsymbol{f}, \boldsymbol{g}) = \frac{1}{2}\left[(\boldsymbol{g} - \mathbf{H}\boldsymbol{f})^T \mathbf{K}^{-1}(\boldsymbol{g} - \mathbf{H}\boldsymbol{f}) \; + \; \alpha||\boldsymbol{f}||_2^2\right]. \tag{2.25}$$

For this case, there exists an explicit expression for the estimator

$$\begin{aligned} \hat{\boldsymbol{f}} &= \left[\mathbf{H}^T\mathbf{K}^{-1}\mathbf{H} + \alpha\mathbf{I}\right]\mathbf{H}^T\mathbf{K}^{-1}\boldsymbol{g} \\ &= \left[\mathbf{F} + \alpha\mathbf{I}\right]\mathbf{H}^T\mathbf{K}^{-1}\boldsymbol{g}, \end{aligned} \tag{2.26}$$

where $\mathbf{F} = \mathbf{H}^T\mathbf{K}^{-1}\mathbf{H}$. To measure the noise and resolution of this estimator, we want to be able to derive the point spread function for the estimator and the covariance matrix for the estimator.

Work done by [2, 28, 12, 13] has build a framework for this very task. Instead of deriving the PSF, we derive the local impulse response (LIR) function. The reason that we can't use a PSF is that the resolution in the reconstructed image is position dependent. Qi *et al.* proposed the idea of a contrast recovery coefficient (CRC) [28]. The CRC_i is the peak intensity of the LIR centered at the pixel i. The reasoning behind CRC is that the intensity in the reconstructed image is conserved, and so a larger peak will correspond to a narrower

LIR. Having a single value for resolution allows for faster comparisons between different imaging models and reconstruction methods. We can plug (2.25) into equations derived in [28] to compute CRC and the covariance matrix for the estimator.

$$\mathrm{CRC}_i(f) = (\boldsymbol{e}_i)^T \left[\mathbf{F} + \alpha\mathbf{I}\right]^{-1} \mathbf{F}\boldsymbol{e}_i, \tag{2.27}$$

$$\mathbf{K}^{\hat{f}} = \left[\mathbf{F} + \lambda\mathbf{I}\right]^{-1} \mathbf{F} \left[\mathbf{F} + \alpha\mathbf{I}\right]^{-1}. \tag{2.28}$$

For the light-sheet systems we are comparing, we can write the forward models as a convolution between a system PSF and the sample. In the discrete domain, this allows us to write the system matrix $\mathbf{H}$ as a circulant matrix, $\mathbf{A}$. A circulant matrix is a special matrix where each row is just the previous row shifted one element to the right (with wrap around). A special property of circulant matrices is that they are diagonalized using the discrete Fourier transform $\mathbf{Q}$.

$$\mathbf{\Gamma}^{(j)} = \mathrm{diag}\left\{\left|\mathbf{O}_i^{(j)}\right|^2\right\} = \mathbf{Q}^\dagger \mathbf{A}^{T\,(j)} \mathbf{A}^{(j)} \mathbf{Q}, \tag{2.29}$$

where the $\mathbf{O}_i^{(j)}$ are the OFT elements of the matrix $\mathbf{A}^{(j)}$. If we assume the noise is uniform for each image, the covariance matrix for a single acquisition is $\mathbf{K}_j = \sigma_j \mathbf{I}$. Making these substitutions for $\mathbf{F}$ gives

$$\mathbf{F} = \sum_{j=1}^{J} \left[\left(\frac{1}{\sigma^{(j)}}\right)^2 \mathbf{E}^{t\,(j)} \mathbf{Q}^\dagger \mathbf{\Gamma}^{(j)} \mathbf{Q} \mathbf{E}^{(j)}\right]. \tag{2.30}$$

In the case where the excitation is uniform (or approximately uniform) across the sample,

we can write out a closed form solution for both the CRC and variance of the estimate.

$$\mathrm{CRC}_i = \frac{1}{N}\sum_{i=1}^{N} \frac{\sum_{j=1}^{J}\left[\left(\frac{1}{\sigma^{(j)}}\right)^2 \left|\mathbf{O}_i^{(j)}\right|^2\right]}{\left(\sum_{j=1}^{J}\left[\left(\frac{1}{\sigma^{(j)}}\right)^2 \left|\mathbf{O}_i^{(j)}\right|^2\right] + \alpha\right)} \tag{2.31}$$

$$\mathrm{Var}\{\hat{\boldsymbol{f}}_k\} = \frac{1}{N}\sum_{i=1}^{N} \frac{\sum_{j=1}^{J}\left[\left(\frac{1}{\sigma^{(j)}}\right)^2 \left|\mathbf{O}_i^{(j)}\right|^2\right]}{\left(\sum_{j=1}^{J}\left[\left(\frac{1}{\sigma^{(j)}}\right)^2 \left|\mathbf{O}_i^{(j)}\right|^2\right] + \alpha\right)^2} \tag{2.32}$$

If the noise is uncorrelated from pixel to pixel and is uniform for each image, the covariance matrix for a single acquisition is $\mathbf{K}_j = \sigma_j \mathbf{I}$. In this case we can write out a simple closed form solution for both the CRC and variance of the estimate by exploiting the circulant structure of our system matrices. This structure allows us to use the Fourier transform to diagonalize A and turn both the CRC and variance into sums over the optical transfer function (OTF) elements.

$$\mathrm{CRC}_i = \frac{1}{N}\sum_{k=1}^{N} \frac{\lambda_k}{(\lambda_k + \alpha\,\omega_k)} \qquad \mathrm{Var}\{\hat{\boldsymbol{f}}_k\} = \frac{1}{N}\sum_{k=1}^{N} \frac{\lambda_k}{(\lambda_k + \alpha\,\omega_k)^2} \tag{2.33}$$

where

$$\lambda_i = \sum_{j=1}^{J}\left[\left(\frac{1}{\sigma^{(j)}}\right)^2 \left|\mathbf{O}_i^{(j)}\right|^2\right] \tag{2.34}$$

ω_k are the diagonal elements of the matrix $\mathbf{Q}\mathbf{D}^T\mathbf{D}\mathbf{Q}^\dagger$ with $\mathbf{Q}$ representing the discrete Fourier transform and $\mathbf{Q}^\dagger$ representing the inverse Fourier transform.

2.3.3 Results

Using (2.33), we can trace out noise and resolution curves where CRC is the proxy for resolution and variance is the proxy for noise. The curve is computed by sweeping out the regularization parameter α. The PSFs we used are the ones depicted in Figure 2.15. The resulting plots are shown in Figures 2.16 and 2.17.

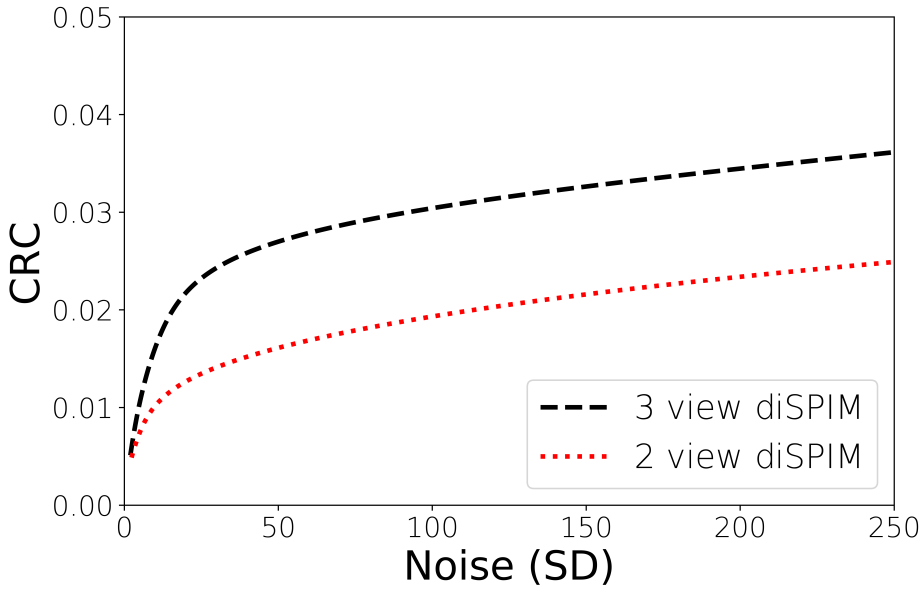

Figure 2.16: Noise and CRC curves for both the two- and three-view diSPIM configurations. The noise for each top view is $\sigma^2_{1,2} = 50$ and the noise for the bottom view is $\sigma^2_3 = 2500$.

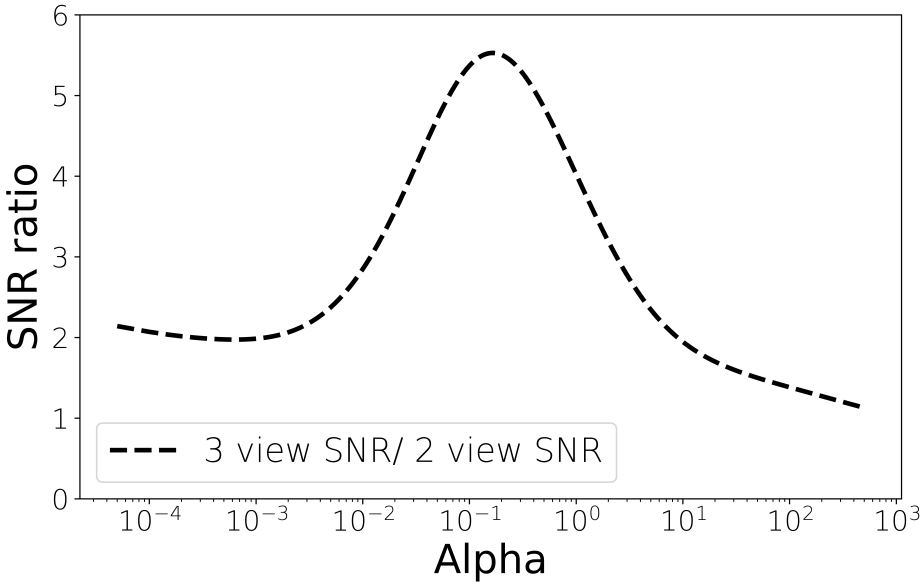

Figure 2.17: The ratio between the two configurations SNR curves. From the plot we can determine that for every α the SNR of the three-view configuration is better.

2.3.4 Conclusion

An issue with the diSPIM configuration is that the numerical aperture (NA) of the two views is limited in order to keep the two views orthogonal to each other. We worked to overcome this limitation by adding a third high-NA detection objective below the sample and cover slip [40]. The new objective is able to provide higher-resolution information to the reconstruction due to its larger NA. And because the third objective is only capturing light that would otherwise be discarded, the collection efficiency is improved without increasing exposure to the sample. Compared with the diSPIM microscope, this system was able to double the volumetric resolution for thin samples.

To see if adding this third view to the diSPIM setup would always improve image quality, we used results from estimation theory to compute the noise and resolution for each system after reconstruction. Based on these results, we were able to determine that even though the bottom objective contains more noise, the addition of the third view improves the SNR compared with the original diSPIM. Furthermore, we can conclude that the addition of the third view improves resolution for all noise levels in the final reconstructed image. This is important to show as it validates our claim that resolution is improved in the three-view system.

2.4 Imaging Thicker Samples with Reflective diSPIM

While adding this third view improved resolution for thin samples, it did not translate to samples that were thicker than $\sim 12\mu$m. For imaging thicker samples, we modified the diSPIM system to acquire images of samples on reflective cover slips [39].

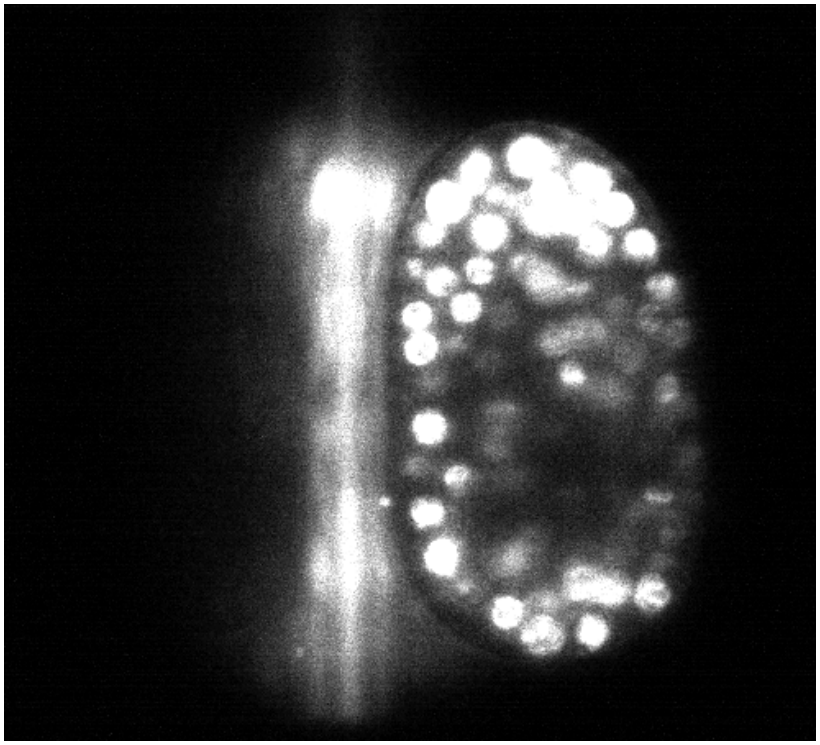

Figure 2.18: Image of a EGFP-histone-labeled nuclei in a live nematode embryo acquired in a 0.8/0.8 NA symmetric diSPIM geometry with a mirrored coverslip. The epi-fluorescence contamination in the center of the image is caused by the reflective coverslip and needs to be removed during image reconstruction. Reprinted from Yicong Wu et al. (2017). Used with permission.

The difficulty with using a reflective coverslip is that the images are contaminated with out-of-focus epi-fluorescence as shown in Figure 2.19. To remove the contamination, a more rigorous modeling of the microscope was necessary. In conventional SPIM, the imaging model is assumed to be linear shift-invariant with an Airy disk PSF modified slightly by the light-sheet thickness. In the case of reflective imaging, we needed to use a shift-varying forward model.

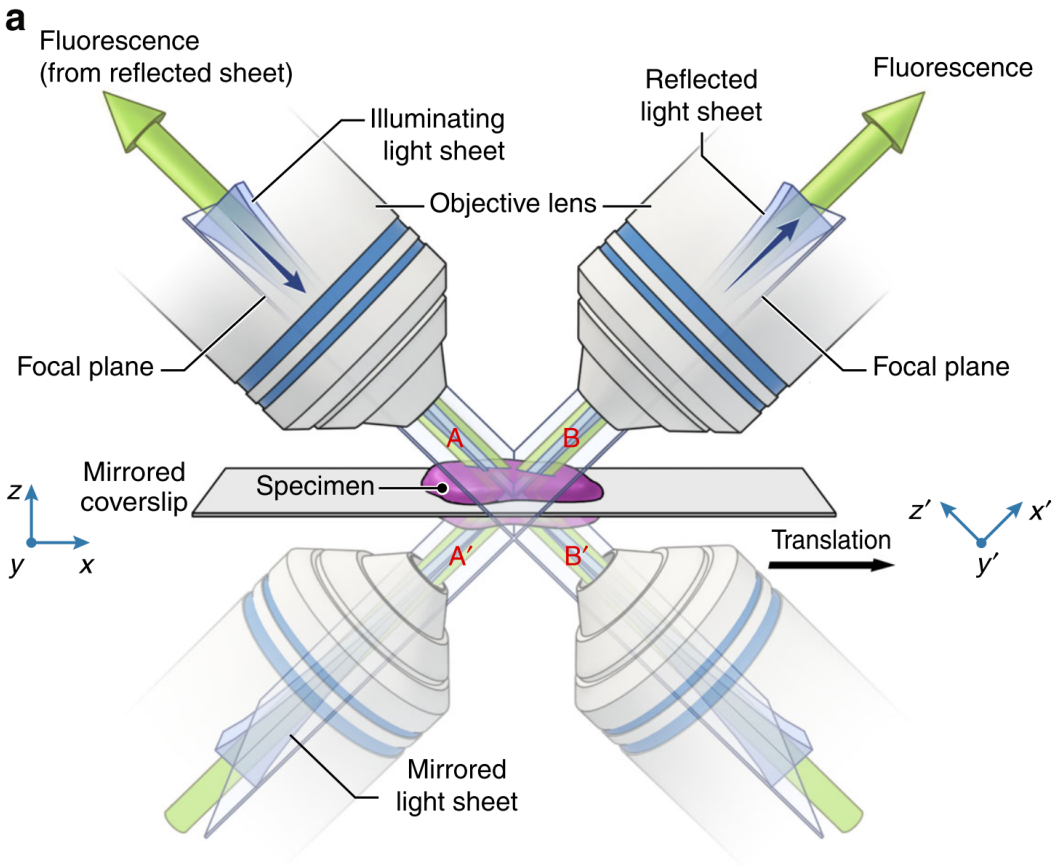

Figure 2.19: A schematic showing the geometry of the symmetric diSPIM with a reflective coverslip. The mirrored coverslip creates virtual objectives reflected across the coverslip plane and results in four views of the sample being acquired, A, B, A', and B'. Reprinted from Yicong Wu et al. (2017). Used with permission.

2.4.1 Forward Model for Reflective Imaging

To account for the mirrored coverslip, the object f is reflected across the coverslip

$$\tilde{f}(x,y,z) = \begin{cases} f(x,y,z) & z \geq -x \\ f(-z,y,-x) & z < -x \end{cases}. \tag{2.35}$$

In the case of symmetric objectives, we can write the forward model for a single position of the sample in the light-sheet as

$$g^{\mathrm{A}}(x', y')\big|_{z'=-\delta} = \iiint \mathrm{d}x\,\mathrm{d}y\,\mathrm{d}z \left[\tilde{f}(x, y, z)E(x-\delta, y, z+\delta)h_{\mathrm{A}}(x-x', y-y', z+\delta)\right] \tag{2.36}$$

$$E(x, y, z) = G(x, y, w(z)) + G(z, y, w(x)) \tag{2.37}$$

$$G(x, y, w(z)) = (w_0/w(z))^2 \exp\left[-2x^2/w^2(z)\right], \tag{2.38}$$

where $w(z) = w_0\sqrt{1+(z/Z_R)^2}$, w_0 is the beam waist, Z_R is the Rayleigh length given by $\pi w_0^2/\lambda_{ex}$, λ_{ex} is the excitation wavelength, and h_{A} represents the emission PSF for objective A. To create a 3D stack, the sample is shifted through the light-sheet a distance $\sqrt{2}\delta$, $+\delta$ in x and -$\delta\tan(\theta)$ in z.

Converting to Light Sheet Scanning Mode

The previous equations assume that the sample is being shifted while the light sheets are fixed. It is equivalent to think about the sample being fixed and the light sheets being scanned across the sample.

Conversion from stage-scanning stacks to light-sheet scanning stacks can be achieved by the following transformations:

$$g^A_{LS}(x'', y'', z'') = g^A_{SS}(x''+z'', y'', z'') \tag{2.39}$$

and

$$g^B_{LS}(x'', y'', z'') = g^B_{SS}(x'', y'', z''+x''). \tag{2.40}$$

The first equation says that the value of the light sheet stack at (x'', y'', z'') is obtained by indexing the stage scanning scanning stack at $\delta = z''$ and setting $x' = x'' + z''$ and

$y' = y''$. Note that the variables (x'', y'', z'') are in the same coordinate system as (x, y, z). One set represents dummy variables that are being averaged over since some finite chunk of fluorophores in the (x, y, z) variables is contributing to our measurement in the (x'', y'', z'') variables.

Let's focus on the stack measured by objective A. If we substitute (**??**) into (2.39) we have

$$g^A_{LS}(x'', y'', z'') = \iiint \mathrm{d}x\,\mathrm{d}y\,\mathrm{d}z\,\widetilde{f}(x - z'', y, z + z'')E(x, y, z)h_A(x - \left(x'' + z''\right), y - y'', z). \tag{2.41}$$

Now we change coordinates

$$\begin{aligned} \widetilde{x} &= x - z'' \\ \widetilde{y} &= y \\ \widetilde{z} &= z + z''. \end{aligned} \tag{2.42}$$

yielding,

$$\begin{aligned} & g^A_{LS}(x'', y'', z'') \\ &\quad = \iiint \mathrm{d}\widetilde{x}\,\mathrm{d}\widetilde{y}\,\mathrm{d}\widetilde{z}\,\widetilde{f}(\widetilde{x}, \widetilde{y}, \widetilde{z})E(\widetilde{x} + z'', \widetilde{y}, \widetilde{z} - z'')h_A(\widetilde{x} + z'' - \left(x'' + z''\right), \widetilde{y} - y'', \widetilde{z} - z'') \\ &\quad = \iiint \mathrm{d}\widetilde{x}\,\mathrm{d}\widetilde{y}\,\mathrm{d}\widetilde{z}\,\widetilde{f}(\widetilde{x}, \widetilde{y}, \widetilde{z})E(\widetilde{x} + z'', \widetilde{y}, \widetilde{z} - z'')h_A(\widetilde{x} - x'', \widetilde{y} - y'', \widetilde{z} - z''). \end{aligned} \tag{2.43}$$

If we substitute for the illumination function, we obtain two terms:

$$
\begin{aligned}
&g^{A}_{LS}(x'', y'', z'') \\
&\qquad = \iiint \mathrm{d}\widetilde{x}\,\mathrm{d}\widetilde{y}\,\mathrm{d}\widetilde{z}\,\widetilde{f}(\widetilde{x},\widetilde{y},\widetilde{z})G(\widetilde{z}-z'', \sigma(\widetilde{x}+z''))h_A(\widetilde{x}-x'', \widetilde{y}-y'', \widetilde{z}-z'') \\
&\qquad + \iiint \mathrm{d}\widetilde{x}\,\mathrm{d}\widetilde{y}\,\mathrm{d}\widetilde{z}\,\widetilde{f}(\widetilde{x},\widetilde{y},\widetilde{z})G(\widetilde{x}+z'', \sigma(\widetilde{z}-z''))h_A(\widetilde{x}-x'', \widetilde{y}-y'', \widetilde{z}-z''). \qquad (2.44)
\end{aligned}
$$

The first term here represents conventional in-focus imaging of the light sheet that is parallel to objective A. The second term represents epifluorescence contamination.

Converting to Discrete Imaging Model

So far everything has been in a continuous notation. For implementation of R-L we need to start thinking in a discrete notation. We start with the light sheet scanning mode imaging equation

$$
g^{A}_{SS}(x', y', \delta) = \iiint \mathrm{d}x\,\mathrm{d}y\,\mathrm{d}z\widetilde{f}(x-\delta, y, z+\delta)E(x,y,z)h_A(x-x', y-y', z). \qquad (2.45)
$$

This equation comprises 4 cascaded operations. We loop over δ and for each δ, we

1. Shift f by δ in x and $-\delta$ in z. We represent this by a shifting matrix S.

2. Multiply by the illumination function. We represent this by a matrix D since this would be a diagonal matrix (scaling each element in the vector representng the object by the illumination).

3. Loop over z in the object and at each z, convolve with with lens response function. This could be represented by an appropriate block circulant matrix with circulant blocks H.

4. Collapse over the z coordinate. This could be represented by a projection matrix P having 1's in appropriate locations since it will lead to summing of the appropriate

elements.

For a given position of the light sheets demoted byδ, the detected image is now written as

$$g_{\delta}^{\mathrm{A}} = \mathbf{PAE}_{\delta}\tilde{f}, \tag{2.46}$$

where $\mathbf{E}_{\delta}$ is the excitation matrix shifted by $+\delta$ in x and $-\delta\tan(\theta)$ in z, $\mathbf{A}$ represents a 2D convolution with the detection PSF at every slice z, and $\mathbf{P}$ is a projection operator that sums the convolved elements along the z-axis. From (2.46), we can use the RL framework in (1.11) for reconstructing the two image stacks.

2.4.2 Simulations

To validate this forward model, we ran simulations of the forward model applied to known phantoms. We could then use the simulated data to see if it was consistent with the data that had already been acquired on a prototype of the system. Figures 2.20 and 2.21 show the simulated forward model when we applied it to a 3D phantom of spheres.

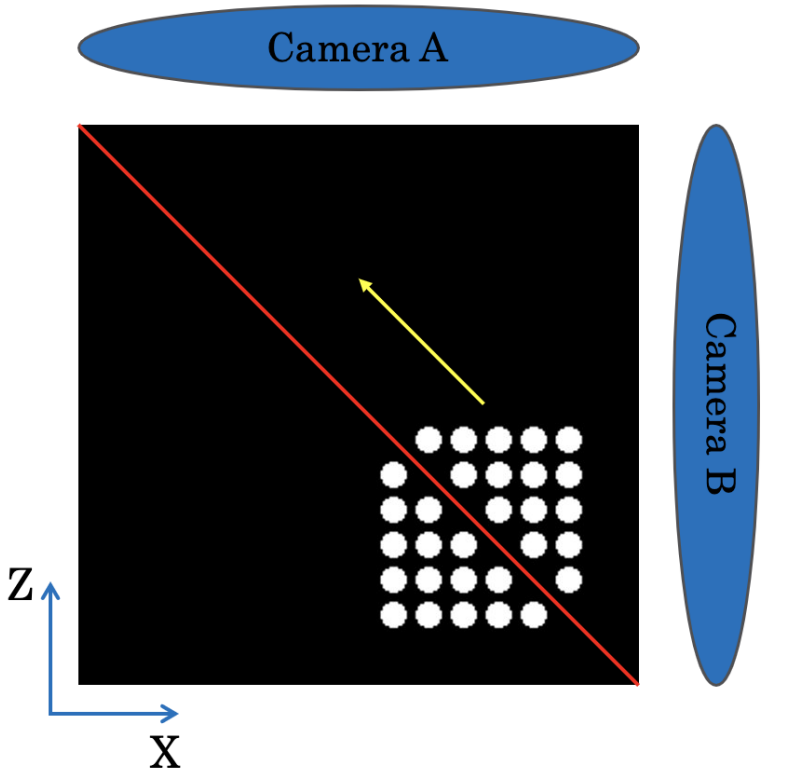

Figure 2.20: Geometry used for simulating the acquisition of data when using a reflective coverslip. The object includes both the real and mirrored phantom and is shifted along the coverslip shown in red.

Figure 2.21: Simulated acquisition data when using a reflective coverslip with a diSPIM system. We can see that in stage-scanning mode the sample has been compressed in the z dimension and expanded in the x dimension.

The data in Figure 2.21 has similar characteristics to the real data that was acquired on the prototype system and is shown in Figure 2.23.

In addition to being able to verify that the forward model was an accurate representation of the new system, it allowed us to confirm that our reconstruction implementation was

correct. Using noise-free simulation data, we should be able to recover the underlying object if the reconstruction algorithm is working properly. Figure 2.22 shows some of the initial reconstructed images after a small number of iterations.

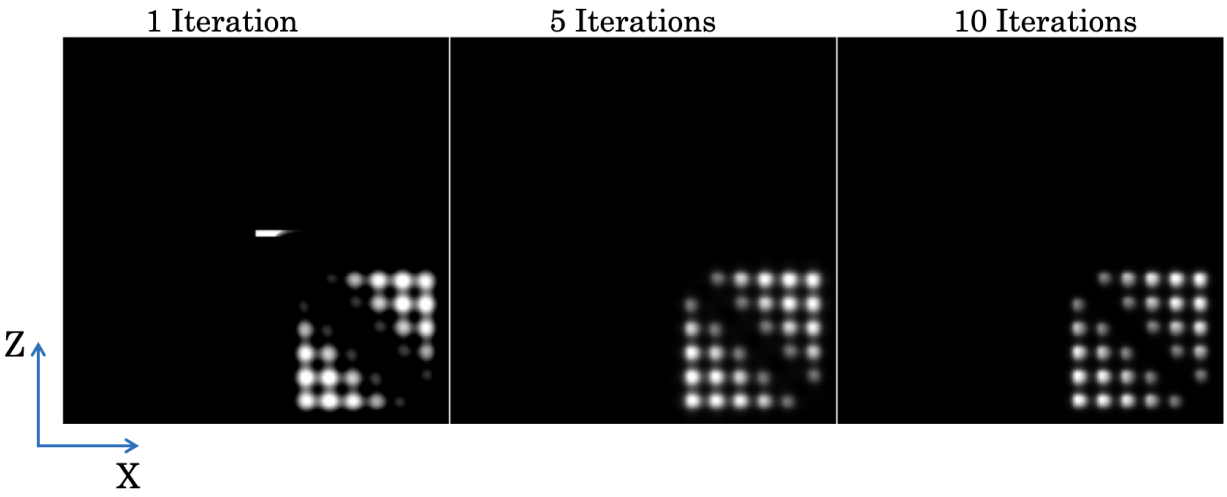

Figure 2.22: Reconstructed images using the noiseless simulations shown in Figure 2.21. As the number of iterations increases we can see that the spheres start to become more well defined, but that the spheres closer to the coverslip have a much small diameter than the phantom has.

Our initial reconstructions were very promising, but there was a major obstacle the the reconstructions. So far, all of the simulations and reconstructions had been implemented in Python, the problem was that a single iteration of the reconstruction was taking over 24 hours to run. This is not feasible if we wanted to use the system for real lab work.

In an effort to improve performance, the code was first ported to C and then to CUDA to see if the reconstruction runtime could be improved. Moving to C did improve performance but it was still too long with each iteration taking over 10 hours to run. Moving to CUDA and running the reconstructions on the GPU saw a much larger boost in performance. On the GPU, each iteration was taking around one hour to run which was fast enough to test the code on real data.

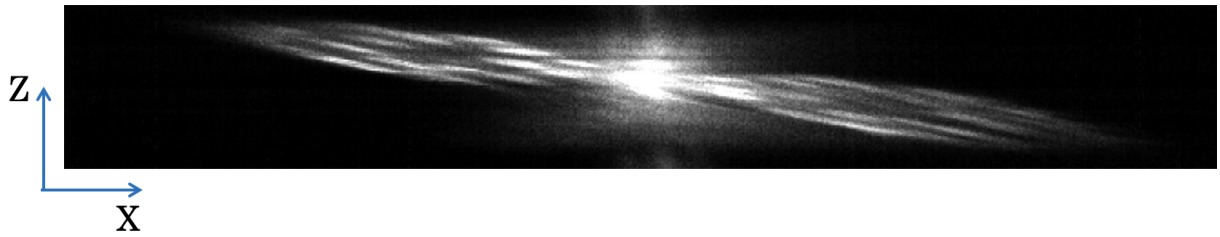

Figure 2.23: Data acquired during the initial testing of the microscope when using a reflective coverslip.

Figure 2.24 shows some of the reconstructed data after a few iterations. These results helped us validate that the forward model was correctly modeling the new geometry. However, the reconstructions with real data were taking even longer to run since they were larger image stacks used in simulation.

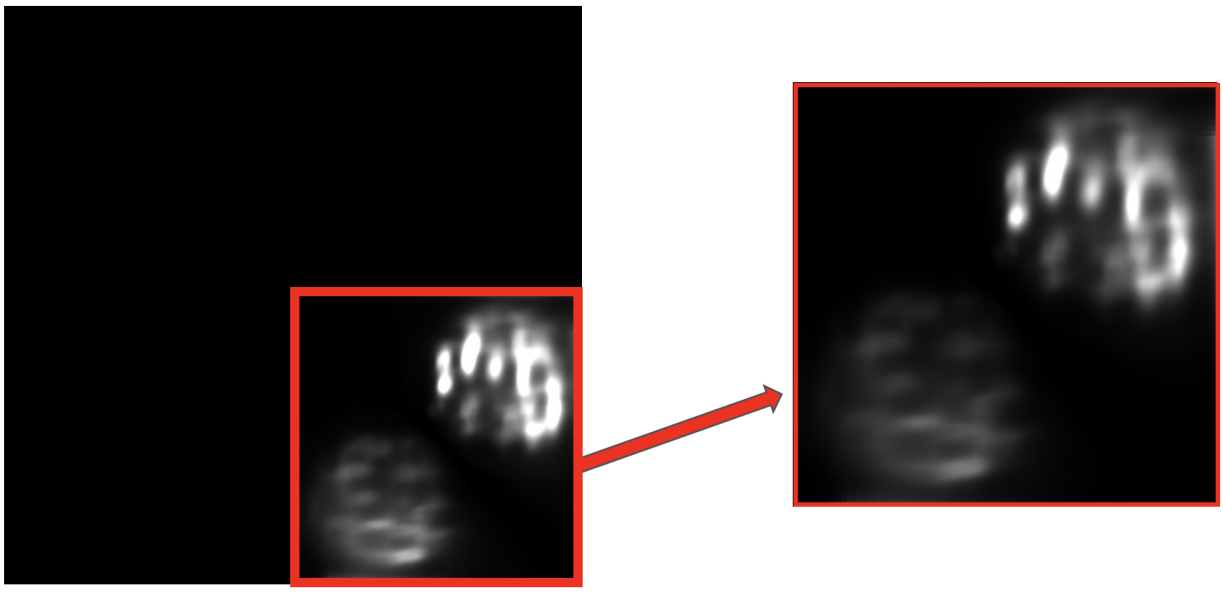

Figure 2.24: Initial reconstructed data after three iterations. We see that even after a few iterations, the contamination from the coverslip has been significantly reduced, if not eliminated entirely. In the image on the left, we also see one of the challenges with the stage scanning implementation. Because the sample is shifted across the field-of-view, we have to expand the volume to include all of these shifts. This requirement increases both the memory and computation burden during reconstruction.

With the computational resources we had access to, there was not much more we could do to improve the speed. The bottleneck in the reconstruction was having to transfer the

data between the CPU and GPU. The reason for doing this is that the GPUs we had access to did not have enough memory to store all of the data needed during reconstruction.

At this point, our collaborators were able to port our code to Matlab and run it on their own systems. Having GPUs with more memory allowed them to remove the transfer of data back and forth between the CPU and GPU. The were also able to replace a series of 2D convolutions with a 3D convolution where the 2D slice is zero-padded. These changes brought the total reconstruction time to under an hour for some of the datasets. Figure 2.25 shows some of the reconstruction using the final implementations of the forward model and reconstructions.

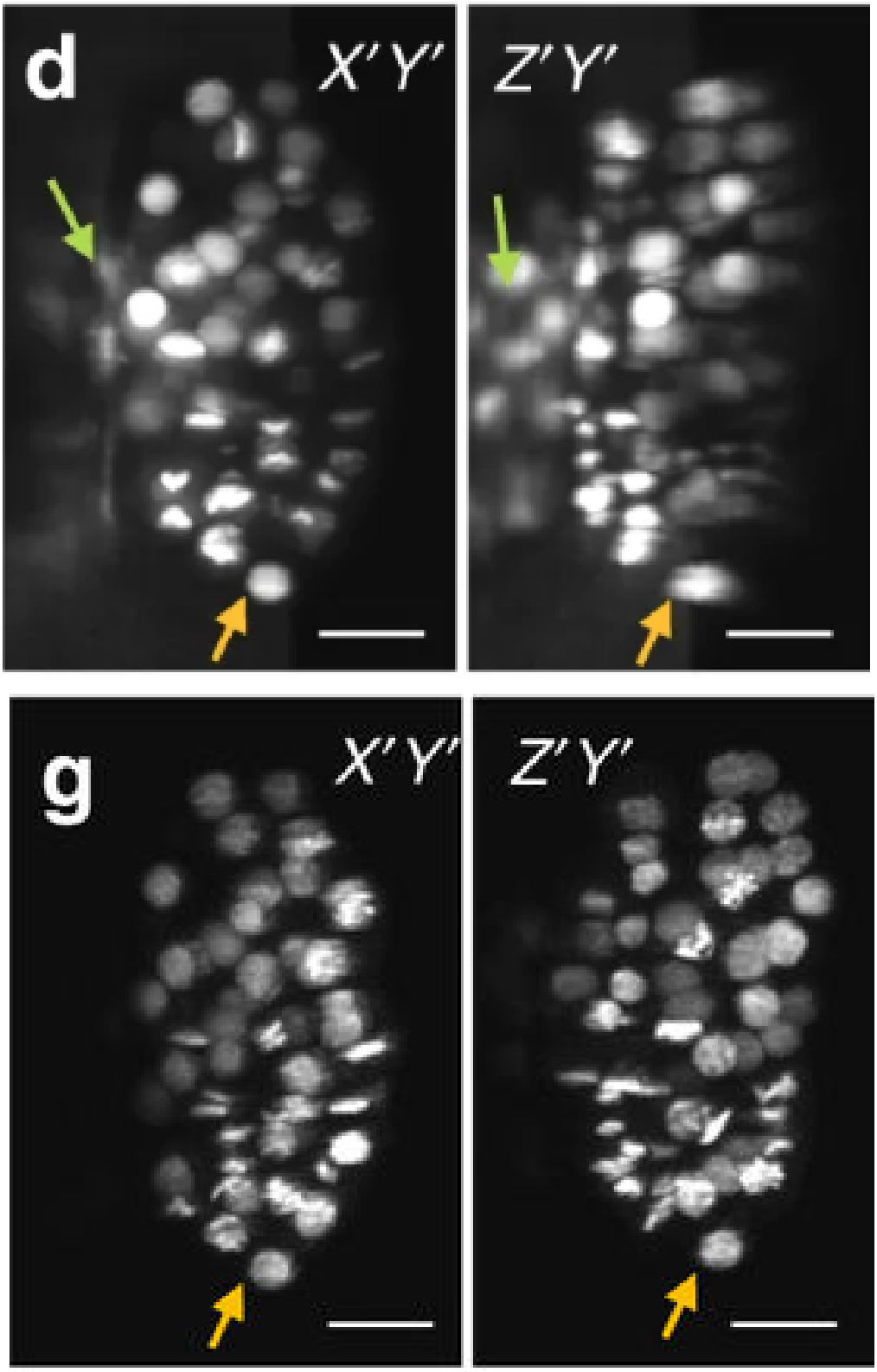

Figure 2.25: The image on the top, shows a 2D slice of data what was reconstructed using a naive light-sheet deconvolution that does not accurately account for the reflective coverslip. Continued on the next page.

Figure 2.25: Cont. In the image on the bottom, we see a 2D slice of data that is reconstructed with the final implementation of the modeling . Comparing the two, we can see that accurate modeling is needed to remove the contamination at the coverslip. We also see that the nuclei have a more isotropic resolution using the more complete model. Scale bars are 10 μm. Reprinted from Yicong Wu et al. (2017). Used with permission.

2.4.3 Conclusions

Using a reflective coverslip helps direct emitted light previously lost back up to the detection objectives creating reflected images. The mirror also allowed us to image with asymmetric geometry of a 0.71/1.1 NA objectives. Because of the mirrored views, this effectively gives us 2-1.1NA views of the sample which is not possible in a diSPIM geometry due to steric constraints. In this imaging configuration, we have improved the collection efficiency to around 60%. Also, because the excitation beam is reflected, there is no need to alternate excitation and detection, which speeds up acquisition time by a factor of two. One objective can both excite and detect the emission by using a filter to reject the lower wavelength excitation light.

CHAPTER 3

RESOLUTION LIMITS IN STRUCTURED ILLUMINATION MICROSCOPY

The next two chapters look at a different imaging technique called Structured Illumination microscopy (SIM). Chapter 3, focuses on our analysis of the theoretical bounds on the resolution in reconstructed SIM images. Most measures of resolution improvement use the cutoff frequency of an imaging system to determine resolution improvement. Instead of using the cutoff frequency, we calculate what the effective point spread function would be after image reconstruction and use its FWHM to measure resolution improvement. In Chapter 4, we use simulated data to test if different reconstruction methods can achieve these resolution bounds. In these chapters, the SIM that we refer to is known as Linear SIM. There are other classes of systems referred to nonlinear SIM that have resolutions closer to those found in super-resolution systems. A more thorough review on the differences can be found in [38].

3.1 Introduction

3.1.1 Structured Illumination Microscopy

SIM is a super-resolution imaging technique that was developed in the 1990's. Publications by Gustafsson *et al.* [18] and Heintzmann *et al.* [20] in 1999, both showed that using modulated illumination or interference, it was possible to achieve resolutions beyond the Abbe diffraction limit discovered by Ernst Abbe in 1873 [1]. In 2001, Gustafsson published an article titled, "Surpassing the lateral resolution limit by a factor of two using structured illumination microscopy" that brought together the theory, results, and implementation details to show that SIM improve lateral resolution by a factor of two [17].

SIM is one of the best super-resolution imaging techniques for live cell imaging as it requires no special dyes, only requires nine images per high-resolution image compared with

the tens of thousands of acquisitions needed for PALM [3] and STORM [30], and is capable of exciting 2D slices rather than point scanning the sample [21].

Using a modulated excitation allows the microscope to detect higher resolution components present in the object. These higher resolution components show up in the detected image as artifacts in the form of aliasing. Additional processing is required to decode the high-resolution components from the image and create an artifact-free high-resolution image.

3.1.2 Two-Photon Microscopy

Two-photon (2P) excitation relies on near simultaneous excitations by two long wavelength photons [16]. The use of 2P in microscopy has resulted in greater depth penetration due to reduced scattering of the excitation light and in an increase in spatial resolution due to the high photon flux needed to get two simultaneous absorptions [8].

3.2 Imaging Model

All structured illumination microscopes acquire multiple images of the sample that must be processed algorithmically in order to generate a artifact-free high-resolution image. For this process to work, there needs to be an accurate model of the imaging system. The model described in (1.5) is a very general equation for modeling an imaging system. For a SIM specific model, $\mathbf{H}$ needs to be explicitly calculated using the specifics of the SIM system being modeled.

3.2.1 Coherent Interference

In the continuous domain, when the modulated excitation is the result of coherent interference between two laser beams, the excitation intensity is modeled as

$$E_{1p}^{(j)}(\mathbf{r}, \mathbf{k}) = 1 + \alpha \cos(\mathbf{r} \cdot \mathbf{k} + \phi^{(j)}), \tag{3.1}$$

where $\mathbf{k}$ is the modulation frequency, $\phi^{(j)}$ is the relative phase of the pattern, and $\alpha \in [0,1]$ models the depth of the modulation depth. The detected intensity at the detector can be written as

$$\begin{aligned} g_{1p}^{(j)}(\mathbf{r},\mathbf{k}) &= \int \mathrm{d}\mathbf{r}' \ \left[E_{1p}^{(j)}(\mathbf{r}',\mathbf{k}) f(\mathbf{r}')\right] h_{em}(\mathbf{r}-\mathbf{r}') \\ &= [E_{1p}^{(j)}(\mathbf{r},\mathbf{k}) f(\mathbf{r})] * h_{em}(\mathbf{r}), \end{aligned} \tag{3.2}$$

where $f(\mathbf{r})$ is the fluorophore distribution being imaged and $h_{em}(\mathbf{r})$ is the PSF of the detection objective for emission photons.

The widefield image that resolution improvement is measured against is computed using

$$g_{\,\mathrm{wide}}(\mathbf{r}) = E_{\,\mathrm{wide}}\,[f(\mathbf{r}) * h_{em}(\mathbf{r})] \tag{3.3}$$

$$E_{\,\mathrm{wide}} = \sum_{j=0}^{J-1} E_{1p}^{(j)}(\mathbf{r},\mathbf{k}), \tag{3.4}$$

where (3.4) is a constant that is used to keep the excitation dose of the SIM and widefield simulations equal.

3.2.2 Point Scanning

Due to the high flux needed for 2P excitation, 2P-SIM systems rely on a point-scanning system to create the modulated excitation pattern rather than using coherent interference to create the modulation. In a 2P-SIM system, a diffraction limited spot is scanned across the sample while the intensity is modulated with position. The resulting 2P-SIM excitation pattern is computed by integrating over all scanner positions.

$$E_{2p}^{(j)}(\mathbf{r},\mathbf{k}) = \int \mathrm{d}\mathbf{r_s}\Big[(1+\alpha\,\cos(\mathbf{r_s}\cdot\mathbf{k}+\phi^{(j)}))\,h_{ex}(\mathbf{r}-\mathbf{r_s})\Big]^2 \tag{3.5}$$

Here, $h_{ex}(\mathbf{r})$ is the PSF of the objective for excitation photons and represents the shape of the spot being scanned across the sample.

The image acquired by the detector is written as

$$\begin{aligned} g_{2p}^{(j)}(\mathbf{r},\mathbf{k}) &= \int \mathrm{d}\mathbf{r}' \ \left[E_{2p}^{(j)}(\mathbf{r}',\mathbf{k}) f(\mathbf{r}')\right] h_{em}(\mathbf{r}-\mathbf{r}') \\ &= [E_{2p}^{(j)}(\mathbf{r},\mathbf{k}) f(\mathbf{r})] * h_{em}(\mathbf{r}). \end{aligned} \tag{3.6}$$

We can see that this form is identical to (3.2) just with a different form of excitation. We can rewrite (3.5) by simplifying the integral over scanning positions:

$$\begin{aligned} E_{2p}^{(j)}(\mathbf{r},\mathbf{k}) &= \int \mathrm{d}\mathbf{r_s} \left[(1+\alpha\, \cos(\mathbf{r_s}\cdot\mathbf{k}+\phi^{(j)}))\, h_{ex}(\mathbf{r}-\mathbf{r_s})\right]^2 \\ &= \int \mathrm{d}\mathbf{r_s}\ (1+\alpha\, \cos(\mathbf{r_s}\cdot\mathbf{k}+\phi^{(j)}))^2\, h_{ex}^2(\mathbf{r}-\mathbf{r_s}) \\ &= (1+\alpha\, \cos(\mathbf{r}\cdot\mathbf{k}+\phi^{(j)}))^2 * h_{ex}^2(\mathbf{r}) \\ &= \left(E_{1p}^{(j)}(\mathbf{r},\mathbf{k})\right)^2 * h_{ex}^2(\mathbf{r}). \end{aligned} \tag{3.7}$$

Plugging (3.7) into (3.6) we get that the image at the detector can be written as,

$$g_{2p}^{(j)}(\mathbf{r},\mathbf{k}) = \left(\left[(E_{1p}^{(j)}(\mathbf{r},\mathbf{k}))^2 * h_{ex}^2(\mathbf{r})\right] f(\mathbf{r})\right) * h_{em}(\mathbf{r}). \tag{3.8}$$

Comparing (3.2) and (3.8), we see that the forward models for one-photon and two-photon SIM are of the same form with the only difference being the effective excitation of the fluorophore distribution. We also simulate a scanning two-photon microscope without structured illumination so that we can measure the resolution improvement that we get from

using structured illumination.

$$g_{\text{2p-scan}}(\mathbf{r}) = E_{\text{2p-scan}}\left[f(\mathbf{r}) * h_{ex}^2(\mathbf{r})\right] \tag{3.9}$$

$$E_{\text{2p-scan}} = \sum_{j=0}^{J-1} E_{2p}^{(j)}(\mathbf{r}, \mathbf{k}) \tag{3.10}$$

3.3 Frequency Shifting Reconstruction

Reconstructions for SIM typically use three images that are acquired with relative phase differences of 0°, 120°, and 240°. Taking the Fourier transform of (3.2) for each of the three images allows the acquired data to be written as a 3×3 system of linear equations.

$$\begin{bmatrix} \overline{g}^{(0)}(\boldsymbol{\nu}) \\ \overline{g}^{(1)}(\boldsymbol{\nu}) \\ \overline{g}^{(2)}(\boldsymbol{\nu}) \end{bmatrix} = \frac{1}{2} \begin{bmatrix} 2 & \alpha & \alpha \\ 2 & \alpha\, e^{-i2\pi/3} & \alpha\, e^{i2\pi/3} \\ 2 & \alpha\, e^{-i4\pi/3} & \alpha\, e^{i4\pi/3} \end{bmatrix} \begin{bmatrix} \overline{f}(\boldsymbol{\nu}) \\ \overline{f}(\boldsymbol{\nu} - \mathbf{k}) \\ \overline{f}(\boldsymbol{\nu} + \mathbf{k}) \end{bmatrix} \tag{3.11}$$

where $\overline{\ }$ represents the Fourier transform. Details on how to calculate the Fourier transform of the detected image can be found in (3.4.1). Inverting the 3×3 matrix in (3.11) allows us to solve for the three frequency components and shift them back to their correct location in k-space. After shifting, the inverse Fourier transform is taken to recover the high-resolution image. Tikhonov filtering [35, 36] is incorporated to improve the SNR of the final high-resolution image. With Tikhonov filtering we use a constant, η, to control the strength of the filter. When η is close to zero, resolution is enhanced but the noise level is increased. As η is made larger, the noise in the images is reduced at the expense of poorer resolution.

3.4 Theoretical Resolution Limits for Structured Illumination Microscopy

In structured illumination microscopy (SIM), resolution is determined by the numerical aperture of the microscope's objective and the excitation and emission wavelengths. Resolution improvement can be approximated by comparing the cutoff frequency achievable with SIM and without SIM.

Without SIM, the cutoff frequency for widefield microscopes is computed using,

$$\nu_c^{wide} = \nu_{c,em} = \frac{2\text{NA}}{\lambda_{em}}. \tag{3.12}$$

The cutoff frequency for two-photon microscopes is computed using the same equation, but due to the fact that two-photon excitation squares the excitation PSF, the cutoff frequency for two-photon microscopes is twice the widefield excitation cutoff frequency.

$$\nu_c^{2p-scan} = 2\,\nu_{c,ex} = \frac{4\text{NA}}{\lambda_{ex}}. \tag{3.13}$$

Comparing the two cutoff frequencies, we see that the widefield cutoff frequency is dependent on the emission wavelength of the fluorescent dye while the two-photon cutoff frequency is only dependent on the wavelength used for excitation. This is caused by differences in how the emission photons are captured by the detector.

However, the cutoff frequency for both one-photon and two-photon SIM systems is determined by both the excitation and emission wavelengths. The excitation wavelength determines what the maximum frequency of the illumination pattern can be, and the emission wavelength determines the cutoff frequency on the detection side. These two contributions combine to create a cutoff frequency for SIM that is simply the sum of the emission cutoff

frequency and the frequency of the excitation pattern, ν.

$$\nu_c^{1p-sim} = \nu + \nu_{c,em} \tag{3.14}$$

$$\nu_c^{2p-sim} = \nu + \nu_{c,em} \tag{3.15}$$

As before, we introduce $\beta \in [0, 1]$ to rewrite the frequency of the excitation pattern in terms of the excitation cutoff frequency. When ($\beta = 1$), the maximum frequency allowed is used for the excitation pattern and when ($\beta = 0$), the excitation is constant across the FOV.

$$\nu_c^{1p-sim} = \beta \frac{2\text{NA}}{\lambda_{ex}} + \frac{2\text{NA}}{\lambda_{em}} \tag{3.16}$$

$$\nu_c^{2p-sim} = \beta \frac{4\text{NA}}{\lambda_{ex}} + \frac{2\text{NA}}{\lambda_{em}} \tag{3.17}$$

At this point we take the ratio of the cutoff frequency with SIM and without SIM to see how much improvement there is when using SIM. This ratio, Q_{sim}, can be used as a proxy to measure the resolution improvement that SIM provides.

$$Q_{sim}^{1p} = \frac{\beta\,(2\,\text{NA}/\lambda_{ex}) + (2\,\text{NA}/\lambda_{em})}{(2\,\text{NA}/\lambda_{em})} = 1 + \beta\,(\lambda_{em}/\lambda_{ex}) \tag{3.18}$$

$$Q_{sim}^{2p} = \frac{\beta\,(4\,\text{NA}/\lambda_{ex}) + (2\,\text{NA}/\lambda_{em})}{(4\,\text{NA}/\lambda_{ex})} = \lambda_{ex}/(2\,\lambda_{em}) + \beta \tag{3.19}$$

For one-photon SIM, the excitation and emission wavelengths are only slightly different due to the Stokes shift with the excitation wavelength being the smaller of the two. This means that when β is set to one, the improvement is slightly larger than two. For two-photon SIM, the excitation wavelength is generally smaller than twice the emission wavelength, and so when using the highest excitation frequency allowed, the improvement factor is slightly less than two. If we use this as a measure of resolution, we expect that for one-photon SIM, the minimum resolvable distance will be cut in half. For the two-photon SIM system, we

expect that the minimum distance resolvable will decrease, but it won't quite be a factor of two improvement.

3.4.1 Resolution Limits in SIM using Linear Reconstructions

Section 3.4 looks at the improvement factor when using SIM in terms of cutoff frequency and how much it is increased. This improvement factor is often used as a proxy for determining the resolution improvement gained with SIM. However, in practice, this improvement factor is not a reliable way to determine resolution improvement because, in 2P-SIM, the contrast of the shifted peaks decreases as the excitation frequency increases.

The decreased contrast is the result of using a diffraction-limited spot to produce the modulated excitation. Looking at the Fourier transform of the two-photon excitation pattern shows the shifted peaks get multiplied by the excitation OTF evaluated at the frequency of the modulated pattern. Since every imaging system introduces noise, as the excitation frequency increases, more of the higher frequency components fall below the noise level and results in decreased resolution in the final reconstructed image.

For a better measure of resolution, we use 1D simulations to compute the effective OTF in both one-photon and two-photon SIM after performing the linear reconstruction described in Section 3.3. We then compute the effective PSF by taking the inverse Fourier transform of the effective OTFs. We use the FWHM of this effective PSF as our measure of resolution to determine the resolution improvement that SIM can provide.

One-Photon OTF

To compute the effective OTF, we start by taking the Fourier transform of the forward model in (3.2) with respect to $\boldsymbol{r}$, obtaining

$$\overline{g}_{1p}^{(j)}(\boldsymbol{\omega}, \mathbf{k}) = O_{em}(\boldsymbol{\omega}) \left[\overline{E}_{1p}^{(j)}(\boldsymbol{\omega}, \mathbf{k}) * \overline{f}(\boldsymbol{\omega}) \right] \tag{3.20}$$

Here we denote the Fourier transform using $\bar{}$. The next step is to expand out the Fourier transform of the excitation pattern.

$$\overline{E}_{1p}^{(j)}(\boldsymbol{\omega}, \mathbf{k}) = \int_{-\infty}^{\infty} \mathrm{d}\mathbf{r} \left[1 + \alpha \cos(\mathbf{r} \cdot \mathbf{k} + \phi^{(j)})\right] e^{-i2\pi \mathbf{r} \cdot \boldsymbol{\omega}} \tag{3.21}$$

$$= \delta(\boldsymbol{\omega}) + \pi\alpha \left(e^{-i\phi^{(j)}} \delta(\mathbf{k} + 2\pi\boldsymbol{\omega}) + e^{i\phi^{(j)}} \delta(\mathbf{k} - 2\pi\boldsymbol{\omega})\right) \tag{3.22}$$

$$= \delta(\boldsymbol{\omega}) + \frac{\alpha}{2} \left(e^{-i\phi^{(j)}} \delta\left(\boldsymbol{\omega} + \frac{\mathbf{k}}{2\pi}\right) + e^{i\phi^{(j)}} \delta\left(\boldsymbol{\omega} - \frac{\mathbf{k}}{2\pi}\right)\right). \tag{3.23}$$

Plugging (3.23) into (3.20) we get

$$\overline{g}_{1p}^{(j)}(\boldsymbol{\omega}, \mathbf{k}) = O_{em}(\boldsymbol{\omega}) \left[\overline{f}(\boldsymbol{\omega}) + \frac{\alpha}{2} e^{\pm i\phi^{(j)}} \overline{f}\left(\boldsymbol{\omega} \mp \frac{\mathbf{k}}{2\pi}\right)\right]. \tag{3.24}$$

At this point we can change the excitation vector from angular frequency to linear frequency such that $\mathbf{k} = 2\pi\boldsymbol{\nu}$.

$$\overline{g}_{1p}^{(j)}(\boldsymbol{\omega}, \boldsymbol{\nu}) = O_{em}(\boldsymbol{\omega}) \left[\overline{f}(\boldsymbol{\omega}) + \frac{\alpha}{2} e^{\pm i\phi^{(j)}} \overline{f}\left(\boldsymbol{\omega} \mp \boldsymbol{\nu}\right)\right] \tag{3.25}$$

Two-Photon OTF

We start by taking the Fourier transform of the forward model in (3.6) just as we did for one-photon.

$$\bar{g}_{2p}^{(j)}(\boldsymbol{\omega}, \mathbf{k}) = O_{em}(\boldsymbol{\omega}) \left(\left[O_{ex}^{2p}(\boldsymbol{\omega}) \overline{\left(E_{1p}^{(j)}(\boldsymbol{\omega}, \mathbf{k}) E_{1p}^{(j)}(\boldsymbol{\omega}, \mathbf{k})\right)}\right] * \overline{f}(\boldsymbol{\omega})\right) \tag{3.26}$$

Next, we compute the Fourier transform of the squared one-photon excitation pattern.

$$\overline{\left(E_{1p}^{(j)}(\boldsymbol{\omega},\mathbf{k})E_{1p}^{(j)}(\boldsymbol{\omega},\mathbf{k})\right)} = \int_{-\infty}^{\infty} \mathrm{d}\mathbf{r}\ \left[1+\alpha\cos(\mathbf{r}\cdot\mathbf{k}\ +\ \phi^{(j)})\right]^2\ e^{-i2\pi\mathbf{r}\cdot\boldsymbol{\omega}} \tag{3.27}$$

$$= \frac{1}{4}\Bigg[2\left(\alpha^2+2\right)\delta(\boldsymbol{\omega}) + \pi\alpha\, e^{-i2\phi^{(j)}}\big[\alpha\, e^{i4\phi^{(j)}}\,\delta(\mathbf{k}-\pi\boldsymbol{\omega}) + \alpha\,\delta(\mathbf{k}+\pi\boldsymbol{\omega}) + 8e^{3i\phi^{(j)}}\,\delta(\mathbf{k}-2\pi\boldsymbol{\omega})\ + 8e^{\,i\phi^{(j)}}\,\delta(\mathbf{k}+2\pi\boldsymbol{\omega})\big]\Bigg] \tag{3.28}$$

$$= \frac{(\alpha^2+2)}{2}\,\delta(\boldsymbol{\omega}) + \frac{\alpha^2}{4}\left[e^{\,i2\phi^{(j)}}\,\delta\left(2\frac{\mathbf{k}}{2\pi}-\boldsymbol{\omega}\right)\ +\ e^{\,-i2\phi^{(j)}}\,\delta\left(2\frac{\mathbf{k}}{2\pi}+\boldsymbol{\omega}\right)\right] + \alpha\left[e^{\,i\phi^{(j)}}\,\delta\left(\frac{\mathbf{k}}{2\pi}-\boldsymbol{\omega}\right)\ +\ e^{\,-i\phi^{(j)}}\,\delta\left(\frac{\mathbf{k}}{2\pi}+\boldsymbol{\omega}\right)\right] \tag{3.29}$$

Now we plug this back into (3.33).

$$\bar{g}_{2p}^{(j)}(\boldsymbol{\omega},\mathbf{k}) \tag{3.30}$$

$$= O_{em}(\boldsymbol{\omega})\Bigg[\frac{(\alpha^2+2)}{2}\,O_{ex}^{2p}(0)\,\bar{f}(\boldsymbol{\omega}) + \alpha\sum_{m\in\{-1,1\}} e^{\,im\phi^{(j)}}\,O_{ex}^{2p}\left(\frac{\mathbf{k}}{2\pi}\right)\bar{f}\left(\frac{\mathbf{k}}{2\pi}-m\boldsymbol{\omega}\right) + \frac{\alpha^2}{4}\sum_{m\in\{-1,1\}} e^{\,i2m\phi^{(j)}}\,O_{ex}^{2p}\left(2\frac{\mathbf{k}}{2\pi}\right)\,\bar{f}\left(\boldsymbol{\omega}-m\,2\frac{\mathbf{k}}{2\pi}\right)\Bigg] \tag{3.31}$$

Again the last step we do is to change the excitation vector from angular frequency to linear frequency such that $\mathbf{k} = 2\pi\boldsymbol{\nu}$.

$$\bar{g}_{2p}^{(j)}(\boldsymbol{\omega}, \boldsymbol{\nu}) \tag{3.32}$$

$$= O_{em}(\boldsymbol{\omega}) \Bigg[\frac{(\alpha^2 + 2)}{2} O_{ex}^{2p}(0)\, \bar{f}(\boldsymbol{\omega}) + \alpha\, e^{\pm i\phi^{(j)}} O_{ex}^{2p}(\boldsymbol{\nu})\, \bar{f}(\boldsymbol{\omega} \mp \boldsymbol{\nu}) + \frac{\alpha^2}{4} e^{\pm i2\phi^{(j)}} O_{ex}^{2p}(2\boldsymbol{\nu})\, \bar{f}(\boldsymbol{\omega} \mp 2\boldsymbol{\nu}) \Bigg] \tag{3.33}$$

Calculating the PSFs

To calculate the PSFs, we begin with plotting the OTFs in (3.24) and (3.33) when our object is a point source (delta function). In Figure 3.1 we are showing the OTFs for both one-photon and two-photon SIM after we have performed the linear reconstruction by shifting the frequencies to where they should be. In this figure, we use the following parameters: an α of one, a NA of 0.95 on both detection and excitation objectives, an excitation wave length of 488 nm, an emission wavelength of 510 nm, and a β set to 0.6 so that the excitation frequency is 60% of the excitation objectives cutoff frequency.

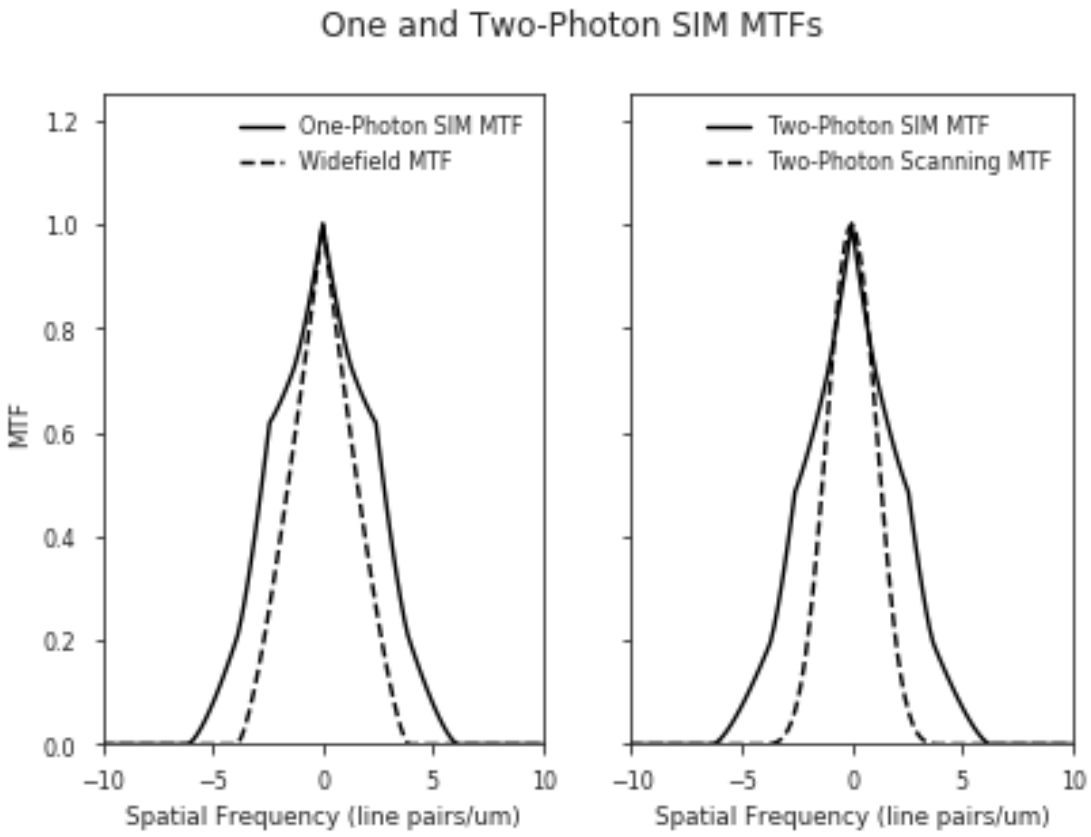

Figure 3.1: Reconstructed MTFs for both 1P (left) and 2P (right) SIM. These are plotted against the MTFs for the baseline configurations we compare SIM to. The piecewise behavior in both of the reconstructed MTFs is the result of the detection objectives and occurs at the crossover point when the detection MTF is less than the MTF of the excitation and sample.

After computing these MTFs we can take the inverse Fourier transfer to get the reconstructed PSFs. In Figure 3.2 we are plotting the corresponding PSFs for the MTFs in Figure 3.1.

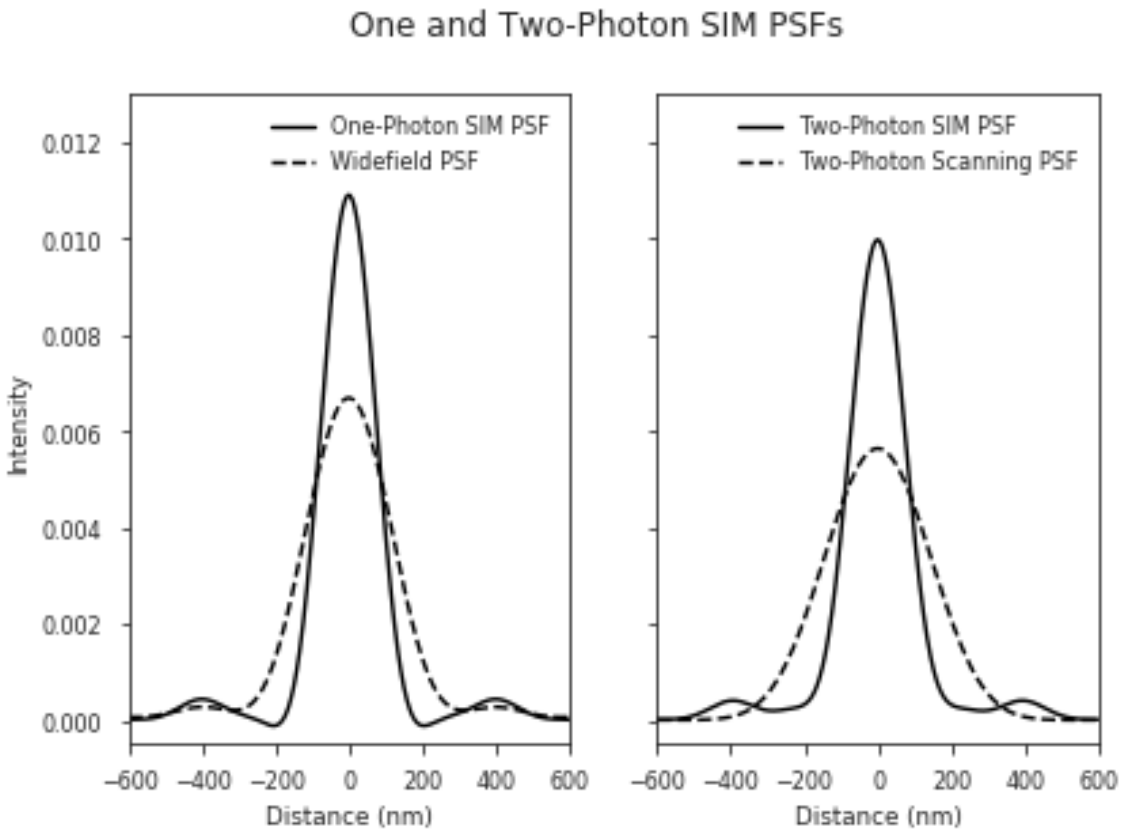

Figure 3.2: Reconstructed PSFs for both 1P (left) and 2P (right) SIM. These are plotted against the PSFs for the baseline configurations we compare SIM to.

Using the reconstructed PSFs, we can measure the FWHM to measure the resolution of SIM after linear reconstruction. In Figure 3.3 we have plotted the FWHM as a function of β. In the figure we see that as the excitation frequency increases, the FWHM decreases which is what we expect based on the calculations in section 3.4. However, here we see that for 2P-SIM, the resolution plateaus around 60% of the maximum frequency and then starts to increase. This is not something that was predicted by just computing the cutoff frequency for SIM. The reason of this plateau is that in 2P-SIM, the shifted frequency lobes are multiplied by the 2P excitation OTF. This means that the contrast of the shifted, higher frequencies is reduced as the excitation frequency increases.

Figure 3.3: Computed FWHM of reconstructed PSFs for both 1P (left) and 2P (right) SIM plotted against the excitation frequency. Both the 1P and 2P curves are calculated using a 0.95 NA objective, and an emission wavelength of 510 nm. The 1P curve uses an excitation wavelength of 488 nm, and the 2P curve uses an excitation wavelength of 900 nm.

3.4.2 Theoretical Resolution Limits of Deconvolution

In the last section we looked as resolution improvements after linear reconstructions. In this section we will look at the resolution improvement that we expect from using our iterative reconstructions.

Deconvolved OTF and PSF

To begin, we start with laying out what the goal of a perfect reconstruction look entails. The goal of deconvolution is to recover the higher frequency components that have been reduced by the system OTF. In a perfect reconstruction, all frequencies in the passband

of the microscope would be recovered such that the reconstructed OTF would be a rect function, for a 1D imaging system. Figure 3.4 is a plot of what the OTF would look like for a widefield microscope before and after a perfect reconstruction.

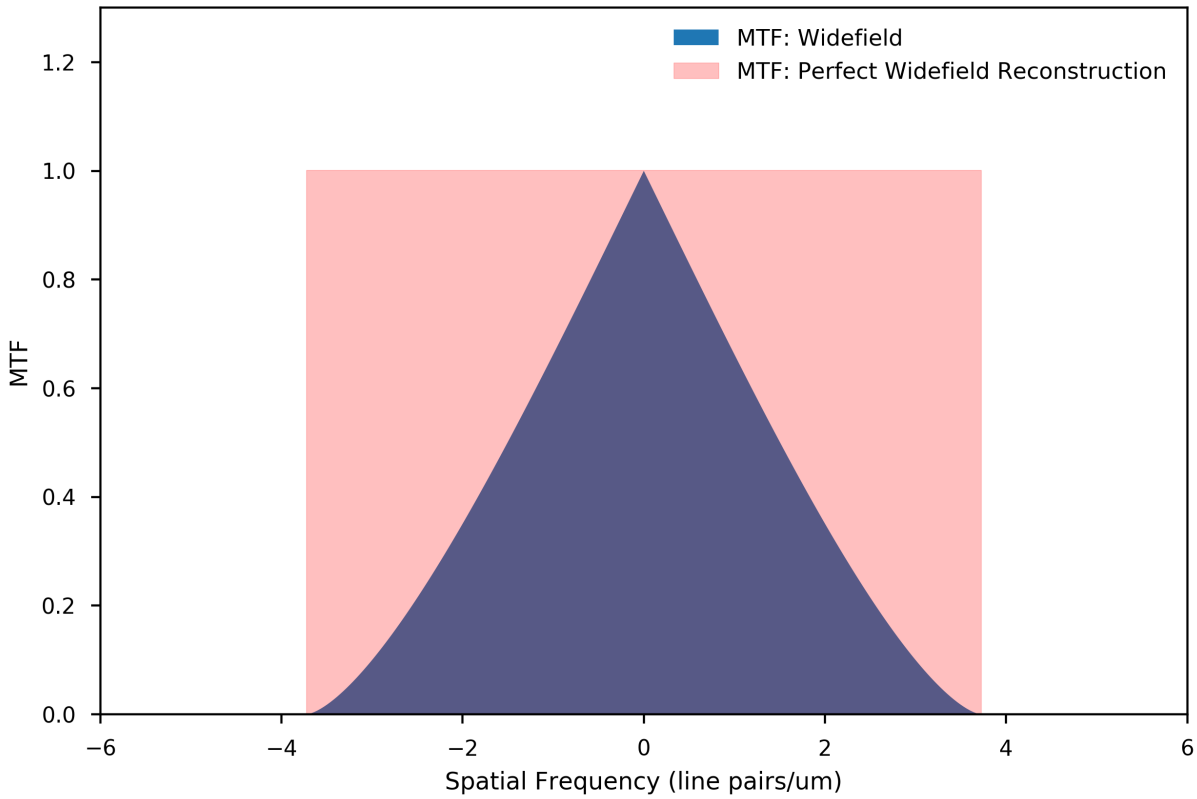

Figure 3.4: In the spatial frequency domain, a perfect reconstruction would pass unmodulated all of the frequencies below the cutoff frequency. This can be represented as a rect function.

To measure the resolution of this perfect reconstruction, we can take the inverse Fourier transform and measure resolution based on the resulting PSF. For a cutoff frequency of ν_c,

the inverse Fourier transform is calculated using

$$\mathrm{PSF}(x) = \int_{\infty}^{\infty} \mathrm{d}\nu \ \mathrm{OTF}(\nu) e^{i2\pi\nu x} \tag{3.34}$$

$$= \int_{-\nu_c}^{\nu_c} \mathrm{d}\nu \ e^{i2\pi\nu x} \tag{3.35}$$

$$= \frac{1}{i2\pi x} e^{i2\pi\nu x}\Big|_{-\nu_c}^{\nu_c} \tag{3.36}$$

$$= \frac{1}{\pi x} \frac{[e^{i2\pi\nu_c x} - e^{-i2\pi\nu_c x}]}{2i} \tag{3.37}$$

$$= 2\nu_c \frac{\sin(2\pi\nu_c x)}{2\nu_c \pi x} \tag{3.38}$$

$$= 2\nu_c \,\mathrm{sinc}(2\nu_c x). \tag{3.39}$$

In the final form of the PSF (3.39), we use the normalized version of the sinc function. In Figure 3.5 we plot the PSF for widefield without deconvolution against the PSF that results from a perfect deconvolution.

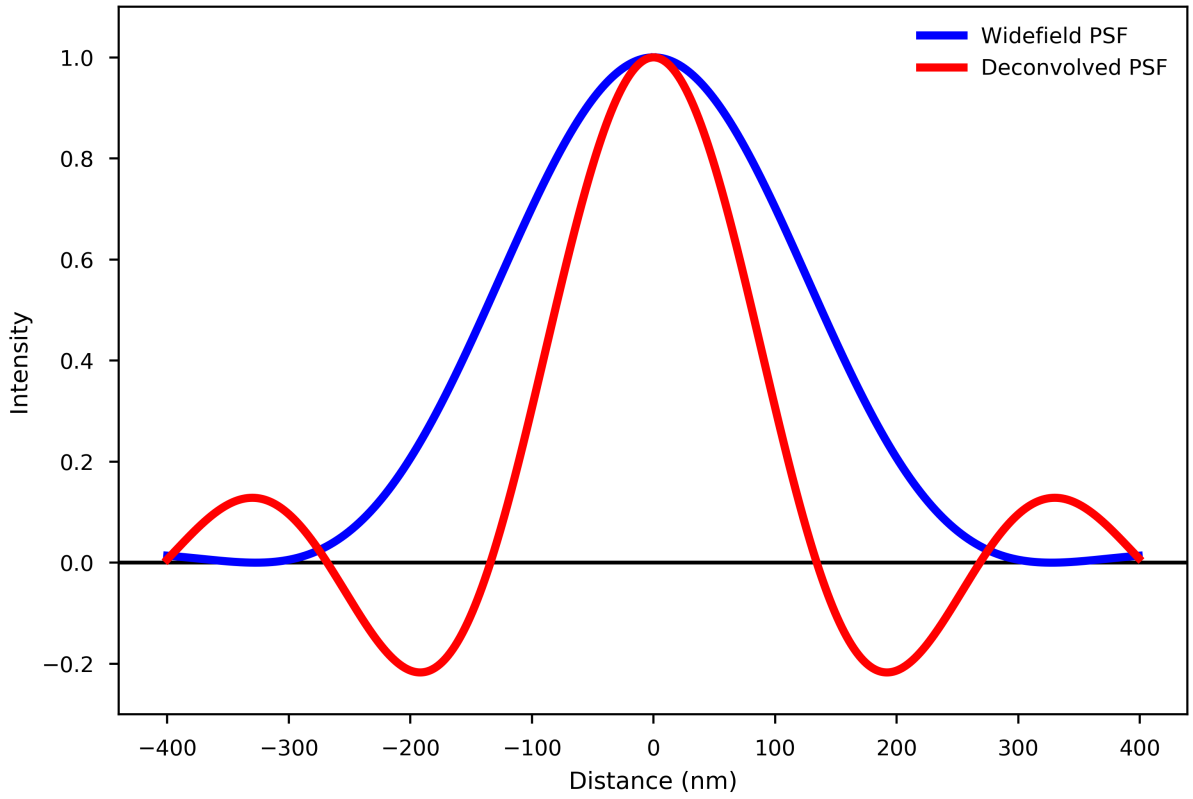

Figure 3.5: Comparing the PSF before and after a perfect reconstruction in a noiseless diffraction limited system.

3.4.3 Measuring Resolution

There are multiple ways that we can measure the resolution from the system PSF. A common way to calculate resolution is to measure the FWHM of the PSF, and use that as the system resolution. From the reconstruction PSF we can calculate the half maximum by solving the following equation for $\times$. The FWHM is then twice the half maximum.

$$\operatorname{sinc}\left(2\,\nu_c\,x\right) = \frac{1}{2}. \tag{3.40}$$

Another way to measure resolution is to use the Rayleigh Criteria. Using this method involves finding the distance between two point sources such that the contrast between the two peaks is 26%. Figure 3.6 shows the Rayleigh distance both before and after the perfect

reconstruction.

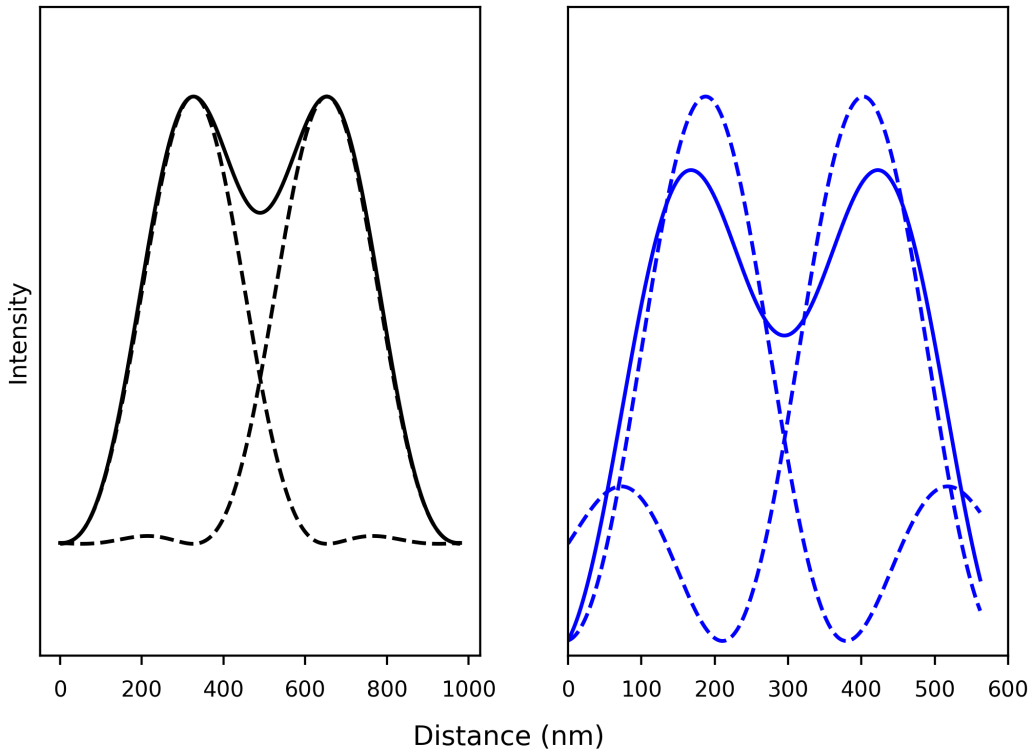

Figure 3.6: Comparing the Rayleigh distances before and after a perfect reconstruction in a noiseless diffraction limited imaging system. The plot on the (left) shows the minimum resolvable distance between two point sources prior to reconstruction, and the image on the (right) shows the minimum resolvable distance after reconstruction.

3.4.4 Results

Using these two different methods for computing the resolution from a PSF, we can calculate what that resolution is for different excitation frequencies in SIM, and compare it to a scanning two-photon microscope. For this comparison, we used the same parameters from section 4.3. Table 3.1 shows the best resolutions an iterative reconstruction can achieve for the 2P scanning microscope configuration. We see that the FWHM measure of resolution is 15% smaller than the resolution computed using the Rayleigh Criteria. This shows that measuring the resolution on a single point source can give a false sense of performance as it

will be unable to differentiate non-point sources at that distance.

Table 3.1: A table showing the best resolution after deconvolution for a scanning two-photon microscope.

	lp/um	min two-point resolution (nm)	min FWHM (nm)
scanning two-photon	4.22	165.42	142.90

In Tables 3.3 and 3.2, we compute the best achievable resolutions for reconstructions for 1P and 2P SIM for both measures of resolution. These are the computed values that we use in Figs. 4.7 and 4.8.

Table 3.2: A table showing the best resolution after deconvolution for a two-photon SIM.

Frequency (%)	lp/um	min two-point resolution (nm)	min FWHM (nm)
100	7.95	87.88	75.92
95	7.74	90.28	77.99
90	7.53	92.81	80.17
85	7.31	95.49	82.49
80	7.10	98.33	84.94
75	6.89	101.34	87.54
70	6.68	104.54	90.31
65	6.47	107.95	93.26
60	6.26	111.59	96.40
55	6.05	115.49	99.77
50	5.84	119.67	103.37
45	5.63	124.16	107.25
40	5.41	129.00	111.44
35	5.20	134.23	115.96
30	4.99	139.91	120.86
25	4.78	146.09	126.20
20	4.57	152.84	132.03
15	4.36	160.24	138.42
10	4.15	168.39	145.47
5	3.94	177.42	153.27

Table 3.3: A table showing the best resolution after deconvolution for a one-photon SIM.

Frequency (%)	lp/um	min two-point resolution (nm)	min FWHM (nm)
100	7.62	91.67	79.19
95	7.42	94.08	81.27
90	7.23	96.61	83.46
85	7.03	99.28	85.77
80	6.84	102.11	88.21
75	6.65	105.10	90.79
70	6.45	108.27	93.53
65	6.26	111.64	96.44
60	6.06	115.23	99.54
55	5.87	119.05	102.84
50	5.67	123.14	106.37
45	5.48	127.51	110.15
40	5.28	132.21	114.21
35	5.09	137.27	118.58
30	4.89	142.73	123.30
25	4.70	148.64	128.40
20	4.50	155.07	133.95
15	4.31	162.07	140.01
10	4.11	169.74	146.63
5	3.92	178.17	153.91
0	3.73	187.48	161.95

CHAPTER 4

RECONSTRUCTION IN STRUCTURED ILLUMINATION MICROSCOPY

In Chapter 3 we calculated the theoretical bounds on the resolution for structured illumination microscopy. In this chapter, we begin by discretizing the imaging models for SIM so they can be used for simulating images acquired on SIM systems. Using the discretized imaging models, We then implement multiple reconstruction methods and compare the resolution in the reconstructed data to the theoretical bounds we found in Chapter 3.

The reconstruction methods we develop aim to simplify and correct previous implementations of iterative reconstruction methods in SIM. Simplification is achieved by removing the need for hyperparameter estimation. Orieux *et al.* [26], have developed a Bayesian-based reconstruction method for SIM. Their work uses a Bayesian framework that requires the estimation of two hyperparameters using iterative sampling of the image conditional posterior law. Sampling is performed using a Markov chain Monte Carlo (MCMC) algorithm called the Gibbs algorithm [23, 14]. In addition to the need for parameter estimation, they found that their reconstruction method is very sensitive to the parameters used to model the excitation modulation in the forward model.

In this chapter we implement two different iterative reconstruction schemes: Richardson-Lucy (RL) deconvolution [29, 25] and ℓ_2-constrained, total-variation (TV) minimization using methods developed by Chambolle and Pock (CP) [5]. Each method only has a single parameter that could be tuned to change the image quality in the reconstructed image, making them easier to implement. While there is a previous paper that claims to use TV reconstructions for SIM data, they have mistakes in how they derive the update equations for non-shift invariant data like SIM.

4.1 Discrete Imaging Model

As the acquired data is discrete, the previous imaging models require translation from the continuous domain to the discrete domain. Discretization begins with the transformation of each acquired image into a one-dimensional vector $\boldsymbol{g}^{(j)}$ of length N, by concatenating the pixels in lexicographical order. Convolution with the system point spread function is replaced by matrix multiplication with a system matrix $\mathbf{A}^{(j)}$. To preserve point-wise multiplication, the effective excitation is replaced with a diagonal matrix $\mathbf{E}^{(j)}$. Lastly, an additive noise vector $\boldsymbol{n}^{(j)}$ can be included to represent noise introduced during the imaging process.

$$g^{(j)}(\mathbf{r}) = \left[E^{(j)}(\mathbf{r},\mathbf{k})f(\mathbf{r})\right] * h_{em}(\mathbf{r}) \longrightarrow \boldsymbol{g}^{(j)} = \mathbf{A}^{(j)}\mathbf{E}^{(j)}\boldsymbol{f} + \boldsymbol{n}^{(j)} \tag{4.1}$$

Combining all J equations is simplified using the notion of a repeating matrix found in Orieux *et al.* [26]. A repeating matrix $\mathbf{R}$, is a $JN \times N$ matrix formed by concatenating J - $N \times N$ identity matrices. Multiplication with the repeating matrix creates J copies of the matrix. The last step is replacing the other matrices in (4.1) with $JN \times JN$ block-diagonal matrices and replacing the length N vectors with concatenated vectors of length JN.

$$\boldsymbol{g} = \mathbf{AER}\boldsymbol{f} + \boldsymbol{n} = \mathbf{H}\boldsymbol{f} + \boldsymbol{n} \tag{4.2}$$

$$\text{where} \qquad \mathbf{H} = \mathbf{AER} \tag{4.3}$$

The block-diagonal matrix $\mathbf{A}$ is formed with $\mathbf{A}^{(j)}$ blocks, $\mathbf{E}$ is the block-diagonal matrix formed with $\mathbf{E}^{(j)}$ blocks, $\boldsymbol{g}$ is a length JN vector formed by concatenating the J - $\boldsymbol{g}^{(j)}$ vectors, and $\boldsymbol{n}$ is a length JN vector formed by concatenating the J - $\boldsymbol{n}^{(j)}$ vectors.

4.2 Iterative Reconstructions

The previous reconstruction method requires the use of shifting, scaling, interpolation, and filtering during different steps of the reconstruction process. These steps have the potential to

introduce artifacts in the high-resolution image. In an iterative reconstruction, the algorithm is responsible for placing folded-over frequencies in the correct location, thus eliminating possible sources of error introduced during reconstruction.

4.2.1 RL/MLEM

Richardson-Lucy (RL) deconvolution is a statistical reconstruction method widely used in fluorescence microscopy. In medical imaging, this statistical reconstruction method is often referred to as maximum-likelihood expectation-maximization (MLEM) [32]. The iterative update we use is a generalization of (1.11) used by Richardson and Lucy [29, 25].

Plugging (4.3) into (1.11) gives

$$\begin{aligned}
\boldsymbol{f}^{t+1} &= \frac{\boldsymbol{f}^{j}}{\mathbf{S}}\left[(\mathbf{AER})^{\mathrm{T}}\frac{\boldsymbol{g}}{\mathbf{AER}\boldsymbol{f}^{t}}\right] \\
&= \frac{\boldsymbol{f}^{t}}{\mathbf{S}}\left[\mathbf{R}^{\mathrm{T}}\mathbf{E}^{\mathrm{T}}\mathbf{A}^{\mathrm{T}}\frac{\boldsymbol{g}}{\mathbf{AER}\boldsymbol{f}^{t}}\right] \\
\boldsymbol{f}^{t+1} &= \frac{\boldsymbol{f}^{t}}{\mathbf{S}}\left[\sum_{j=1}^{J}(\mathbf{E}^{(j)})(\mathbf{A}^{(j)})^{\mathrm{T}}\frac{\boldsymbol{g}^{(j)}}{\mathbf{A}^{(j)}\mathbf{E}^{(j)}\boldsymbol{f}^{t}}\right]
\end{aligned} \tag{4.4}$$

where j is the SIM image index and $\mathbf{S}$ is the sensitivity matrix that was introduced in (1.11). For multi-view systems, this calculation can be reduced to

$$\mathbf{S} = \sum_{j=1}^{J}(\mathbf{E}^{(j)})(\mathbf{A}^{(j)})^{\mathrm{T}}\mathbb{1} \tag{4.5}$$

If the system matrices or PSFs are normalized, (4.5) can be further reduced to the sum of the excitation matrices.

$$\mathbf{S} = \sum_{j=1}^{J}\mathbf{E}^{(j)} \tag{4.6}$$

Translating this discrete update equation back to the continuous domain brings back the

convolutions present in the continuous forward models

$$f^{t+1}(\mathbf{r}) = \frac{f^t(\mathbf{r})}{S(\mathbf{r})}\left[\sum_{j=1}^{J} E^{(j)}(\mathbf{r})\left(h_{em}^{\dagger(j)}(\mathbf{r}) * \left(\frac{g^{(j)}(\mathbf{r})}{h_{em}^{(j)}(\mathbf{r}) * E^{(j)}(\mathbf{r}) f^t(\mathbf{r})}\right)\right)\right], \tag{4.7}$$

where † denotes the Hermitian adjoint of a function. Writing the update as a convolution allows us to exploit the convolution-multiplication theorem and perform the convolutions in the spatial frequency domain. This greatly improves both memory usage and computation speed in the implemented reconstruction.

A well-known issue with using RL is that the noise level in the reconstruction increases as the number of iterations increases. To get around this issue the algorithm should be stopped early as a type of regularization. The next section uses a cost function that employs explicit constraints to help remove some of the ambiguities associated with early stopping.

4.2.2 Total-Variation Minimization

Total-variation (TV) is a regularized reconstruction method that eliminates the need for early stopping by penalizing the TV-norm in the cost function. The TV-norm or ℓ_1 norm of the image gradient is smaller in regions of constant intensities. Thus minimizing the TV-norm promotes regions of uniform intensity with sharp cutoffs between different objects.

The TV method implemented in this section is the solution to a ℓ_2-constrained, total-variation minimization problem. In the constrained form, the TV-norm is the lone term in the cost function, but a valid solution also has to satisfy a separate data fidelity and positivity constraint. The data fidelity constraint requires that the ℓ_2-norm of the difference between the detected images and the forward model applied to the reconstructed images be smaller than some constant ϵ. The positivity constraint requires all pixels in the reconstructed image to be non-negative.

$$\hat{\boldsymbol{f}} = \arg\min_{\boldsymbol{f}} \; \| \left(|\nabla \boldsymbol{f}|\right) \|_1 \quad \text{s.t.} \quad \left|\left|\mathbf{H}\boldsymbol{f} - \boldsymbol{g}\right|\right|_2 \leq \epsilon, \; \boldsymbol{f}_i \geq 0 \; \forall \, i \tag{4.8}$$

This constrained optimization problem can be rewritten as an unconstrained optimization in the form of (1.8) through the use of indicator functions. In this form the cost function to minimize is given by

$$\Phi(\boldsymbol{f},\boldsymbol{g}) = \left\{ \parallel (|\nabla \boldsymbol{f}|) \parallel_1 + \delta_p(\boldsymbol{f}) + \ \delta_{\text{ball}(\epsilon)}(\mathbf{H}\boldsymbol{f} - \boldsymbol{g}) \right\}, \tag{4.9}$$

where ϵ is the data constraint parameter and δ_p and $\delta_{\text{ball}(\epsilon)}$ are indicator functions used to enforce the positivity and ℓ_2 constraints.

$$\delta_p(\boldsymbol{f}) \equiv \begin{cases} 0 & \boldsymbol{f}_i \ \geq 0 \ \ \forall \ i \\ \infty & \text{otherwise} \end{cases} \qquad \delta_{\text{ball}(\epsilon)}(\boldsymbol{f}) \equiv \begin{cases} 0 & \left|\left|\boldsymbol{f}\right|\right|_2 \ \leq \ \epsilon \\ \infty & \left|\left|\boldsymbol{f}\right|\right|_2 \ > \ \epsilon \end{cases}. \tag{4.10}$$

In this new form, (4.9) is a convex function and opens the doors to the many methods for solving convex optimization problems. For this work we chose to use the primal-dual formulation for convex objective functions first introduced by Chambolle and Pock [5] with applications to imaging. In the primal-dual formulation, a second objective function, the dual, is maximized. When convergence is reached, the primal and the dual should be equal. Thus, this difference called the primal-dual gap gives a well defined criteria for convergence. Convergence is reached when the primal-dual gap is within some tolerance of zero. Implementation of the update equations for this reconstruction method follow the framework developed by Sidky *et al.* [33]. The psuedo-code for this implementation can be found in Section A.1.

4.3 Simulations

In these simulations we only consider the 2D case where the modulated excitation intensity is only along the plane perpendicular to the optical axis. Using the imaging models derived in Section 3.2, simulated SIM images were generated for use in both the qualitative and

quantitative evaluation of achievable resolutions after reconstruction. The two phantoms shown in Figure 4.1 were used to generate SIM data used for quantitative evaluation. The first, a bar pattern phantom, is used to determine what frequencies are resolvable after reconstruction, and the second, a phantom with point sources and uniform regions, is used for visual assessment.

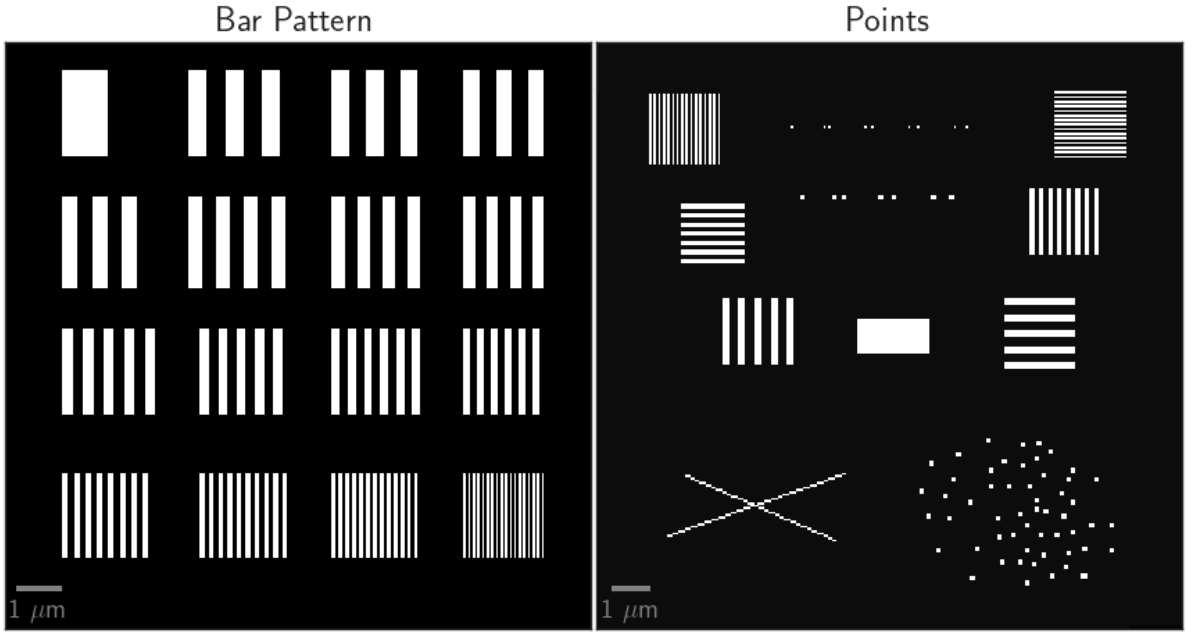

Figure 4.1: Phantoms used to simulate SIM data for the qualitative assessment of image quality after image reconstruction.

To quantitatively measure the resolution of reconstructed images while also accounting for the non-linear effects of the iterative reconstructions, we use a method proposed by Gong *et al.* for measuring point source resolution. They found that by reconstructing a low-contrast point source on a uniform background, and reconstructing the uniform background without a point source, they could achieve more stable FWHM measurements that did not simply approach the pixel size of the reconstructed images [15]. The two phantoms are shown in Figure 4.2.

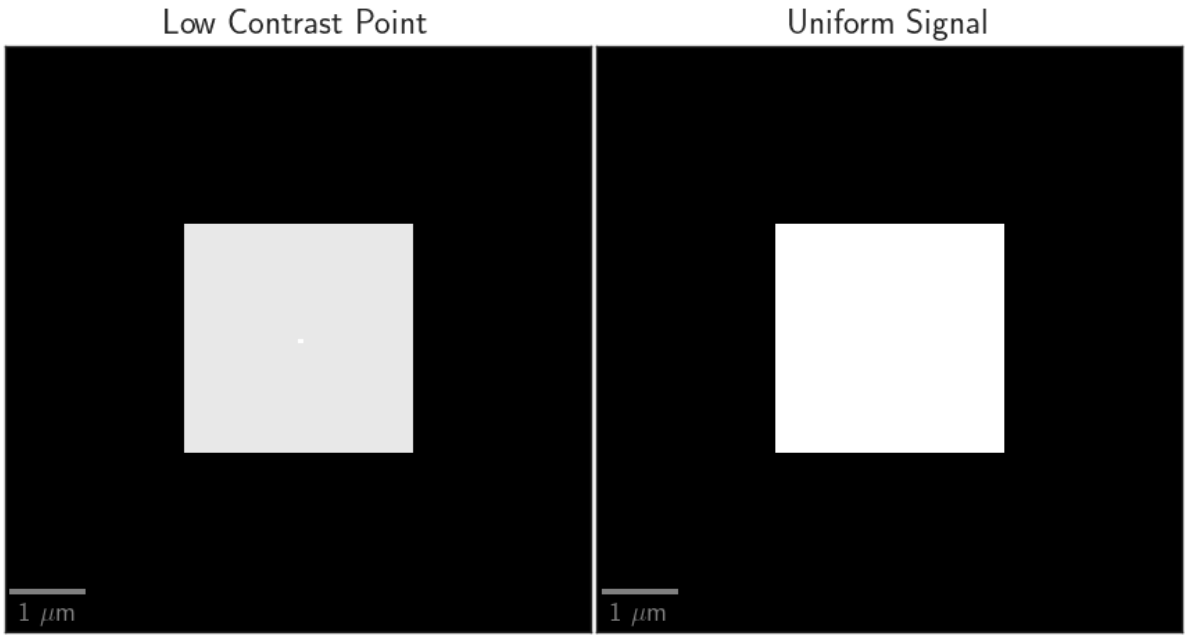

Figure 4.2: Phantoms used to measure the noise and resolution in reconstructed SIM images.

Following their method, we run noiseless simulations on a phantom with a uniform signal and on a phantom that has the same uniform signal but with a single low-contrast (less than %10 contrast) point source in the center of the signal. We also run a noisy simulation on the phantom with uniform signal so that we can measure noise. All of the simulated images are then reconstructed.

To measure resolution, we subtract the reconstructed uniform phantom from the reconstructed phantom that contains the low contrast point source. A Gaussian is fit to an intensity profile across the resulting point source in the subtraction image. From the fitted Gaussian we compute the FWHM from the standard deviation. To measure noise, we measure the standard deviation of the intensity in the uniform region for the reconstruction on the noisy simulation.

4.3.1 One-Photon SIM Simulations

For single-photon SIM, we simulate the nine acquired images using (3.2) with the following parameters:

$$k_0 = \beta\, 2\pi\, \nu_{c,ex} \tag{4.11}$$

$$\mathbf{k}^{(0)} = [k_0 \cos(\pi/4),\ k_0 \sin(\pi/4)] \tag{4.12}$$

$$\mathbf{k}^{(1)} = [k_0 \cos(2 * \pi/3 + \pi/4),\ k_0 \sin(2 * \pi/3 + \pi/4)] \tag{4.13}$$

$$\mathbf{k}^{(2)} = [k_0 \cos(-2 * \pi/3 + \pi/4),\ k_0 \sin(-2 * \pi/3 + \pi/4)] \tag{4.14}$$

$$\phi = [0,\ 2\pi/3,\ 4\pi/3], \tag{4.15}$$

where $\beta \in [0, 1]$ is a parameter that changes the frequency of the excitation intensity, k_0 and $\nu_{c,ex}$ are the respective magnitudes of the frequency vectors $\mathbf{k}$ and $\boldsymbol{\nu}$, and the subscript em or ex denotes whether the wavelength of light used was from emission or excitation photons. With $\beta = 1$, we are using the highest excitation frequency that can be passed by the excitation objective, and choosing $\beta = 0$ removes the modulation of the excitation intensity. Airy patterns are used for the objective PSFs and are computed in the spatial frequency domain using

$$O_{em}(\nu) = \frac{1}{\pi}\left(2\cos^{-1}\left(\frac{\nu}{\nu_{c,em}}\right) - \sin\left(2\cos^{-1}\left(\frac{\nu}{\nu_{c,em}}\right)\right)\right), \tag{4.16}$$

where

$$\nu_{c,em} = \frac{2\,\mathrm{NA}}{\lambda_{em}} \tag{4.17}$$

is the cutoff frequency for an objective and O_{em} is the Fourier transform of the PSF h_{em}.

In our simulations we set α to 1, along with using an NA of 0.95, an excitation wavelength of 488 nm, and an emission wavelength of 510 nm. In addition to simulating the nine structured illumination images, we use (3.3) to simulate the single-photon widefield image. For simulations with noise, we draw an image taken from a Poisson distribution with the

simulated image pixel values as the mean of the Poisson distribution.

4.3.2 Two-Photon SIM Simulations

For the two-photon simulations (4.11) becomes

$$k_0 = \beta\, 4\pi\, \nu_{c,ex}, \tag{4.18}$$

with an extra factor of two coming from squaring the excitation PSF. Plugging (4.18) into (4.12) – (4.14), we can calculate the orientation and frequency of the modulated excitation. The relative phases remain the same as those used in the one-photon SIM simulations.

In these simulations, we use an NA of 0.95, an excitation wavelength of 900 nm, and an emission wavelength of 510 nm. After simulating the nine structured illumination images, we use (3.9) to simulate a non-SIM two-photon image that we use to measure the resolution improvement when using structured illumination.

4.3.3 Simulated Bar and Points Phantoms

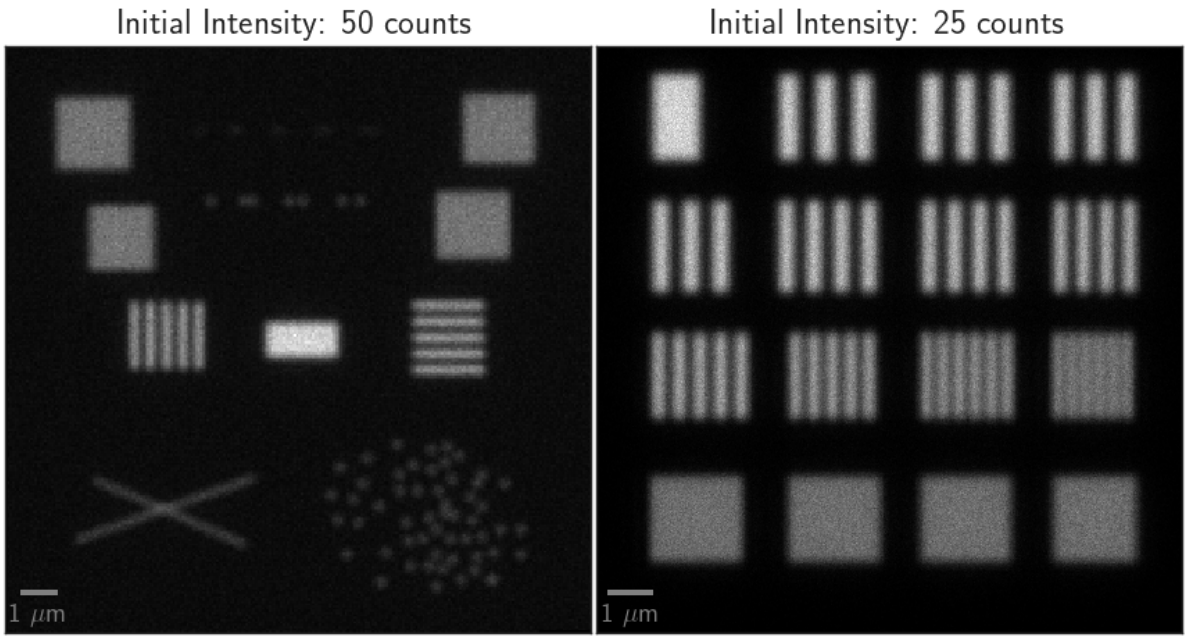

Figure 4.3: Simulated widefield data using each of the phantoms as the sample we are interested in imaging. These non-SIM images are used to assess resolution improvement gained when using SIM.

Figure 4.3 shows the simulated widefield images that we use to measure the resolution improvement gained when using structured illumination.

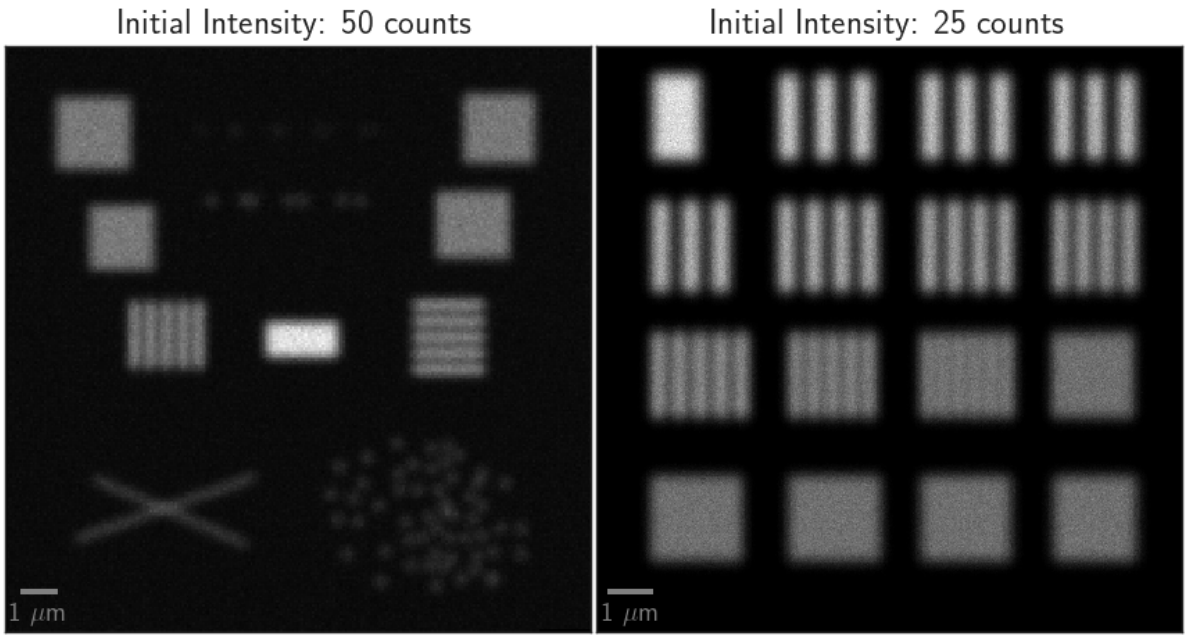

Figure 4.4: Simulated data for each phantom using the non-SIM, two-photon scanning microscope.

In Figure 4.4 we have the simulated non-SIM 2P scanning images that we use to measure resolution improvement with using 2P-SIM.

4.3.4 Simulated Uniform and Low-contrast Point Source Phantoms

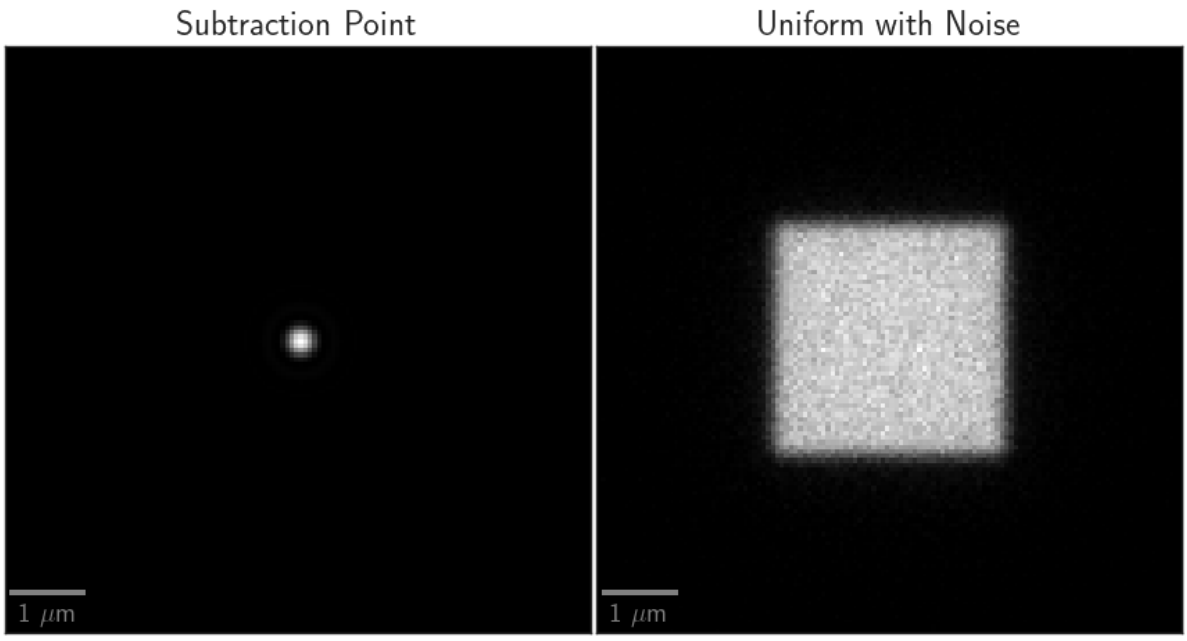

Figure 4.5: Subtraction image (left) computed from the two noise-free simulated widefield images used to measure resolution and the noisy widefield simulation (right) used to measure noise.

Figure 4.5 shows the subtraction image of two noise-free widefield images and the noisy widefield simulation for the uniform signal.

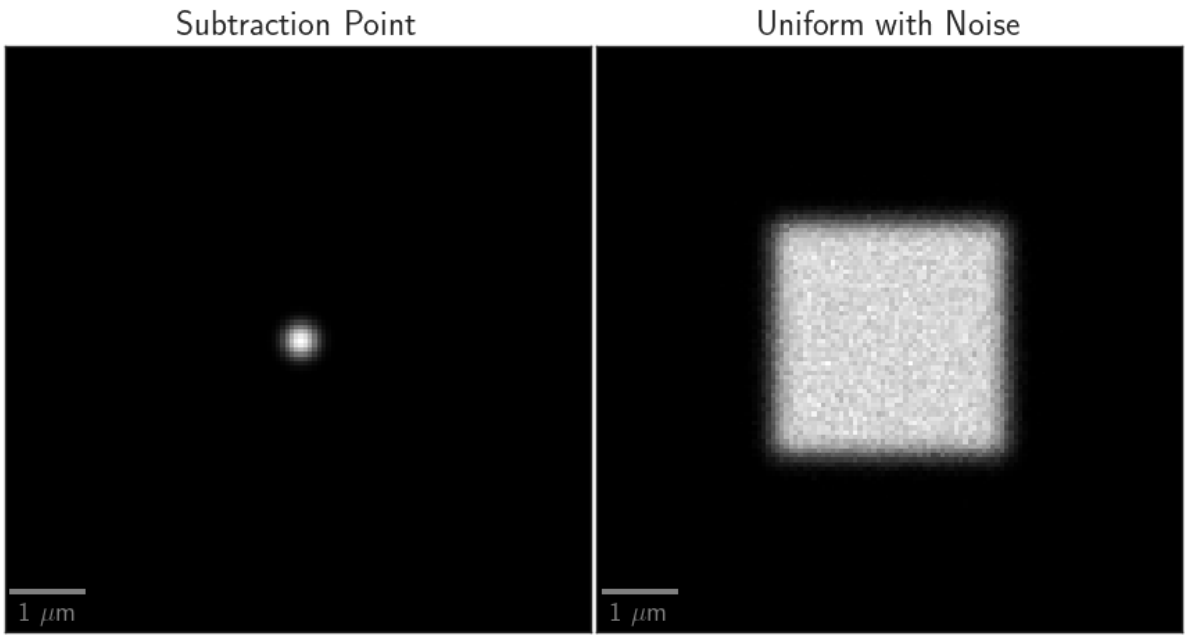

Figure 4.6: Subtraction image (left) computed from the two noise-free simulated two-photon scanning images used to measure resolution and the noisy two-photon scanning simulation (right) used to measure noise.

In Figure 4.6 we have the subtraction image of two noise-free simulated two-photon scanning microscope images and the noisy two-photon scanning simulation for the uniform signal.

4.4 Reconstructions of Simulated Data

4.4.1 Measuring Noise and Resolution

Following Section 4.3 we can measure the noise and resolution properties for the different reconstruction methods. In each reconstruction method there is a tunable parameter the we can use to vary the noise and resolution properties of the final image. In the conventional reconstruction we have η, with RL we have number of iterations, and with TV we have the constraint parameter ϵ.

By varying each parameter and measuring the FWHM and noise of the resulting re-

constructed images, we can trace out noise vs resolution curves to compare each of the reconstructions. To help negate any differences in the mean, we normalize the noise by the mean to get the relative standard deviation (RSD). Using 3.4.2, we include on the plots the theoretical resolution limits for both the SIM reconstruction and the baseline reconstruction (widefield one-photon illumination or non-SIM two-photon scanning).

One-Photon Curves

In Figure 4.7, we want to minimize both the noise and resolution so that better values are closer to the origin of the plot. As the first check we see that all of the reconstructions performed on the one-photon SIM images outperform RL deconvolution on the widefield image.

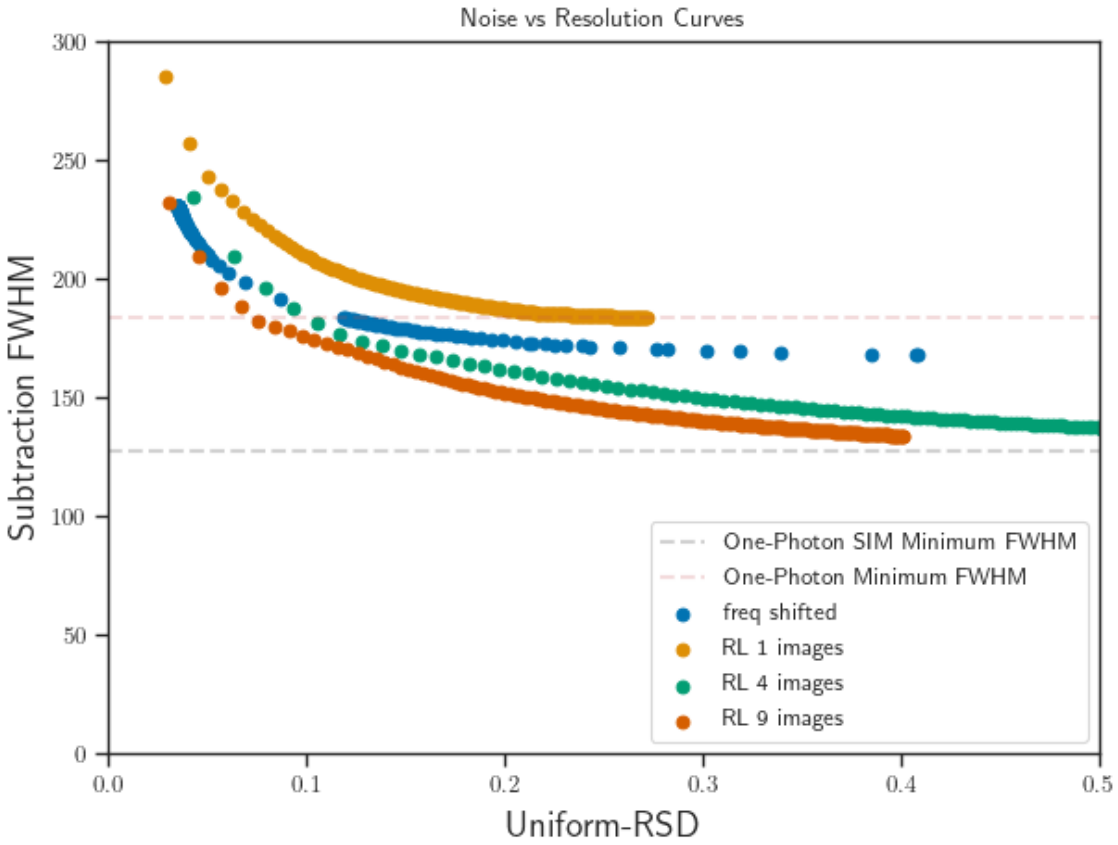

Figure 4.7: Calculated noise vs resolution plots from reconstructed one-photon SIM simulation data. The simulated data had a mean intensity of 25 counts.

Comparing the iterative reconstructions against the conventional reconstruction methods, we see that for every noise level, a better resolution is achieved when an iterative reconstruction is used. The iterative reconstructions also approach the theoretical resolution limit while the conventional reconstructions fail to saturate this limit. However, saturation of this limit comes at the cost of increased noise. One thing to note is that in the RL with four images, there is 4/9 of the exposure when compared to the freq shifted and RL nine images reconstructions. As such, the importance of noise, resolution, and exposure need to be determined for the specific imaging task.

Two-Photon Curves

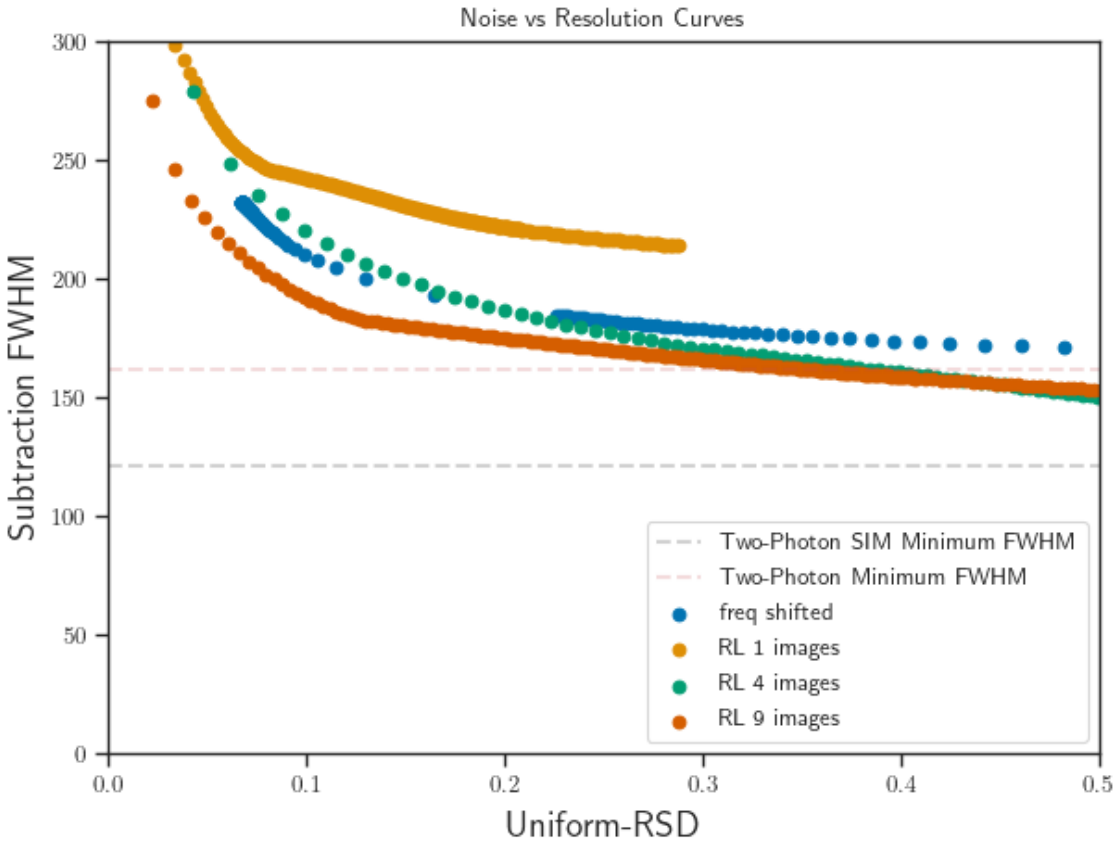

Figure 4.8: Calculated noise vs resolution plots from reconstructed two-photon SIM simulation data. The simulated data had a mean intensity of 25 counts.

As in the case of one-photon SIM, we see in Figure 4.8 that using SIM outperforms the baseline reconstruction which in this case is a two-photon scanning microscope. We also find that when using the same dataset, RL outperforms the conventional reconstruction method. Unlike the one-photon SIM reconstructions, neither the iterative nor the conventional reconstruction methods saturate the theoretical resolution limits. This is caused by the reduced contrast of higher frequency components in a scanning configuration. Another difference is that RL with only four images is no longer better than the conventional method. In this case, one would need to weigh the need for better resolution/noise or lower exposure during the acquisition process.

4.4.2 Reconstructed Bar and Points Phantoms

A potential issue with just using noise and resolution curves as the metric for image quality is that there are no indicators of error in the reconstruction. To check if any artifacts are introduced during the reconstruction process, reconstructions are done on simulated data that use the qualitative phantoms described in Section 4.3.3.

One-Photon Reconstructions

As we did with the noise and resolution curves, we run the RL deconvolution algorithm on the widefield simulations. This allows us to make sure that the resolution with 1P-SIM using the conventional reconstruction algorithm is better than we could achieve by running iterative reconstructions on non-SIM widefield simulation data.

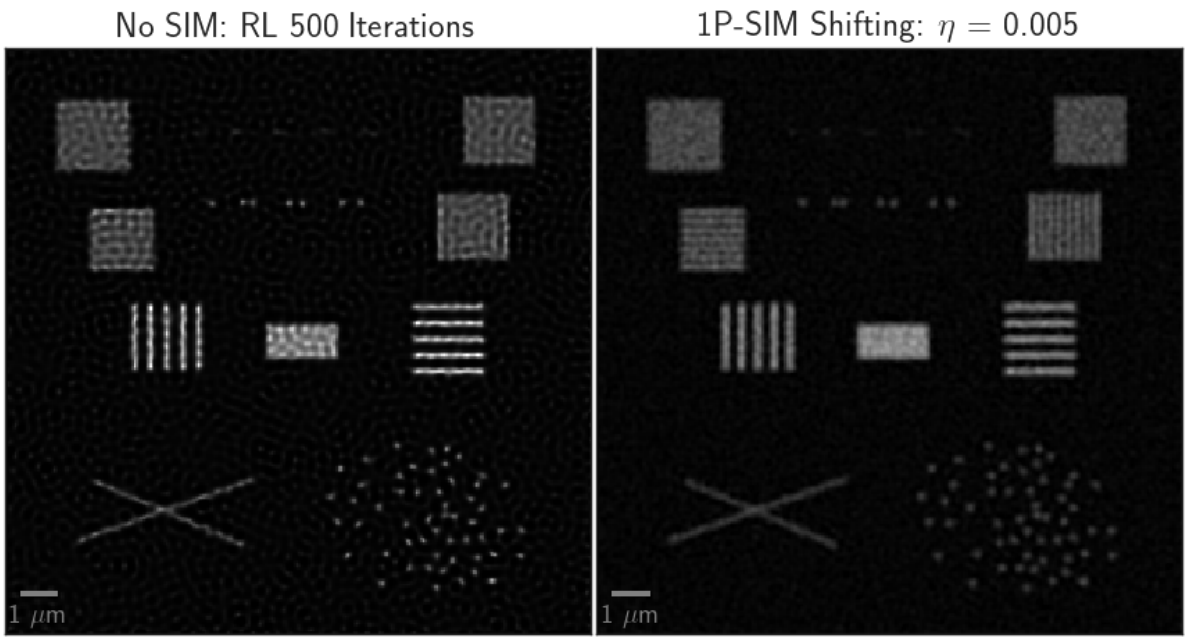

Figure 4.9: Reconstructed image for the widefield simulation (left) and the reconstructed image for 1P-SIM when using a smoothing parameter of $\eta = 5\text{x}10^{-3}$. In the reconstructed SIM image, the bars are resolvable on the middle pattern while this is not the case for the for the non-SIM reconstruction.

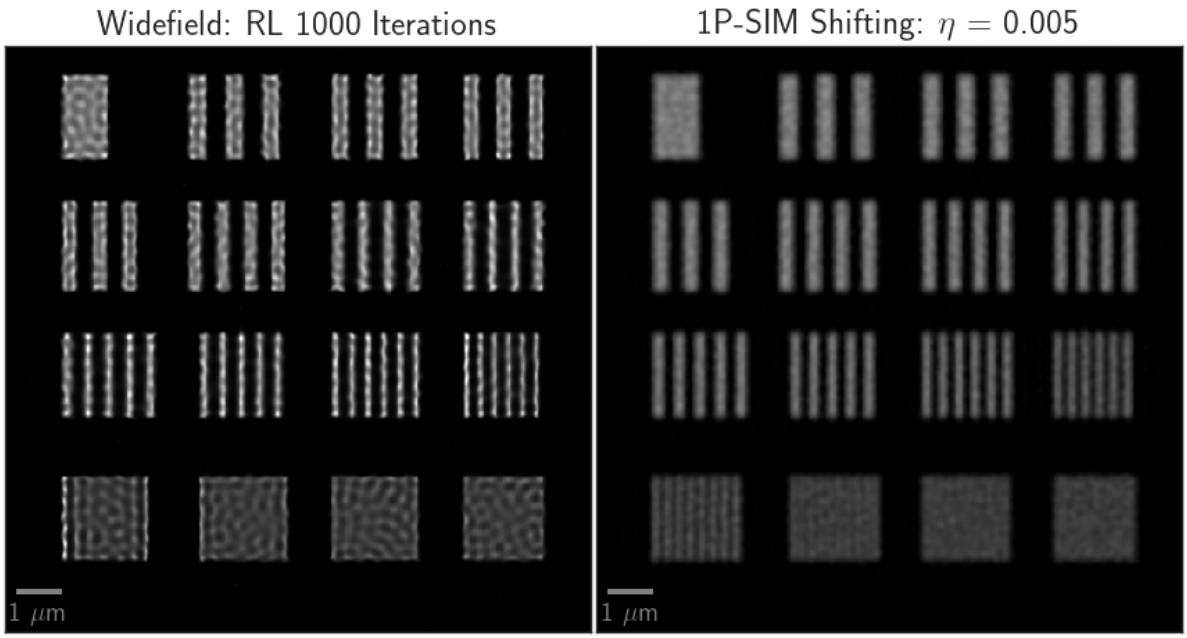

Figure 4.10: Reconstructed image for the widefield simulation (left) and the reconstructed image for 1P-SIM when using a smoothing parameter of $\eta = 5\text{x}10^{-3}$. In the reconstructed SIM image, the bottom left pattern is fully resolvable and is not resolvable in non-SIM reconstruction, indicating that the use of structured illumination does increase resolution.

Figures 4.9–4.10 show that resolution is improved by using 1P-SIM as we expect it to. In Figure 4.11 we show the reconstructed 1P-SIM images for the conventional reconstruction method and images using our implementation of RL deconvolution when using both nine acquired images and when using only four acquired images. With iterative reconstruction methods, we see that there is greater contrast in the bar patterns compared to the bar patterns in the reconstructed image that use the conventional reconstruction method.

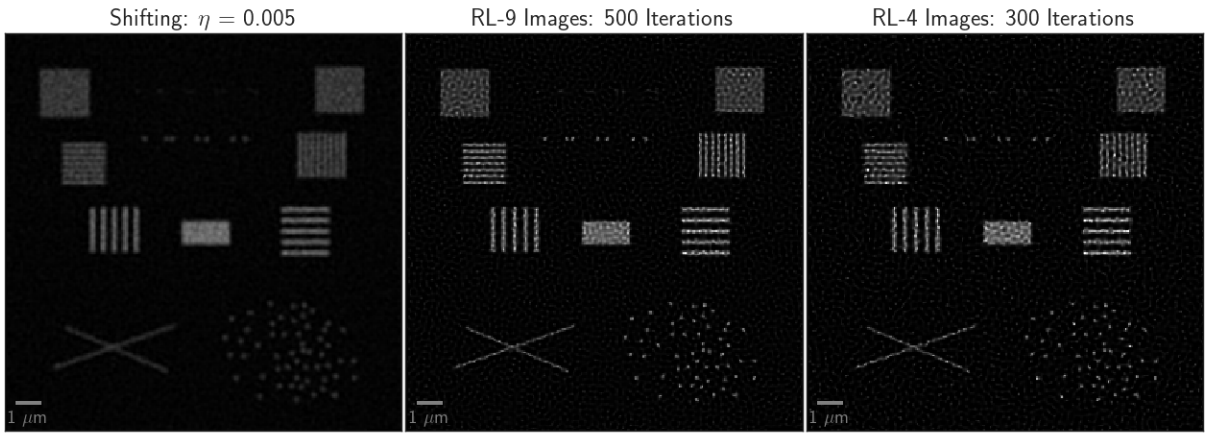

Figure 4.11: Reconstructions of the 1P-SIM simulation data when using the conventional reconstruction (left), RL deconvolution (center), and RL deconvolution with only four acquisition images.

Figure 4.12 shows the reconstructed images when the same methods are applied to simulated data using the bar phantom. Again, we are able to see that contrast is improved through the use of iterative reconstruction methods.

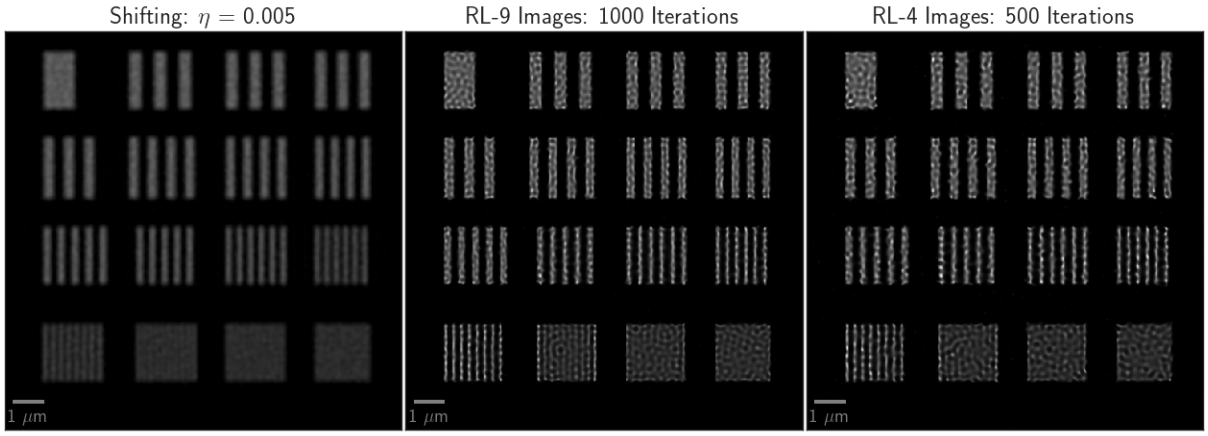

Figure 4.12: Reconstructions of the 1P-SIM simulation data when using the conventional reconstruction (left), RL deconvolution (center), and RL deconvolution with only four acquisition images.

To better show the contrast improvements achieved using an iterative reconstruction method, we plot the intensity profiles across the bottom-left pattern in the bar phantom for each of the reconstructions in Figure4.13.

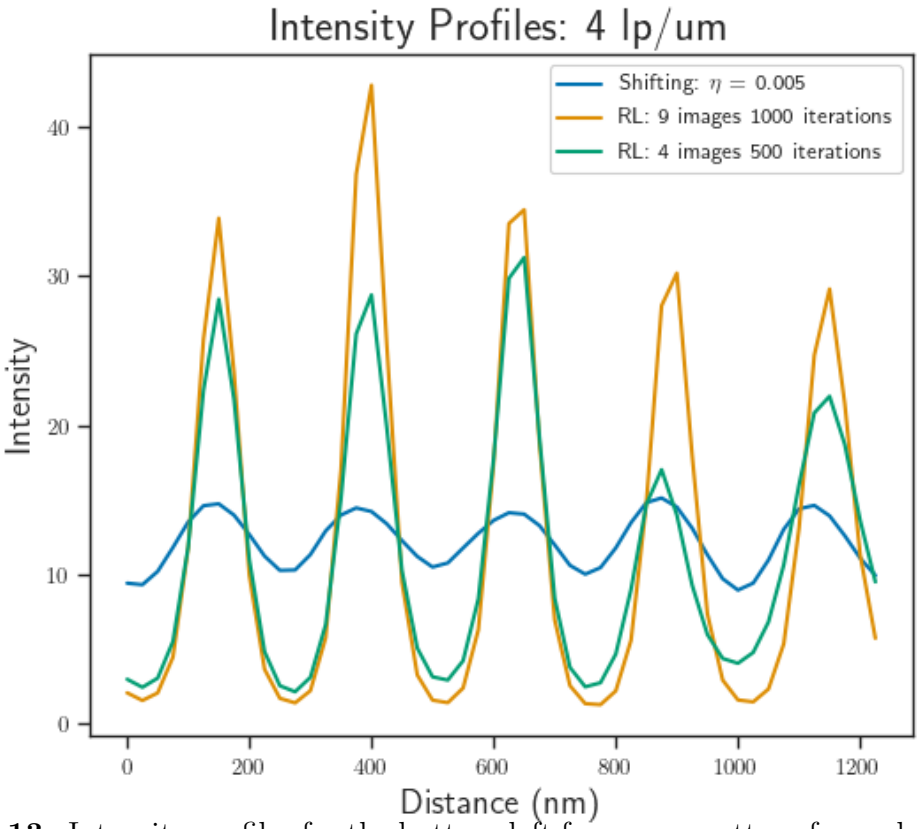

Figure 4.13: Intensity profiles for the bottom-left frequency pattern for each reconstruction method applied to the 1P-SIM simulation data.

Two-Photon Reconstructions

The same reconstruction process in Section 4.4.2 was also applied to the simulated two-photon SIM data.

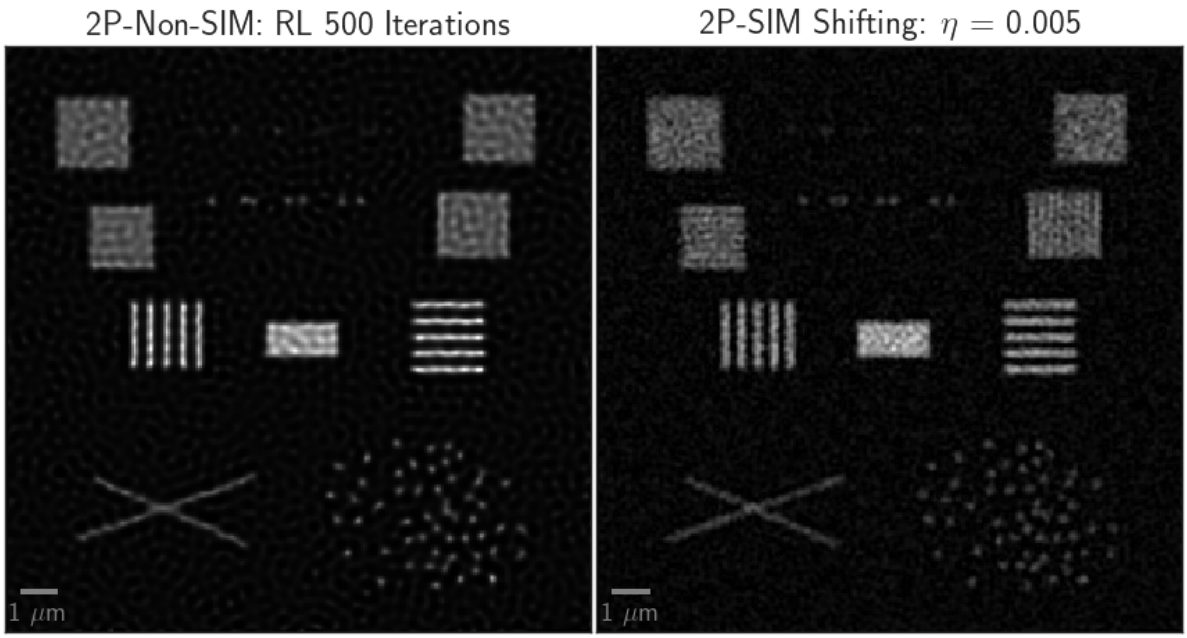

Figure 4.14: Reconstructed image for the non-SIM 2P scanning simulation (left) and the reconstructed image for 2P-SIM when using a smoothing parameter of $\eta = 5\text{x}10^{-3}$.

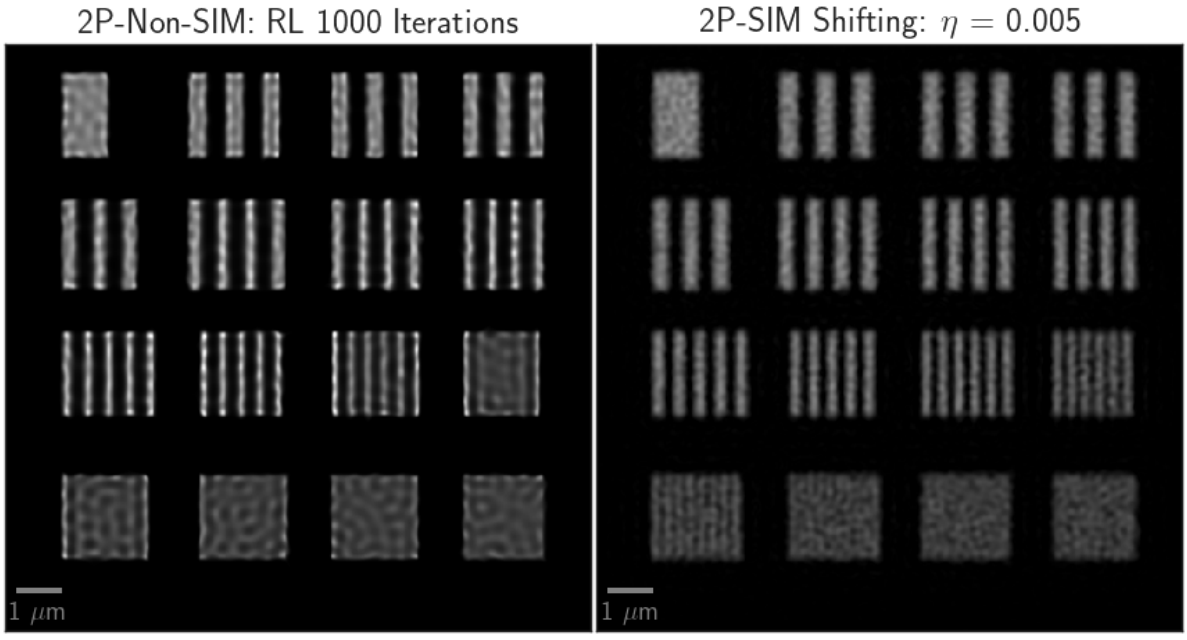

Figure 4.15: Reconstructed image for the non-SIM 2P scanning simulation (left) and the reconstructed image for 2P-SIM when using a smoothing parameter of $\eta = 5\text{x}10^{-3}$.

Similar to the one-photon simulations, Figures 4.14 and 4.15 show that resolution in

reconstructed 2P-SIM images is improved when compared to reconstructed non-SIM two-photon images.

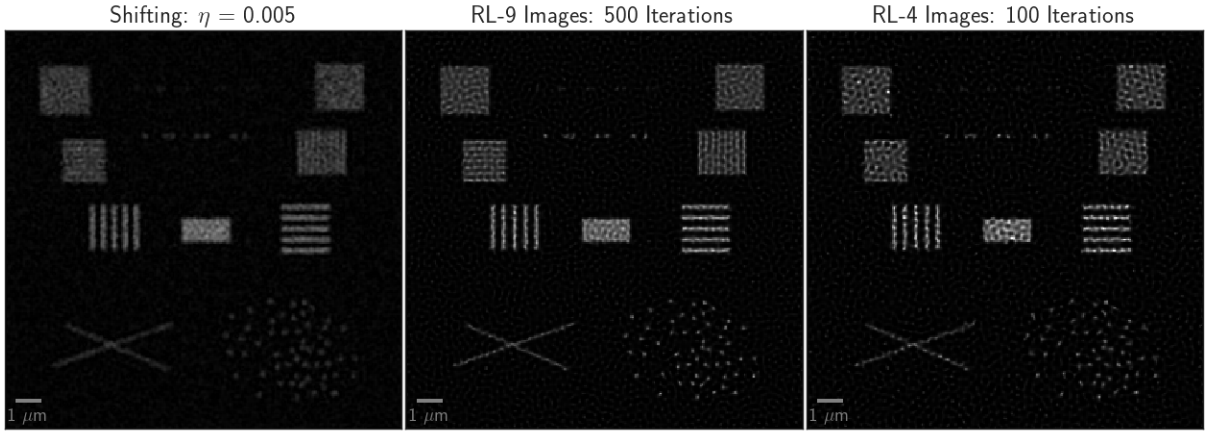

Figure 4.16: Reconstructions of the 2P-SIM simulation data when using the conventional reconstruction (left), RL deconvolution (center), and RL deconvolution with only four acquisition images.

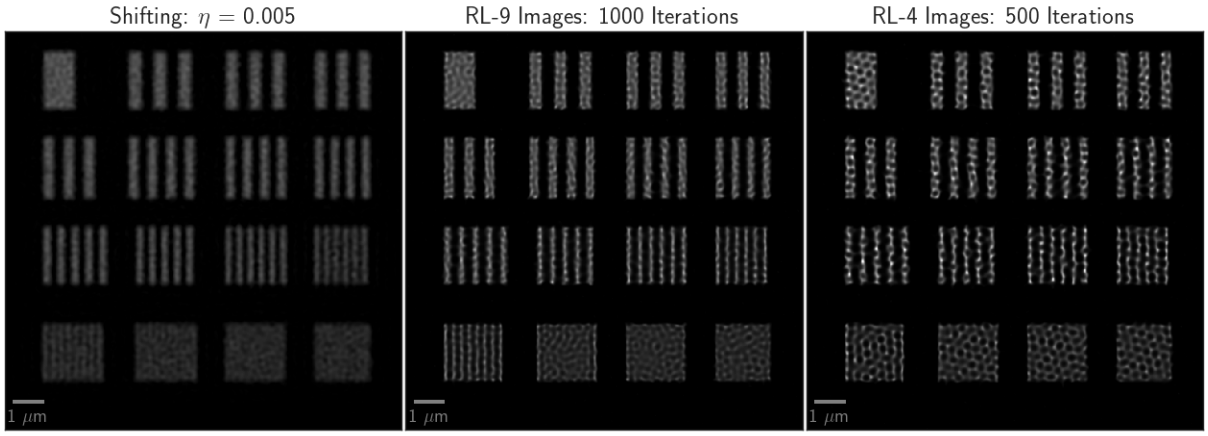

Figure 4.17: Reconstructions of the 2P-SIM simulation data when using the conventional reconstruction (left), RL deconvolution (center), and RL deconvolution with only four acquisition images. For these acquisition parameters, artifacts are introduced if only four images are used in the reconstruction.

Figure 4.16 and 4.17 again show that using RL deconvolution produces sharper reconstructions and improved contrast when compared to the conventional reconstruction method. Using only four images in the reconstruction introduces artifacts that were not present in similar reconstructions on the simulated 1P-SIM data. The artifacts are most pronounced

in larger objects in the image and appear as a honeycomb-like structure. However, while less pronounced, these artifacts are also present in small structures and have the potential to show false objects in the reconstructed image. For more automated pipelines, these artifacts could lead to incorrect results and conclusions.

This is a good example of why looking at the actual reconstructions is so important. If we had just looked at an intensity plot similar to Figure 4.13, we would not know that RL deconvolution using only four images introduces artifacts.

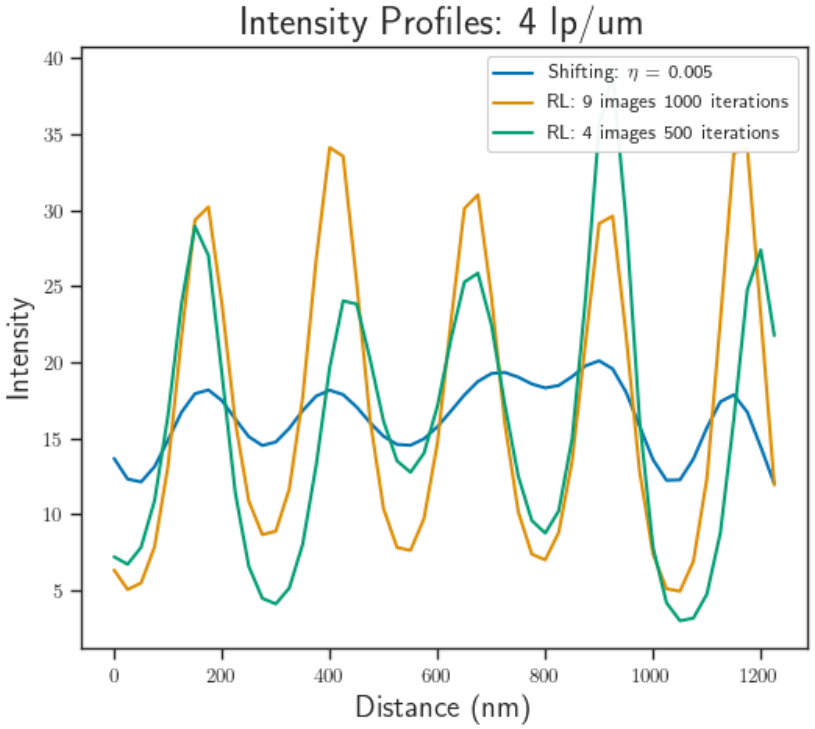

Figure 4.18: Intensity profiles for the lower left frequency pattern for each reconstruction of the 2P-SIM simulated phantom. This is a good example of when metrics used to compare reconstructions can be misleading.

4.4.3 TV Reconstruction

So far, the only iterative reconstruction method compared to the conventional reconstruction method has been RL deconvolution. This section presents the results of reconstructions that use the constrained TV method presented in Section 4.2.2.

One-Photon Reconstructions

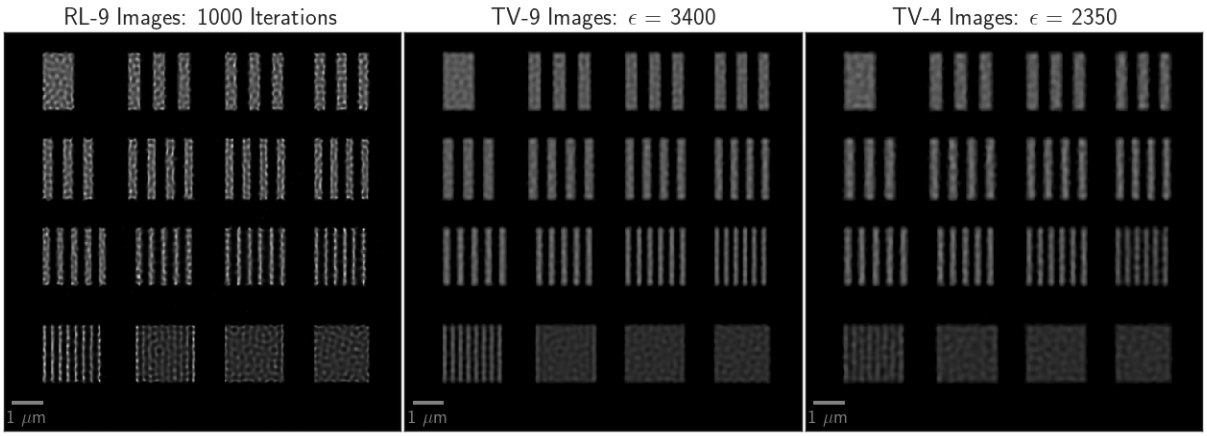

Figure 4.19: Reconstructions of the 1P-SIM simulation data when using RL deconvolution (left), TV reconstruction (center), and TV reconstruction with only four acquisition images.

Comparing the two iterative methods, we see the the bars are slightly wider when using TV. We also see that the intensity is more uniform when using regularization. Both of these traits are to be expected and is the reason to use regularized reconstruction algorithm. The wider bars with regularization can more easily be seen when plotting the intensity of the reconstructions along a line profile as shown in Figure 4.20.

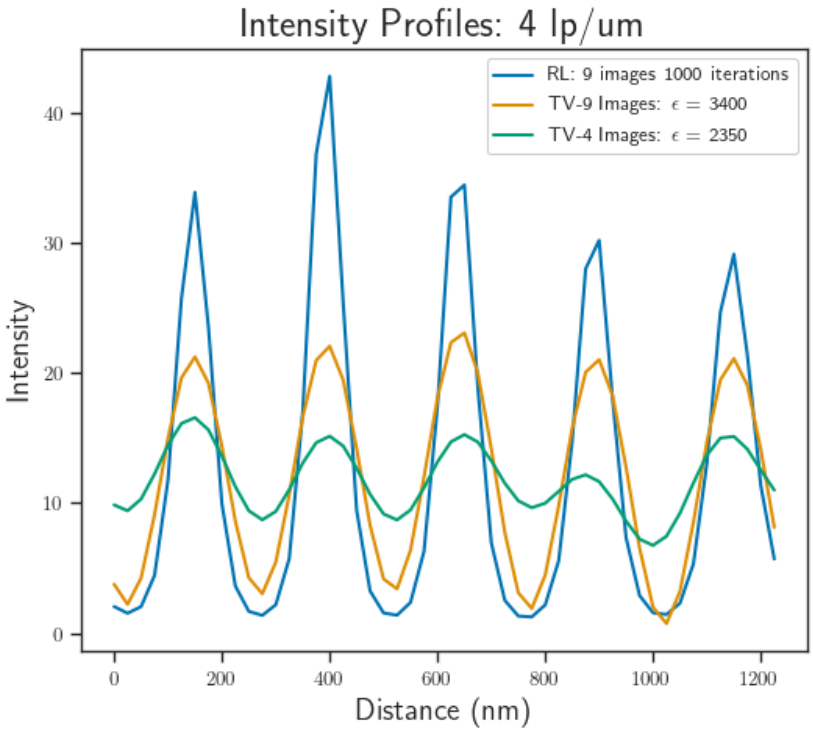

Figure 4.20: Intensity profiles for the lower left frequency pattern for each reconstruction of the 1P-SIM simulated phantom. This is a good example of when metrics used to compare reconstructions can be misleading.

Two-Photon Reconstructions

Applying the same reconstruction methods to simulated 2P-SIM data, we see that both RL and TV reconstructions produce reconstructions of similar resolutions. In Figure 4.21 we see that the TV reconstruction is able to resolve the lower left bar pattern as we saw with the RL reconstructions.

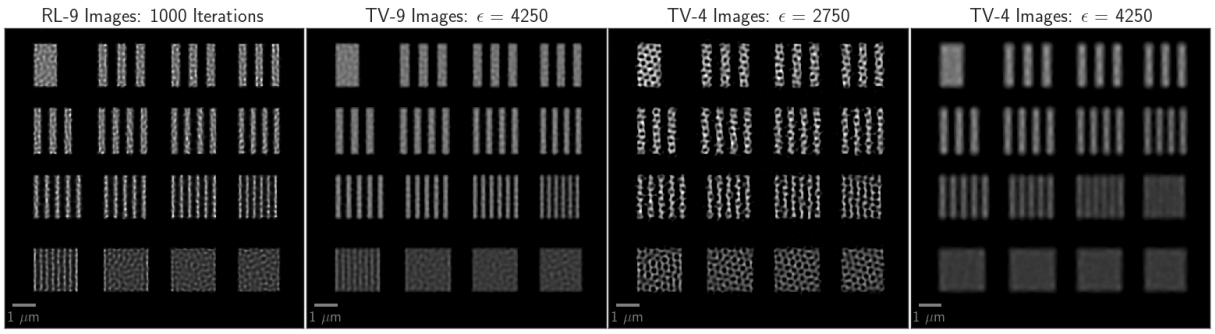

Figure 4.21: Reconstructions of the 2P-SIM simulation data when using RL deconvolution (left), TV reconstruction (center), and TV reconstruction with only four acquisition images.

However, for these reconstructions we find that there are artifacts introduced in the image when only 4 images are used in the reconstruction. These artifacts appear as a "honeycomb" pattern. In cases like this, using TV reconstructions allow us to remove some of these artifacts by using a larger constraint parameter. This promotes smoothness in the image. But there is no such thing as free lunch. The trade off for reducing the artifacts is a reduction in resolution.

4.5 Real Data

To test the robustness of the different reconstruction methods and how they perform on real data, we use data acquired by our collaborators on a scanning two-photon structured illumination microscope [37].

4.5.1 Parameter Estimation

For reconstructions done on real data, the parameters for the excitation pattern must be directly measured from the acquired data as we are no longer working with perfect systems. The first step deals with determining the frequency and phase of the excitation intensity, and begins by taking the Fourier transform of each of the acquired images. In the frequency domain, the magnitude and orientation of the frequency is measured by finding the zero

frequency peaks that are located at $-\mathbf{k}$ and $\mathbf{k}$. Using the measured $\hat{\mathbf{k}}$, the phase for each acquisition is found by solving the following equation for each of the J acquisitions.

$$\hat{\phi}_j = \arg\min_{\phi} \left|\left| \left(1 + \cos(\boldsymbol{k}_j \cdot \boldsymbol{r} + \phi)\right) - g_j(\boldsymbol{r}) \right|\right|_2^2 \tag{4.19}$$

For real data, we also need to account for a background term that is added by the camera, as well as any possible autofluorescence that the sample may generate. Each of the reconstruction methods have a unique way to account for a background term.

In both the conventional and TV reconstructions, we subtract the background from each image prior to reconstruction. To account for the noise, we subtract the minimum intensity value from each image to ensure that there are no negative values. For RL deconvolution, we simply add in a background term to the forward model. This changes the update equation in (4.7) to

$$f^{t+1}(\mathbf{r}) = \frac{f^t(\mathbf{r})}{S(\mathbf{r})} \left[\sum_{j=1}^{J} E^{(j)}(\mathbf{r}) \left(h_{em}^{\dagger\,(j)}(\mathbf{r}) * \left(\frac{g^{(j)}(\mathbf{r})}{h_{em}^{(j)}(\mathbf{r}) * E^{(j)}(\mathbf{r}) f^t(\mathbf{r}) + b} \right) \right) \right]. \tag{4.20}$$

4.5.2 Bead Data

The first data set we tested the reconstructions on are images of 87 nm glass beads fixed on a slide. Acquisition was done using a 1.4 NA oil immersion objective and an excitation wavelength of 850 nm. The emission wavelength for the fluorescent dye is centered around 500 nm. Figure 4.22 is the average of all nine images that were acquired with modulated excitation. This is a pseudo-image of what an image acquired without the modulation would look like and is the baseline comparisons for computing the resolution improvement for SIM.

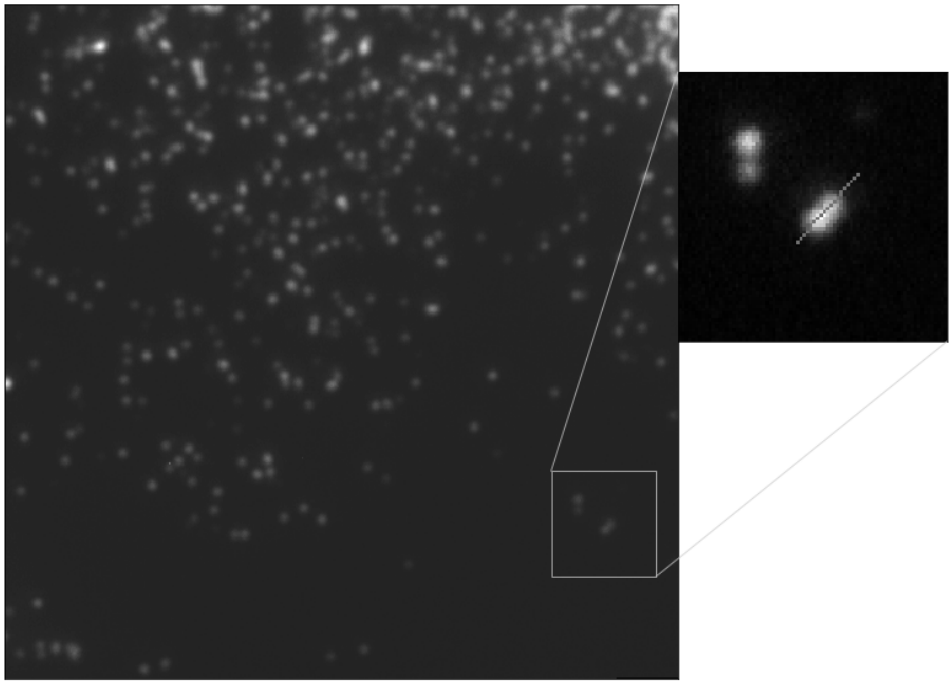

Figure 4.22: Artificial widefield image of the 87 nm beads created by averaging the nine acquired 2P-SIM images. This is the image used as the baseline image for calculating improvement with SIM.

The top right image in Figure 4.23 is the extracted ROI shown in Figure 4.22. This images is what we compare all of the reconstruction methods with. With the traditional reconstruction method (top-left), we see that the resolution has definitely improved but the background has a patchy texture that the averaged image doesn't have. In the two images that use TV reconstruction (middle row), we also see improvement in resolution, but there is also a background texture not present in the averaged image. In this case, the background seems to be the sum of waves that emanate from the beads. In the bottom row, images that used RL seem to have even more improved resolution as the two adjacent beads are easier to discern from one another. And while there is still a textured background, it is greatly reduced compared to the other methods.

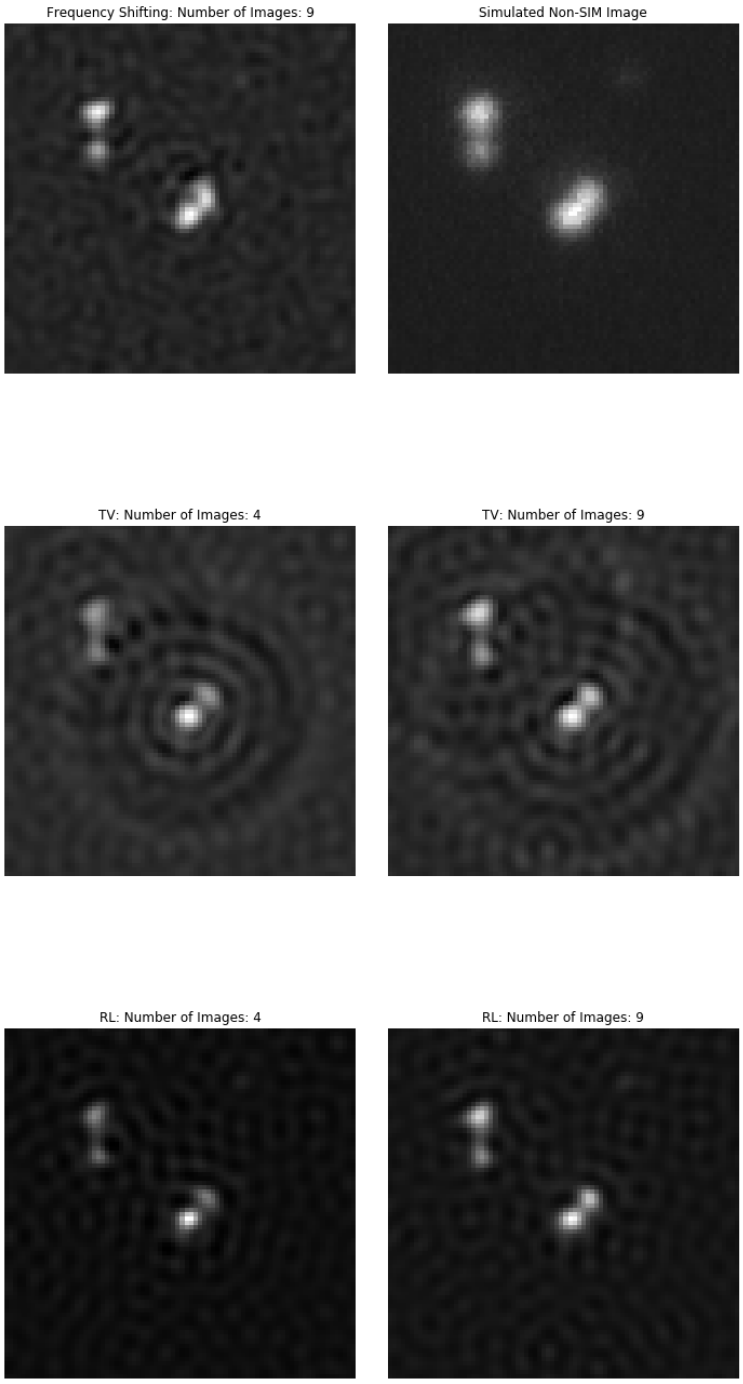

Figure 4.23: Results of the different reconstruction methods applied to real acquired data. The top row includes the traditional reconstruction (left) and the baseline non-SIM image (right). The middle and bottom rows show the results of the two iterative reconstruction methods we implemented. The left column shows reconstructions when only four images are used in the reconstruction which is not possible with the traditional method. The right column includes the reconstructions when all nine of the acquired images are used in the reconstruction.

For each of the ROIs in Figure 4.23, we plotted the intensity of the image across a line through the peaks of adjacent beads and is shown in Figure 4.24. The location of the line is shown on the insert in Figure 4.22. From the line profiles we can see that all of the reconstruction methods are able to resolve the two beads. However, we find that there is a greater contrast between the peaks and valley for the iterative reconstruction methods.

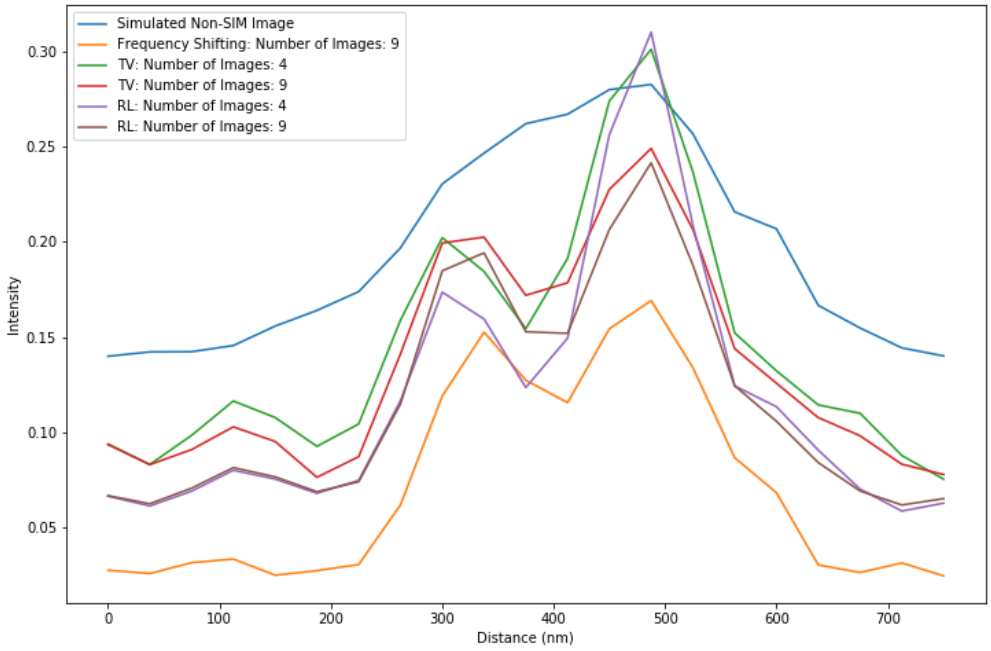

Figure 4.24: Intensity profiles for each reconstruction method along a line profile through adjacent beads. These plots allow us to determine if the peaks are resolvable for any of the reconstruction methods.

4.6 Conclusions

When using simulated data, we found that an iterative reconstruction was better able to reach and saturate the theoretical resolution bounds that we described in the previous chapter. While this is true for both one and two-photon simulations, convergence to the limit happens at a much faster rate in the one-photon reconstructions. One reason for this difference can

be attributed to the fact that the two-photon reduces the contrast of the higher frequency components that need to be recovered to achieve the best resolution.

In simulations with bar patterns, we found that even though both the linear and iterative reconstruction were able to resolve the same bars, the sharpness and contrast were greatly improved when using an iterative reconstructions. However, when using an unconstrained algorithm like RL, we found that the reconstructed bars were narrower than the bars in the underlying real data. Using a regularized reconstruction algorithm produced bars that better approximated the width of the underlying data.

For the one real data we have, we found that there was some improvement in resolution using the iterative algorithms, the biggest difference between the reconstructed data was in the background. Because RL allows for seamless integration of both a constant and spatially varying background as seen in (1.11), it performs best for data that has a non-zero background. The other two algorithms don't have such a seamless background integration. Because of this, it is important to know what the background noise looks like in the reconstructed images so that its texture is not mistaken for signals from the samples.

CHAPTER 5

CONCLUSIONS

As the speed of new microscope development continues to expand exponentially, there is an ever-growing number of systems that rely on multiple acquisitions of the sample to enhance image quality. In such systems, it is crucial to consider the trade-offs with noise, resolution, and exposure when acquiring more images.

Throughout this work, we have investigated ways to improve image quality while holding exposure constant or even reducing it. These methods take advantage of information that is already present either in the data or modify the system to acquire data that is previously uncollected. All of our work has shown how vital accurate modeling of the systems are for increasing utility and extracting more information from the data we collect.

In the case of light-sheet microscopes, we worked to improve the model for diSPIM. Improving model accuracy works to extract more information from data previously collected. Our work focused on including the effects of using a Gaussian beam to create the light-sheet into the imaging model. In previous works, the physics of Gaussian beams is often ignored, and a simpler model substituted. In simulations, we found that including beam widening of the excitation light-sheet in the imaging model results in reconstructed data that has a more isotropic resolution. Transitioning to real data did not show as noticeable of an improvement.

We also worked on ways to improve the collection efficiency during imaging to take advantage of information already being extracted from the sample. To improve collection efficiency, we added additional detection objectives (three-view diSPIM) or redirected emission photons back to the detection objectives (reflective diSPIM). In each case, we found that accurate modeling was necessary to take advantage of the additional information.

With the three-view diSPIM, we found that the addition of a third objective required the use of a rolling shutter on the camera. Since the light-sheets are no longer entirely contained in the focal plane of this objective, a rolling shutter needs to be synced with the motion of the objective to reject light not coming from the focal plane during imaging. Without an

accurate model for this shutter, the increase in image quality of the reconstructed images would not have been as significant.

We found that replacing the glass coverslip with a reflective coverslip in the diSPIM system improved imaging speed, collection efficiency, and image quality. Because the reflective coverslip creates reflected images in the acquired data, it is necessary to have an accurate model to account for the now four views collected. Without this new model, entirely removing the contamination from the coverslip was not possible during reconstruction.

Transitioning to SIM, we found that having an accurate forward model allowed us to compute what the theoretical resolutions limits are for both one- and two-photon SIM. Having known limitations makes it possible to choose imaging configurations and parameters to acquire data that has sufficient image quality for different use cases. Forgoing maximum system resolution improves image contrast.

After discretizing the forward model, we implemented two iterative reconstruction methods to test the upper bounds on the reconstructed resolution. In simulations, we found that reconstructions using RL deconvolution were able to converge quickly to the upper bound, and at the same time did not cross it. By converging but not crossing our theoretical bound, the simulations help to validate our calculations.

BIBLIOGRAPHY

[1] E. Abbe. "Beiträge zur Theorie des Mikroskops und der mikroskopischen Wahrnehmung". In: *Archiv für Mikroskopische Anatomie* 9.1 (1873), pp. 413–418.

[2] H. H. Barrett, D. W. Wilson, and B. M.W. Tsui. "Noise properties of the EM algorithm. I. Theory". In: *Physics in Medicine and Biology* 39.5 (1994), pp. 833–846.

[3] Eric Betzig et al. "Imaging intracellular fluorescent proteins at nanometer resolution". In: *Science* 313.5793 (2006), pp. 1642–1645.

[4] M Chalfie et al. "Green fluorescent protein as a marker for gene expression". In: *Science* 263.February (1994), pp. 802–805.

[5] Antonin Chambolle and Thomas Pock. "A first-order primal-dual algorithm for convex problems with applications to imaging". In: *Journal of Mathematical Imaging and Vision* 40.1 (2011), pp. 120–145.

[6] Raghav K Chhetri et al. "Whole-animal functional and developmental imaging with isotropic spatial resolution". In: *Nature Methods* 12.12 (2015), pp. 1171–1178. ISSN: 1548-7105. DOI: 10.1038/nmeth.3632. URL: https://doi.org/10.1038/nmeth.3632.

[7] I. Csiszar. "I-Divergence Geometry of Probability Distributions and Minimization Problems". In: *Ann. Probab.* 3.1 (Feb. 1975), pp. 146–158. DOI: 10.1214/aop/1176996454. URL: https://doi.org/10.1214/aop/1176996454.

[8] W Denk, J. Strickler, and W. Webb. "Two-photon laser scanning fluorescence microscopy". In: *Science* 248.4951 (1990), pp. 73–76.

[9] Nicolas Dey et al. "Richardson–Lucy algorithm with total variation regularization for 3D confocal microscope deconvolution". In: *Microscopy Research and Technique* 69.4 (2006), pp. 260–266. DOI: 10.1002/jemt.20294. eprint: https://onlinelibrary.wiley.com/doi/pdf/10.1002/jemt.20294. URL: https://onlinelibrary.wiley.com/doi/abs/10.1002/jemt.20294.

[10] Måns Ehrenberg. "The Nobel Prize in Chemistry 2008 - Advanced Information". In: *Nobelprize.org. Nobel Media AB* (2008).

[11] Måns Ehrenberg. *The Nobel Prize in Chemistry 2014 - Advanced Information*. 2014.

[12] Jeffrey A. Fessler. "Mean and variance of implicitly defined biased estimators (Such as penalized maximum likelihood): Applications to tomography". In: *IEEE Transactions on Image Processing* 5.3 (1996), pp. 493–506.

[13] Jeffrey A. Fessler and W. Leslie Rogers. "Spatial resolution properties of penalized-likelihood image reconstruction: Space-invariant tomographs". In: *IEEE Transactions on Image Processing* 5.9 (1996), pp. 1346–1358.

[14] Stuart Geman and Donald Geman. "Stochastic Relaxation, Gibbs Distributions, and the Bayesian Restoration of Images". In: *IEEE Transactions on Pattern Analysis and Machine Intelligence* PAMI-6.6 (1984), pp. 721–741.

[15] Kuang Gong, Simon R Cherry, and Jinyi Qi. "On the assessment of spatial resolution of PET systems with iterative image reconstruction". In: *Physics in Medicine and Biology* 61.5 (2016), N193–N202.

[16] Maria Göppert-Mayer. "Uber Elementarakte mit zwei Quantensprüngen". In: *Annalen der Physik* 401.3 (1931), pp. 273–294.

[17] M. G L Gustafsson. "Surpassing the lateral resolution limit by a factor of two using structured illumination microscopy". In: *Journal of Microscopy* 198.2 (2000), pp. 82–87.

[18] Mats GL Gustafsson, DA Agard, JW Sedat, et al. "I5M: 3D widefield light microscopy with better than 100nm axial resolution". In: *Journal of microscopy* 195.1 (1999), pp. 10–16.

[19] O Heimstädt. "The fluorescence microscope (Das Fluoreszenzmikroskop)". In: *Z Wiss Mikrosk* 28 (1911), pp. 330–337.

[20] Rainer Heintzmann and Christoph G Cremer. "Laterally modulated excitation microscopy: improvement of resolution by using a diffraction grating". In: *Optical Biopsies and Microscopic Techniques III*. Vol. 3568. International Society for Optics and Photonics. 1999, pp. 185–196.

[21] Stefan W Hell and Jan Wichmann. "Breaking the diffraction resolution limit by stimulated emission: stimulated-emission-depletion fluorescence microscopy". In: *Optics Letters* 19.11 (1994), p. 780.

[22] Jan Huisken et al. "Optical sectioning deep inside live embryos by selective plane illumination microscopy". In: *Science* 305.5686 (2004), pp. 1007–1009.

[23] Robert E Kass and Larry Wasserman. "The Selection of Prior Distributions by Formal Rules". In: *Journal of the American Statistical Association* 91.435 (1996), pp. 1343–1370.

[24] August Köhler. "Ein neues Beleuchtungsverfahren für mikrophotographische Zwecke". In: *Zeitschrift für wissenschaftliche Mikroskopie und für Mikroskopische Technik* 10.4 (1893), pp. 433–440.

[25] L. B. Lucy. "An iterative technique for the rectification of observed distributions". In: *The Astronomical Journal* 79.6 (1974), p. 745.

[26] Francois Orieux et al. "Bayesian estimation for optimized structured illumination microscopy". In: *IEEE Transactions on Image Processing* 21.2 (2012), pp. 601–614.

[27] Donald C. O'Shea. *Elements of Modern Optical Design*. Reading, Massachusetts: Wiley, 1985.

[28] J Qi and R M Leahy. "A theoretical study of the contrast recovery and variance of MAP reconstructions from PET data." In: *IEEE transactions on medical imaging* 18.4 (1999), pp. 293–305.

[29] W Richardson. "Bayesian-based iterative method of image restoration". In: *Journal of the Optical Society of America* 62.I (1972), pp. 55–59.

[30] Michael J Rust, Mark Bates, and Xiaowei Zhuang. "Sub-diffraction-limit imaging by stochastic optical reconstruction microscopy (STORM)". In: *Nature Methods* 3.10 (2006), pp. 793–795.

[31] Johannes Schindelin et al. "Fiji: an open-source platform for biological-image analysis". In: *Nature Methods* 9.7 (2012), pp. 676–682. ISSN: 1548-7105. DOI: 10.1038/nmeth.2019. URL: https://doi.org/10.1038/nmeth.2019.

[32] Shepp, L. A. and Vardi, Y. "Maximum Likelihood Reconstruction for Emission Tomography". In: *IEEE Transactions on Medical Imaging* 1.2 (1982), pp. 113–122.

[33] Emil Y. Sidky, Jakob H. Jorgensen, and Xiaochuan Pan. "Convex optimization problem prototyping for image reconstruction in computed tomography with the ChambollePock algorithm". In: *Physics in Medicine and Biology* 57.10 (2012), pp. 3065–3091.

[34] H. Siedentopf and R. Zsigmondy. "Uber Sichtbarmachung und Größenbestimmung ultramikoskopischer Teilchen, mit besonderer Anwendung auf Goldrubingläser". In: *Annalen der Physik* 315.1 (1902), pp. 1–39.

[35] A.N. Tikhonov. "On the stability of inverse problems". In: *Doklady Akademii nauk SSSR* 39.5 (1943), pp. 195–198.

[36] A.N. Tikhonov and V.Y. Arsenin. *Solutions of ill-posed problems*. Washington, D.C.: W.H. Winston, 1977.

[37] Ben E. Urban et al. "Super-resolution two-photon microscopy via scanning patterned illumination". In: *Physical Review E - Statistical, Nonlinear, and Soft Matter Physics* 91.4 (2015), pp. 1–6.

[38] Yicong Wu and Hari Shroff. "Faster, sharper, and deeper: structured illumination microscopy for biological imaging". In: *Nature Methods* 15.12 (2018), pp. 1011–1019. ISSN: 1548-7105. DOI: 10.1038/s41592-018-0211-z. URL: https://doi.org/10.1038/s41592-018-0211-z.

[39] Yicong Wu et al. “Reflective imaging improves spatiotemporal resolution and collection efficiency in light sheet microscopy”. In: *Nature Communications* 8.1 (2017), p. 1452.

[40] Yicong Wu et al. “Simultaneous multiview capture and fusion improves spatial resolution in wide-field and light-sheet microscopy”. In: *Optica* 3.8 (2016), p. 897.

[41] Yicong Wu et al. “Spatially isotropic four-dimensional imaging with dual-view plane illumination microscopy.” In: *Nature biotechnology* 31.11 (2013), pp. 1032–8.

APPENDIX A

SUPPLEMENTARY MATERIAL

A.1 Total Variation Minimization

Algorithm 2: Pseudocode for Chambolle-Pock L2 constrained, TV-minimization.

INPUT : data $\vec{g}$, data-error tolerance ϵ

OUTPUT: object estimate f_{N}, p_{N}, q_{N}

Set : $\nu \leftarrow ||\mathbf{H}||_2/||\nabla||_2$, L $\leftarrow ||(\mathbf{H}, \nu\nabla)||_2$, $\tau \leftarrow 1/L$, $\sigma \leftarrow 1/L$, $\theta \leftarrow 1$, $n \leftarrow 0$, $\lambda_0 \leftarrow 1$

Initialize : $f_0 = 0_{\mathbb{I}}$, $p_0 = 0_{\mathbb{D}}$, and $\vec{q_0} = 0_{\mathbb{V}}$

$\bar{f}_0 \leftarrow f_0$

while n ¡ N **do**

  $\lambda_n \leftarrow \lambda_0 2^{-\log_2 n}$

  $p'_n \leftarrow p_n + \sigma(\mathbf{H}\bar{f}_n - \vec{g})$

  $p_{n+1} \leftarrow \max\left(||p'_n||_2 - \sigma\epsilon, 0\right) \frac{p'_n}{||p'_n||_2}$

  $\vec{q'_n} \leftarrow \vec{q_n} + \sigma\nu\nabla\bar{f}_n$

  $\vec{q}_{n+1} \leftarrow \vec{q'_n}((\lambda/\nu)/\max\left(\lambda/\nu, |\vec{q'_n}|\right))$

  $f_{n+1} \leftarrow f_n - \tau\ \mathbf{H}^{\mathrm{T}} p_{n+1} + \nu\ \mathrm{div}(\vec{q'}_{n+1})$

  $\bar{f}_{n+1} \leftarrow f_{n+1} + \theta(f_{n+1} - f_n)$

  $cPD \leftarrow \frac{\lambda}{\nu}||(|\nu\ \nabla f_{n+1}|)||_1 + \epsilon||p_{n+1}||_2 + p_{n+1}^T\vec{g}$

  $L2_{\mathrm{Diff}} \leftarrow ||f_{n+1} - f_n||_2\ /\ ||f_{n+1}||_2$

  if $cPD < 10^{-6}$ || $L2_{\mathrm{Diff}} < 10^{-8}$ **then**

    return

  $n \leftarrow n + 1$

return